UNIVERSIDAD DE CHILE
FACULTAD DE CIENCIAS FISICAS Y MATEMATICAS
DEPARTAMENTO DE ASTRONOMIA

MONITOREO OPTICO DE CUASARES LUMINOSOS DE ALTO REDSHIFT

TESIS PARA OPTAR AL GRADO DE MAGISTER EN CIENCIAS
MENCION ASTRONOMIA

ISMAEL ANDRES BOTTI ROJAS

PROFESOR GUIA:
PAULINA LIRA TEILLERY

MIEMBROS DE LA COMISION:
LUIS CAMPUSANO BROWN
MARIO HAMUY WACKENHUT
NEIL MARK NAGAR

SANTIAGO DE CHILE
MARZO 2011

Resumen

Este trabajo se enmarca en una campaña de monitoreo óptico de una muestra de 56 cuasares (QSO) de alta luminosidad ($\lambda L_\lambda(1350\,\text{Å}) \gtrsim 10^{46.5}\,\text{erg}\,\text{s}^{-1}$) y de alto redshift ($z > 2$), el cual se lleva a cabo usando imágenes directas y espectros obtenidos en telescopios de pequeña y mediana envergadura desde los observatorios de Cerro Tololo y Las Campanas.

El objetivo principal de este monitoreo consiste en seleccionar los objetos con mayor variabilidad en el contínuo, caracterizado por el flujo en el filtro *R*, para los cuales se comienza un monitoreo espectroscópico con el fin de medir el tamaño de la región de líneas anchas (BLR), así como también la masa del agujero negro (BH) central de cada cuasar usando la técnica conocida como *mapeo de reverberación*.

El mapeo de reverberación es el único método para medir directamente la masa del BH central en los nucleos activos de galaxias (AGNs) y ha sido aplicado exitosamente en una treintena de AGNs de luminosidad baja e intermedia. Sin embargo, la masa de los BH en QSOs, los AGN de mayor luminosidad, aún no han sido directamente medidos. Esto es particularmente importante debido a que la mayoría de estos objetos se encuentran a alto redshift, época clave para la evolución de las galaxias. El mapeo de reverberación para estas fuentes no es tarea fácil debido a las largas escalas de tiempo involucrados, debido a que son sistemas intrínsecamente más grandes, y al factor $(1+z)$ debido a la expansión del universo, lo que hace de este un proyecto ambicioso y de largo plazo (10 años).

En este trabajo de tesis se muestra el análisis de la variabilidad del contínuo de los primeros 6 años del monitoreo, que ha permitido la identificación de una sub-muestra de cuasares de alta variabilidad, que corresponde a un 30% de la muestra completa, los cuales ya se están monitoreando espectroscópicamente y que corresponden a los candidatos para realizar estudios de reverberación en los próximos 4 años. Además se presentan resultados preliminares para tres objetos con curvas de luz suficientemente pobladas, tanto en el contínuo como en las líneas de emisión observadas, que corresponden al Si IV , C IV y C III] . Estos resultados preliminares indican que la masa de los BH en estos objetos es del orden de $10^9\,\text{M}_\odot$ y que además el tamaño de su BLR concuerda con la relacion $R_{\text{BLR}} - L_{\text{UV}}$ basado en la línea de C IV propuesta por Kaspi et al. (2007).

Agradecimientos

Debo partir agradeciendo a mi Mamá, quien con esfuerzo nos ha sacado a mi y a mis hermanos adelante. Sin su apoyo incondicional no hubiera llegado a ninguna parte y espero que este orgullosa, así como yo estoy orgulloso de ella. A mi Tata, que si estuviera aquí de seguro tendría una copia de esta tesis. A mi Ita, a mis hermanos, a mi abuela Nelly, a mi familia entera.

Quiero agradecer profundamente a Paulina Lira, mi jefa, que siempre tuvo palabras de apoyo y que fue un pilar fundamental en mi formación tanto personal como académica y profesional, sobre todo en momentos de mucha indecisión. Muchas gracias por la paciencia, por los consejos, por creer en mi y por hacerme trabajar. Toda esa pega en el hostal de Rio valió la pena :)

También les doy las gracias a mis compañeros de Calán. Pasamos muchos buenos momentos y terminé haciendo tremendas amistades. Luciano, Hugo, Simón y Coté, las mejores vibras en lo que se viene!.

A Nidia Morrell por su tremenda paciencia y por enseñarme la pasión por estar dentro de un domo mirando al cielo con dedicación. Al observatorio Las Campanas, y en especial a don Hector por esas cenas que espero volver a probar dentro de poco.

Debo agradecer también a Jaime Campos y en especial a Armando Cisternas por creer en mi, en mis capacidades y enseñarme que este planeta está vivo. A pesar de que nuestros intereses van por distintos caminos siempre encontramos temas de común interés junto a un buen café.

Agradezco a mis amigos, que son parte importantísima de mi familia: Bea, Panchito, Carlos, Coke, Flavio, Eme, Felpo y Gumi.

Finalmente agradezco a quienes se me quedan en el tintero ... que no son pocos.

Contents

List of Figures **IV**

List of Tables **IX**

1 Introduction **1**

1.1 Active Galactic Nuclei 1

1.1.1 The Broad Line Region: what we know. 3

1.1.2 Reverberation Mapping 3

1.2 Scaling Relations 6

1.3 Galaxy Evolution and Black Holes Demography 6

1.4 This Thesis 7

2 High Luminosity Quasar Monitoring Campaign **9**

2.1 Observational Strategy 10

2.2 Quasars Sample 10

2.3 Monitoring Campaign Length 13

2.4 Comparison with the Work of Kaspi et al. (2007) 13

2.5 Observations 14

3 Broad Band Imaging **18**

3.1 Data Reduction 19

3.2 Photometric Measurements 19

3.2.1 Field Stars Catalogue . . . 20
3.2.2 Photometry . . . 21
3.2.3 Diferential Light Curves (DLCs) . . . 23

4 Spectroscopy **27**

4.1 Data Reduction . . . 27
4.2 Normalized Spectra . . . 28
4.3 Emission Lines Fluxes . . . 30
4.4 Emission Lines Widths . . . 33
4.5 Calibrated spectra . . . 34

5 Variability Measurements **36**

5.1 Variability Estimators . . . 36
5.2 Variability Measurements . . . 37
5.3 Analysis . . . 38
5.3.1 Continuum Variability . . . 38
5.3.2 Emission Lines Variability . . . 39

6 Preliminary Results and Reverberation Measurements **45**

6.1 Lag estimate . . . 45
6.2 Filling the high end of the luminosity range in the $R_{\rm BLR} - L_{\rm UV}$ relation . . . 48
6.3 Preliminary Black Hole Masses . . . 48
6.4 Preliminary Accretion Rates . . . 50

7 Conclusions **53**

Bibliography **56**

Appendix **58**

A Continuum and BLR Emission Lines Light Curves **59**

A.1 Light Curves: Spectrophotometrically Monitored Objects 59

A.2 Continuum Light Curves: Photometrically Monitored Objects 64

A.3 Continuum Light Curves: Photometrically Discarded Objects 69

B Optical Spectra **72**

List of Figures

1.1 Unified model of the central engine of an AGN (From Carroll & Ostlie). 2

1.2 Rest frame velocity v_{FWHM} versus rest frame centroid time lag τ for five BLR emission lines in NGC 3783. The dashed line is the best fit to the data; the solid line is the best fit with fixed slope of -0.5, consistent with a virialized BLR. From Onken & Peterson 2002. 5

1.3 $R_{BLR} - L$ relation based on Hβ line and $\lambda L_\lambda(5100\,\text{Å})$ form Kaspi et al. 2005. The slope is 0.69 ± 0.05. 7

1.4 $R_{BLR} - L$ relation using the C IV line and $\lambda L_\lambda(1350\,\text{Å})$ form Kaspi et al. 2007. The slope is 0.52 ± 0.04. 7

2.1 Cartoon which shows the way to calculate the Cassegrain Ring angle for a particular QSO. North and East are labeled and the slit is represented by the inclined rectangle. QSO is at the center of the image, assumed to be the center of rotation in this example. In the left panel, the comparison star (A) is at the left, and then the slit has to be rotated clockwise. The middle panel shows the comparison star (B) at the right, so the slit should be rotated counter-clockwise. A snapshot of the acquisition image of a QSO and its comparison star is shown in the right panel. Both targets are perfectly aligned along the wide slit. 15

3.1 Galaxy Mk 579 cataloged as a Seyfert 2. With a redshift of $z = 0.017$ an extended host galaxy can be easily seen. 21

3.2 Quasar CTQ 286. With a redshift of $z = 2.8$ only a point source is seen. 21

3.3 Histogram with the instrumental magnitudes for the quasar sample (left) and for the mean magnitude of the comparison field stars of each quasar (right). 24

4.1 CTQ 953 comparison star optical spectrum. Noise and absorption lines (Balmer an telluric) can be seen. . . 29

4.2 CTQ 953 comparison star optical spectrum after boxcar filtering. The resultant spectrum is smooth and featureless. 29

4.3 Ratio between CTQ CT320 spectra obtained in two consecutive nights (December 20th and 21st, 2008). . . 30

4.4 Ratio between CTQ 953 spectra obtained in two observations four days apart (July 7th and July 11th, 2010). 30

4.5 Scheme for the continuum fitting. 32

4.6 Normalized spectrum of CTQ 953. Blue and red continuum windows for each emission line are shown above the spectrum, while the emission lines windows are shown below for Si IV $\lambda 1400 + $ O IV] $\lambda 1402$, C IV $\lambda 1549$ and Si III] $\lambda 1892 + $ C III] $\lambda 1909$respectively. 32

5.1 Histogram with the variability amplitude ($A_{\rm var}$) of the 56 quasars in the sample. Vertical lines represents the limits for discarded, photometric and spectrophotometric monitored objects. The histogram on the right shows the amplitude of the mean field stars variability, used as a comparison in the continuum monitoring. 40

5.2 Mean fractional variability $F_{\rm var}$ parameter for the continuum light curves of the whole sample. The spectrophotometric sample is shown in blue. The mean and median of the distribution are shown as vertical lines. 40

5.3 Mean fractional variability $F_{\rm var}$ histogram of the broad emission lines for our spectroscopic sample with a bin width of 0.02. Mean and median of the distributions are represented by vertical lines. 41

6.1 Discrete Correlation Function between the continuum and C IV (top), Si IV (middle) and C III] (bottom) emission lines for quasar J 221516. 47

6.2 Discrete Correlation Function between the continuum and C IV (top), Si IV (middle) and C III] (bottom) emission lines for quasar CTQ 953. 47

6.3 Discrete Correlation Function between the continuum and the C IV (top) and C III] (bottom) emission lines for quasar CTQ 803. The vertical line in each plot indicates the centroid lag $\tau_{\rm cent}$ of the distribution. 47

6.4 $R_{\rm BLR} - L_{\rm UV}$ relation for the UV continuum based on C IV reverberation measurements. CTQ 803, J 221516 (red squares) and S5 0836 (in violet, from Kaspi et al. 2007) are in the upper right corner zoom. Peterson et al (2005) sample are shown as violet dots. The dot-dashed grey line is the relation obtained by Kaspi et al. in 2007 with a slope of 0.52 ± 0.05, while the dashed red line is our fit with a slope of 0.52 ± 0.07. 49

6.5 Black hole masses for CTQ 953 and J 221516 using the Si IV emitting line region versus bolometric luminosity. 51

6.6 Black hole masses for CTQ 803 and J 221516 using the C IV emitting line region versus bolometric luminosity. 51

6.7 Black hole mass for CTQ 803 using the C III] emitting line region versus bolometric luminosity. 52

6.8 Weighted mean of black hole masses for CTQ 803, CTQ 953 and J 221516 using the available emission lines for each object versus bolometric luminosity. 52

A.1 Light curve of the continuum and BLR emission lines of J 002830. To date there is only one measurement for the C IV emission line, thus only its continuum light curve is shown. Y axis corresponds to the residual magnitude according to (3.16). 60

A.2 Light curve of the continuum and BLR emission lines of CTQ 286 60

A.3 Light curve of the continuum and BLR emission lines of CTQ 320 60
A.4 Light curve of the continuum and BLR emission lines of CTQ 367 61
A.5 Light curve of the continuum and BLR emission lines of CTQ 406 61
A.6 Light curve of the continuum and BLR emission lines of CTQ 564 61
A.7 Light curve of the continuum and BLR emission lines of CTQ 650 61
A.8 Light curve of the continuum and BLR emission lines of CTQ 803 62
A.9 Light curve of the continuum and BLR emission lines of CTQ 953 62
A.10 Light curve of the continuum and BLR emission lines of CTQ 975 62
A.11 Light curve of the continuum and BLR emission lines of CTQ 1061 62
A.12 Light curve of the continuum and BLR emission lines of HB89 [0325-385] 63
A.13 Light curve of the continuum and BLR emission lines of J 214355 63
A.14 Light curve of the continuum and BLR emission lines of J 221516 63
A.15 Light curve of the continuum and BLR emission lines of J 224743 63
A.16 Continuum differential light curve in the *R* band of CTQ 252 64
A.17 Continuum differential light curve in the *R* band of CTQ 250 64
A.18 Continuum differential light curve in the *R* band of J 001743 64
A.19 Continuum differential light curve in the *R* band of CTQ 500 64
A.20 Continuum differential light curve in the *R* band of CTQ 261 65
A.21 Continuum differential light curve in the *R* band of CTQ 299 65
A.22 Continuum differential light curve in the *R* band of CTQ 272 65
A.23 Continuum differential light curve in the *R* band of CTQ 391 65
A.24 Continuum differential light curve in the *R* band of CTQ 656 65
A.25 Continuum differential light curve in the *R* band of J 222006 65
A.26 Continuum differential light curve in the *R* band of CTQ 491 66
A.27 Continuum differential light curve in the *R* band of CTQ 481 66
A.28 Continuum differential light curve in the *R* band of CTQ 504 66
A.29 Continuum differential light curve in the *R* band of J 221814 66

A.30 Continuum differential light curve in the *R* band of CTQ 280 66
A.31 Continuum differential light curve in the *R* band of CTQ 322 66
A.32 Continuum differential light curve in the *R* band of CTQ 460 67
A.33 Continuum differential light curve in the *R* band of J 023805 67
A.34 Continuum differential light curve in the *R* band of CTQ 291 67
A.35 Continuum differential light curve in the *R* band of CTQ 412 67
A.36 Continuum differential light curve in the *R* band of CTQ 682 67
A.37 Continuum differential light curve in the *R* band of J 003354 67
A.38 Continuum differential light curve in the *R* band of CTQ 247 68
A.39 Continuum differential light curve in the *R* band of CTQ 1060 68
A.40 Continuum differential light curve in the *R* band of CTQ 296 68
A.41 Continuum differential light curve in the *R* band of CTQ 480 69
A.42 Continuum differential light curve in the *R* band of CTQ 260 69
A.43 Continuum differential light curve in the *R* band of CTQ 452 69
A.44 Continuum differential light curve in the *R* band of CTQ 872 69
A.45 Continuum differential light curve in the *R* band of J 233133 70
A.46 Continuum differential light curve in the *R* band of CTQ 493 70
A.47 Continuum differential light curve in the *R* band of CTQ 830 70
A.48 Continuum differential light curve in the *R* band of CTQ 814 70
A.49 Continuum differential light curve in the *R* band of CTQ 783 70
A.50 Continuum differential light curve in the *R* band of CTQ 498 70
A.51 Continuum differential light curve in the *R* band of CTQ 400 71
A.52 Continuum differential light curve in the *R* band of CTQ 408 71
A.53 Continuum differential light curve in the *R* band of J 235340 71
A.54 Continuum differential light curve in the *R* band of CTQ 599 71
A.55 Continuum differential light curve in the *R* band of CTQ 509 71
A.56 Continuum differential light curve in the *R* band of G 2912 71

B.1 Spectrum of CTQ 286 (top), its comparison star (middle) and the normalized QSO spectrum (bottom). . . . 73

B.2 Spectrum of CTQ 320 (top), its comparison star (middle) and the normalized QSO spectrum (bottom). . . . 73

B.3 Spectrum of CTQ 367 (top), its comparison star (middle) and the normalized QSO spectrum (bottom). . . . 73

B.4 Spectrum of CTQ 406 (top), its comparison star (middle) and the normalized QSO spectrum (bottom). . . . 73

B.5 Spectrum of CTQ 564 (top), its comparison star (middle) and the normalized QSO spectrum (bottom). . . . 74

B.6 Spectrum of CTQ 650 (top), its comparison star (middle) and the normalized QSO spectrum (bottom). . . . 74

B.7 Spectrum of CTQ 803 (top), its comparison star (middle) and the normalized QSO spectrum (bottom). . . . 74

B.8 Spectrum of CTQ 953 (top), its comparison star (middle) and the normalized QSO spectrum (bottom). . . . 74

B.9 Spectrum of CTQ 975 (top), its comparison star (middle) and the normalized QSO spectrum (bottom). . . . 75

B.10 Spectrum of CTQ 1061 (top), its comparison star (middle) and the normalized QSO spectrum (bottom). . . . 75

B.11 Spectrum of HB89 [0325-385] (top), its comparison star (middle) and the normalized QSO spectrum (bottom). 75

B.12 Spectrum of J 214355 (top), its comparison star (middle) and the normalized QSO spectrum (bottom). . . . 75

B.13 Spectrum of J 221516 (top), its comparison star (middle) and the normalized QSO spectrum (bottom). . . . 76

B.14 Spectrum of J 224743 (top), its comparison star (middle) and the normalized QSO spectrum (bottom). . . . 76

B.15 Spectrum of CTQ 564 (top), its comparison star (middle) and the normalized QSO spectrum (bottom). . . . 76

List of Tables

1.1 UV Broad Emission Lines Ionization Potentials . . . 3

2.1 Sample Characteristics . . . 11

2.2 Sample Characteristics (continued) . . . 12

2.3 0.9m Telescope Tek CCD characteristics . . . 14

2.4 C100' (duPont) and SOAR CCD Instruments Characteristics . . . 16

3.1 Imaging observing runs . . . 20

3.2 Imaging observing runs (continuation) . . . 20

4.1 Spectroscopic observing runs . . . 28

4.2 Flux, Luminosity and Cosmological measurements from the spectroscopic sample Redshift has been calculated from the C IV λ1549 in the spectra. CTQ 564 does not have a calibration yet. . . . 34

4.3 Wavelength Windows and Emission Lines Widths The wavelengths are in the observer's reference frame. . . . 35

5.1 Variability Measurements . . . 42

5.2 Variability Measurements – Continued . . . 43

5.3 Variability Measurements – Continued . . . 44

6.1 Preliminary Rest Frame Time Lags from Time-Series Analysis . . . 46

6.2 Preliminary Rest-Frame Lag, Line Width, Virial Product and Black Hole Mass . . . 50

6.3 Bolometric Luminosity and Accretion Rates . . . 51

1

Introduction

1.1 Active Galactic Nuclei

The term *Active Galactic Nuclei (AGN)* refers to energetic phenomena seen in the center of $\sim 10\%$ of the galaxies and that can not be explained by stellar processes. In fact, there is wide consensus and plenty of evidence that AGNs are due to accretion of matter onto a super massive black hole (SMBH).

AGNs are seen in galaxies as unresolved point sources at their centers. The *spectral energy distribution (SED)* of them covers all the electromagnetic spectrum, from gamma and X-rays to radio wavelengths. We can classify AGNs basically by their luminosities:

Seyfert (Sy) Galaxies owe their names to Carl Seyfert who was the first in studying the spectra of these objects in the early 1940's. They are galaxies that harbor a low or intermediate luminosity AGN ($M_B > -21.5$) with a clear detectable host galaxy. Among Seyferts, two types can be found depending on their spectral features: **Type 1 Sy**, for which their spectra is composed by a superposition of a power law continuum, broad and narrow emission lines of high ionization species. In contrast, **Type 2 Sy** show only narrow forbidden lines in their spectra.

Quasars Thanks to the rapid advance of radio astronomy in the 1960's, point like sources were discovered with broad and narrow emission lines in their optical spectra. They were called *quasi stellar objects (QSO)* or simply *quasars*. It took a while to identify those emission lines with the same lines observed in Sy 1 but redshifted. Nowadays, the term quasar refers to the high luminosity subclass of AGNs ($M_B < -21.5$) with broad emission lines and stronger power law continuum than Sy 1 galaxies.

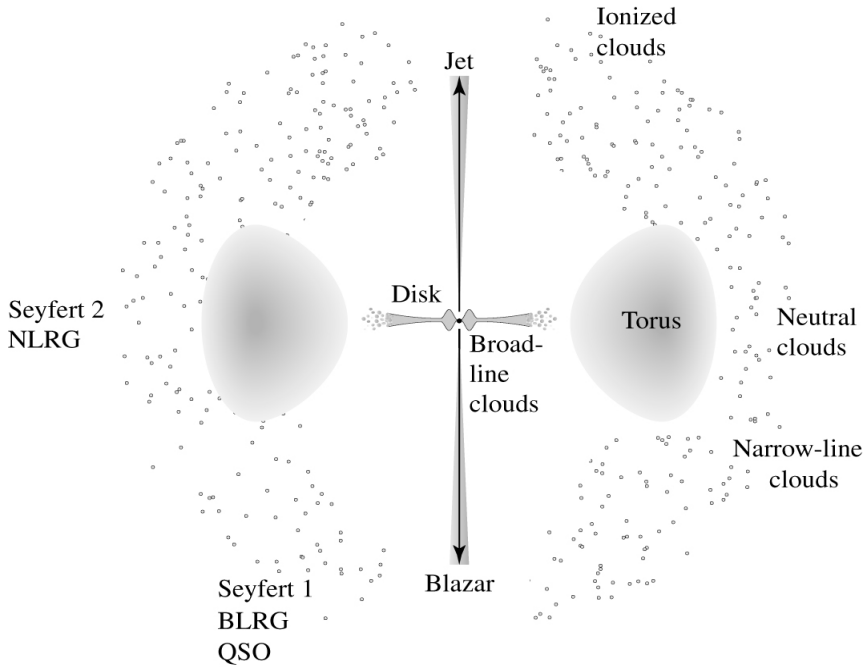

FIGURE 1.1: Unified model of the central engine of an AGN (From Carroll & Ostlie).

Seyferts and quasars form a special class of galaxies called *active galaxies*. Seyferts are generally early type spiral galaxies and are common in the local universe ($z \lesssim 0.5$) while quasars are rare locally and correspond to active galaxies at higher redshifts which are generally unresolved, so that their host galaxy are very faint if seen.

The different types of AGN (Sy 1 and Sy 2) can be understood in the frame of the unified model shown in figure 1.1. In this model, gravitational energy is released by accretion of matter onto a SMBH from an accretion disk. A nearby region filled by gas clouds are responsible for the broad emission lines and is called the *broad line region (BLR)*. Other components of the AGNs are the *dusty torus* which radiates in the IR rest frame part of the spectrum and the *narrow line region (NLR)* responsible of the narrow emission lines in the spectra. Different viewing angles between the line of sight and the central engine produce the different types of AGNs. As seen in 1.1, the BLR is obscured by the dusty torus in type 2 Seyferts, and then no broad lines are seen in the spectra. Nevertheless, the black hole paradigm has been also shown to apply to Sy type 2 from broad emission lines seen in polarized flux.

One of the first properties found in active galaxies was their variability in every spectral band where they have been observed (from X rays to radio). Variability is a powerful tool to study the physics of the central engine of AGNs, in particular the broad line region, one of the dominant features of AGN spectra.

In what follows, "UV" and "optical" refer to these same bands (centered at 1350Å and 5100Å, respectively) in the rest frame of the AGN.

1.1.1 The Broad Line Region: what we know.

The broad emission lines in AGNs spectra can not be explained by thermal processes. Actually, the emission lines observed in AGN are similar than those of other plasmas such as planetary nebulae and HII regions which are basically under photoionization equilibrium. This equilibrium is reached at $T \sim 10^4$ K which implies a thermal width of $\sim 10\,\mathrm{km\,s^{-1}}$ for the emission lines. However, AGN spectra show very broad emission lines with velocities of the order $v_{FWHM} \sim 500\,\mathrm{km\,s^{-1}}$ in low luminosity Seyferts to $\sim 10^4\,\mathrm{km\,s^{-1}}$ reaching up to $30000\,\mathrm{km\,s^{-1}}$ which implies a doppler broadening caused by gas moving supersonically.

A lower density limit for the BLR clouds is given by the absence of O III] forbidden lines for which the critical density is of the order of $\sim 10^8\,\mathrm{cm^{-3}}$. The presence of C III] in turn gives an upper limit of $\sim 10^{10}\,\mathrm{cm^{-3}}$. However, some studies have shown that the C III] emission comes from a different part of the BLR than Ly α and CIV. A fiducial density value of $10^{11}\,\mathrm{cm^{-3}}$ is actually accepted for the region where Ly α and C IV are produced. Table 1.1 show the UV emission lines of the BLR and their ionization potentials.

TABLE 1.1: UV BROAD EMISSION LINES IONIZATION POTENTIALS

Ion	Wavelength (Å)	Ionization Potential (eV)
Lyα	1216	13.6
Si IV	1400	33.5
C IV	1549	47.9
He II	1640	24.6
C III]	1909	24.4

Only a modest amount of mass of $\sim 10\,M_\odot$ forms the BLR despite the strong emission it produces. It is common to refer to the BLR structure as clumpy, formed by many gas clouds orbiting around the BH. The BLR is unresolved even for the nearest AGNs, so it must be very close to the central BH as expected from the emission line widths with $R_{\mathrm{BLR}} \sim 100\,R_S$, where R_S is the Schwartchild radius of the BH. Its variability time scale constrains its size and can be used to probe the central engine.

1.1.2 Reverberation Mapping

Black hole masses in AGN are obtained using a technique proposed by Blandford and McKee (1982) called *Reverberation Mapping (RM)*.

Reverberation mapping uses the lag between variations in the central ionizing source and the response of the Broad Line Region (BLR) emission lines to directly measure the BLR size (Kaspi et al., 2000, Peterson et al., 2004, Kaspi et al., 2004). Assuming a gravitationally bound system and measuring the BLR line widths, it is possible to infer the mass of the central BH. It is based on three basic assumptions:

1. *The ionizing continuum originates in a single central source.*

This holds because the BLR size is ∼2 orders of magnitude larger than the continuum source (the accretion disk).

2. *The light travel time across the BLR is the most important time scale.*

   Given that the recombination time is related with the electron density n_e by the relation $\tau_{rec} \approx 0.1(10^{10}\ \mathrm{cm}^{-3}/n_e)\ \mathrm{hr} \approx 0.1$ hr, which is negligible compared with much less than the typical light travel time across the BLR, the response of the cloud can be considered instantaneous.

3. *There is a simple but not necessary linear relationship between the observed continuum and the ionizing continuum (which gives rise to the emission lines).*

From these points one can construct a simple 1D linear model given by

$$L(t) = \int \Psi(\tau) C(t-\tau) d\tau \tag{1.1}$$

where $L(t)$ and $C(t)$ are the line and continuum light curves respectively. $\Psi(\tau)$ is the *transfer function* (TF) which holds information about the geometry and kinematics of the BLR gas, so, in principle, $\Psi = \Psi(\tau, v, r)$. Due to technical limitations, the TF is collapsed to one single parameter: the time lag τ between both continuum and line light curve variations which is obtained through a cross-correlation analysis between them (Peterson 2001).

1.1.2.1 Broad Line Region size and Black Hole properties

Reverberation mapping has allowed to measure BH masses in AGNs mainly thanks to the optical monitoring of the Hβ line in the local universe. Typical time scales for variability in Seyfert galaxies are of order of few months from which we can constrain their BLR size using

$$R_{\mathrm{BLR}}(\mathrm{H}\beta) = c\,\tau_{\mathrm{H}\beta} \tag{1.2}$$

where c is the speed of light and $\tau_{\mathrm{H}\beta}$ is the time lag between the continuum and the Hβ line changes. Furthermore, the BLR size has been used to directly measure the central black hole mass assuming a virialized state of the gas. A BLR cloud is said to be virialized when it is in gravitational equilibrium with the deep potential of the BH, and therefore its velocity is related to the its distance from the SMBH in such a way that $\mathrm{v} \propto R_{\mathrm{BLR}}^{-1/2}$ which is equivalent to $\mathrm{v} \propto \tau^{-1/2}$. This assumption has proven to be correct for those objects with measurements in several lines: the observed anti-correlation between the line Doppler widths and their distance from the central black hole is consistent with virialized motion of the BLR gas in the deep potential of the central BH (Onken & Peterson 2002), as shown in figure 1.2. Since the BLR is virialized, we can infer the central black hole mass from

$$M_{\mathrm{BH}} = f\,\frac{R_{\mathrm{BLR}}\,\mathrm{v}^2}{G} \tag{1.3}$$

where R_{BLR} and v^2, the BLR size and doppler velocity, are measured for a particular emission line and f is a factor ~ 1 to take into account the geometrical distribution of the gas and G is the universal gravitational constant. It is usual to express reverberation masses in terms of the *virial product* defined as

$$VP = \frac{R_{\mathrm{BLR}}\,\mathrm{v}^2}{G} \tag{1.4}$$

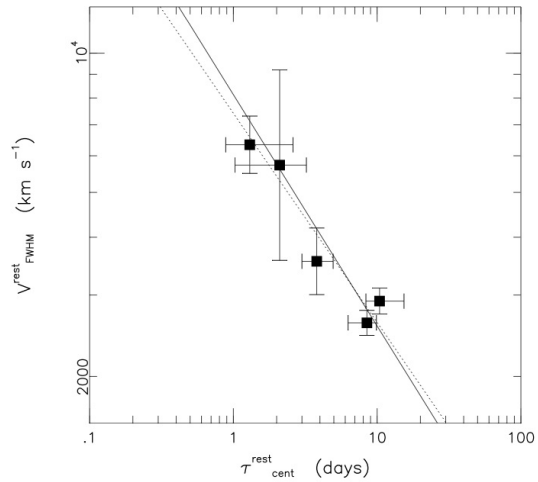

FIGURE 1.2: Rest frame velocity v_{FWHM} versus rest frame centroid time lag τ for five BLR emission lines in NGC 3783. The dashed line is the best fit to the data; the solid line is the best fit with fixed slope of -0.5, consistent with a virialized BLR. From Onken & Peterson 2002.

that is, the virial mass of the BH.

In addition we can estimate the accretion rate of the AGN using the Eddington luminosity defined as the maximum luminosity that accretion onto the BH can radiate to avoid a radiative disintegration of the accretion flow an given by

$$L_{\rm Edd} = \frac{4\pi G c m_p}{\sigma_e} M \approx 6.3\times10^4\ M\ {\rm erg\,s^{-1}} \tag{1.5}$$

where m_p and σ_e are the proton mass and the Thomson scattering cross section respectively and M is the mass of the BH in grams. If mass is measured in solar masses, then

$$L_{\rm Edd} = 1.25\times10^{38}\left(\frac{M}{\rm M_\odot}\right){\rm erg\,s^{-1}} \tag{1.6}$$

As mentioned above, AGN luminosity comes from the energy released by the accretion of mass M onto the central object. Then, the luminosity is given by

$$L = \eta \dot{M} c^2 \tag{1.7}$$

where η is the accretion efficiency, which theoretically depends on the type of BH (Schwarchild or Kerr BH), being $\eta \sim 0.1$ a standard value. Combining (1.6) and (1.7) the accretion rate $\dot{M}_{\rm Edd}$ depends on the BH mass and accretion efficiency according to

$$\dot{M}_{\rm Edd} \approx \frac{2.2}{\eta}\left(\frac{M}{10^9\,{\rm M_\odot}}\right){\rm M_\odot\ yr^{-1}} \tag{1.8}$$

Then, measuring the BLR size and the velocity of an emission line we can have direct estimates of the central BH properties such as its mass and the Eddington accretion rate. If in addition we knew the bolometric luminosity $L_{\rm bol}$ of the source, we could estimate the accretion efficiency in terms of $\dot{M}_{\rm Edd}$.

1.2 Scaling Relations

Using the simple assumption that all AGN have the same parameters (ionization parameter, density of the BLR clouds), a simple scaling relation between the BLR size and the luminosity $R_{\rm BLR} \propto L^{0.5}$ can be derived (Peterson 2001). Using a large sample of ~ 30 AGN with BH masses estimated from reverberation mapping based on the Hβ line, Kaspi et al. (2000, 2005) found that the BLR size scales with luminosity according to

$$\frac{R_{\rm BLR}\,({\rm H}\beta)}{10\,{\rm lt-days}} = (2.23 \pm 0.21)\left[\frac{\lambda L_\lambda(5100\,\text{Å})}{10^{44}\,{\rm erg\,s^{-1}}}\right]^{0.69\pm0.05} \tag{1.9}$$

Vestergaard (2002) proposed that BH mass, particularly at high redshifts, can be derived from single epoch spectroscopic observations to obtain specific luminosity and line widths and using an extrapolation of the $R_{\rm BLR} - L$ relation. This was the first attempt to study the demography of BHs in AGNs at all redshifts. However, higher redshifts implies that optical lines are redshifted into the IR window. Thus, other emission lines apart of the Hβ have been used. A handful BH masses are available based on reverberation mapping using Mg II λ2798 , although the line shifts to the IR at modest redshifts ($z \gtrsim 1.5$).

Rest frame UV emission lines can be used to study high redshift AGNs when they fall in the optical band. In particular, C IV λ1549 has been used to measure black hole masses in nearby AGN using the UVE satellite (UV Explorer) (Peterson 2004, Kaspi 2007). Kaspi et al. (2007) started a reverberation program for 11 high luminosity high redshift sources. Only one quasar showed enough variability to estimate its BLR size. Adding this source to the Peterson et al. (2004) C IV sample Kaspi et al. found

$$\frac{R_{\rm BLR}\,({\rm C\,IV})}{10\,{\rm lt-days}} = (0.17 \pm 0.04)\left[\frac{\lambda L_\lambda(1350\,\text{Å})}{10^{43}\,{\rm erg\,s^{-1}}}\right]^{0.52\pm0.04} \tag{1.10}$$

The $R_{\rm BLR} - L$ relations based on both Hβ and C IV emission lines are shown in figures 1.3 and 1.4. Despite both slopes have been measured, it is clear that the optical relation is statistically more reliable than the one in the UV given the number of AGNs in the plot. Therefore, more points are necessary to have a reliable $R_{\rm BLR} - L$ relation in the UV from which we can estimate BH masses from optical spectra of sources at redshifts of cosmological interest ($z > 1$).

1.3 Galaxy Evolution and Black Holes Demography

Despite great advances in our understanding of galaxy evolution in recent years, this is still controversial subject in modern astronomy. Today it is widely accepted that all massive galaxies harbor SMBH in their centers. Evidence of that are found in nearby quiescent galaxies using stellar and gas dynamics at the very center of them. Two clear examples are the BH found at the center of the Milky Way with a mass $\sim 4\times10^6\,{\rm M}_\odot$ and a direct observation of a water mega maser in the center of NGC 4258 (Maloney 2002).

There are many indicators that the evolution of galaxies is intimately coupled with the BH growth. This can be inferred from the tight relations found between the central BH mass and the large scale properties of the host galaxy (mainly

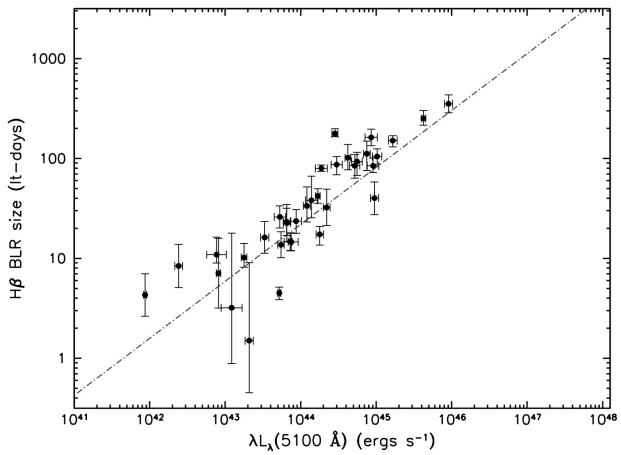

FIGURE 1.3: $R_{\rm BLR} - L$ relation based on Hβ line and $\lambda L_\lambda(5100\,\text{Å})$ form Kaspi et al. 2005. The slope is 0.69 ± 0.05.

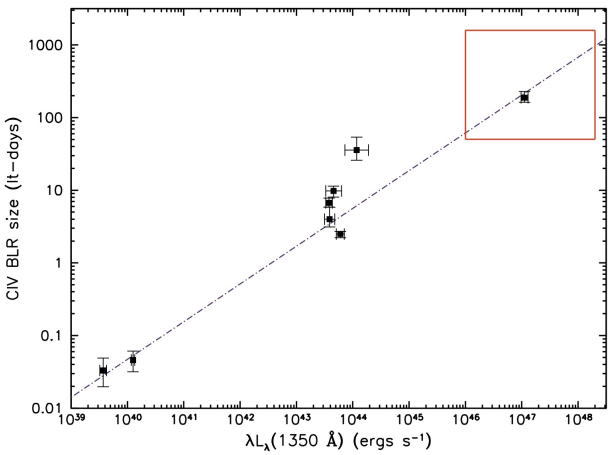

FIGURE 1.4: $R_{\rm BLR} - L$ relation using the C IV line and $\lambda L_\lambda(1350\,\text{Å})$ form Kaspi et al. 2007. The slope is 0.52 ± 0.04.

the spheroidal component), like the $M_{\rm BH} - \sigma_\star$ and the $M_{\rm BH} - M_{\rm bulge}$ relations (Woo et al. 2010) as well as from the coupling in the comoving QSO space density with the *star formation rate (SFR)*, very similar in shape and both with a peak at $z \sim 2.5$. In that sense, BH demography and its evolution with redshift can provide us with several constraints about the physical evolution of quasars and their relation to the formation of structure in the universe.

Reverberation mapping has played a central role in estimating black hole masses and deriving the BLR size-luminosity relation in AGN, allowing real physical comparison between active and dormant BHs in the local universe. Furthermore, it seems that dormant and active BHs follow the same scaling relations in the nearby universe. Netzer (2003) pointed out that, if we extrapolate the results of Kaspi et al. to high redshifts we can expect BH masses as large as $\sim 10^{10}\,\text{M}_\odot$. Using the scaling relations between the BH and its host galaxy, then we could expect galaxy masses of order of $\sim 10^{13}\,\text{M}_\odot$ and stellar velocity dispersions of $\sim 800\,\text{km s}^{-1}$. Such galaxies have never been observed and are not expected to exist under standard galaxy formation theories. However, the high redshift BH demography to confirm or rule out these scenarios is still unknown.

A plausible suggestion is that one or some conversion factors can not be extrapolated to such high redshifts. In fact, Woo et al. (2009) showed that there seems to be some evolution of these scaling relations with redshift. Nevertheless, all BH mass estimations are based on an extrapolation of (1.9) which has not be reliably tested at the high luminosity end. Therefore, direct measurements of BH properties at high redshifts are desirable.

1.4 This Thesis

In this thesis I expect to set up a baseline work for future reverberation mapping of several high luminosity sources at high redshift, which consists in the identification of a subsample of high variable objects within a large sample from which we can obtain reliable estimations of their BLR size. From this subsample it is expected to obtain BH masses and accretion rates not for one, but several sources which will be a huge advance for the statistical analysis for the

$R_{\rm BLR} - L$ relation especially at high luminosity (red square in figure 1.4), which will allow us to confirm or rule out the present trend and for the general study of the high redshift universe.

The optical monitoring of a large sample of high luminosity quasars started as a collaborative work between Paulina Lira, Hagai Netzer and Shai Kaspi who defined, based on their previous experience, the overall design for monitoring campaign and the quasar sample selection. I came into this project in the very beginning after starting the first imaging observations in march of 2005. Since then, I have been in charge of the whole data reduction, the imaging observation arrangements and the spectroscopic observations. This thesis is the result of my work during this almost 6 years.

This work is divided as follows: I will describe the motivation, observational strategy and instruments defined by the group in chapter 2. My work on the data reduction for the imaging and spectroscopic monitoring of the sample is described in chapters 3 and 4 respectively. The light curves I have obtained from the data processing of both imaging and spectroscopic monitoring are shown in appendix A. The variability estimators and measurements that I have used for the variability characterization of the sample are described in chapter 5. An analysis of both, continuum and emission lines quasar variability is also presented. Preliminary lags, black hole masses and accretion rates for three sources are presented in chapter 6. I finally outline the conclusions in chapter 7.

I assumed throughout this work a standard ΛCDM cosmology with $H_0 = 70\,{\rm km\,s^{-1}\,Mpc^{-1}}$, $\Omega_\Lambda = 0.7$ and $\Omega_M = 0.3$.

2

High Luminosity Quasar Monitoring Campaign

The empirical relation found in previous works between BLR size ($R_{\rm BLR}$) and AGN luminosity has produced reliable black hole mass estimates for a large number of AGNs at low and intermediate luminosity ($\lesssim 10^{46}\,{\rm erg\,s^{-1}}$) in the local universe ($z \lesssim 0.5$, Kaspi et al. 2000, hereafter K00). On the other hand, the ability to measure black hole masses and accretion rates in AGNs becomes crucial at high redshifts ($z > 1$) which are of cosmological interest in the context of galaxy evolution. In that way, the $R_{\rm BLR} - L$ relation would allow us to estimate from a single epoch spectroscopic observation black hole masses and accretion rates through cosmic history only by extrapolating this relation in luminosity (Vestergaard 2002).

However, such extrapolation, by up two orders of magnitude, might not be reliable because it strongly depends on the untested assumption that the $R_{\rm BLR} - L$ relation is also valid at high redshift. Therefore, reverberation mapping of high luminosity sources is needed to probe the expected trend.

So far the few attempts to carry out reverberation mapping of very high luminosity quasars have failed mainly for two reasons: **1.** Statistically, high luminosity sources are less variable in terms of amplitude and time scale (Vander Berk et al. 2004). **2.** The line variability amplitude is even smaller than the continuum amplitude because the emission line response is averaged over the large ($\sim$ 1 pc) BLR geometry, and then only highly variable objects are useful in order to measure accurate emission line variations.

In this thesis I summarize the efforts, techniques and preliminary results of a long term monitoring campaign of high luminosity quasars designed to probe the BLR size and BH mass at the highest redshifts ever measured, with a new observational strategy that, so far, has led to encouraging preliminary results which will need to be confirmed in the near future. When this long-term project is concluded, reverberation studies will cover the luminosity range of 10^{41}–

$10^{47.5}\,\mathrm{erg\,s^{-1}}$, almost two orders of magnitude higher in luminosity than the K00 sample, spanning the whole AGN luminosity range.

2.1 Observational Strategy

This long term monitoring project is a challenging task due the low amplitude and slow varying properties of high luminosity sources. Furthermore, emission line variability amplitude is even smaller than that observed in the continuum. In order to maximize the probability of finding variable sources, we have undertaken a novel strategy that combines small and medium size telescopes based on a "target of opportunity" approach.
First, broad band imaging monitoring of a sizeable sample of sources is conducted in order to find highly variable sources. If quasars are variable enough, a spectroscopic monitoring is triggered in order to follow this variability in the broad emission lines. More details are given in section §2.5. This observational approach has led to the identification of a subsample suitable for reverberation studies.

2.2 Quasars Sample

The main selection criteria was the high luminosity of the sources. The final sample is composed of the brightest quasars with luminosities greather than $\lambda L_\lambda(1350\,\text{Å}) \gtrsim 10^{46.5}\,\mathrm{erg\,s^{-1}}$ from the Calán-Tololo (Maza et al. 1993, 1995a, 1995b, 1996), Two Micron All Sky Survey (2MASS, Wayne B. & Hall P. 2001) and 2dF Quasar Redshift Survey (2QZ, Croom et al. 2004) catalogues giving 56 optically selected, unobscured sources. Since high luminosity sources are actually found at high redshift because of the strong cosmological evolution shown by these sources (Boyle et al. 1998), the sample redshift range is between $2.3 \lesssim z \lesssim 3.4$. Also, existing spectra of the targets were inspected to ensure that all of them showed strong broad emission lines suitable for reverberation measurements. At those redshifts broad UV emission lines are shifted into the optical window. Consequently, the monitoring campaign is optical in nature. The sample characteristics are summarized in tables 2.1 and 2.2. Right ascension, declination and redshift are tabulated in columns (2), (3) and (4). Instrumental magnitudes in the *R* filter are listed in column (5). Column (6) corresponds to the angular separation between the quasar and the comparison star, with an accuracy $\lesssim 5$ arc sec. Quasars with two comparison stars are marked in red. Column (7) correspond to the quasar-comparison star Cassegrain Ring position (see section §2.5).

TABLE 2.1: SAMPLE CHARACTERISTICS

Object	R.A. (J2000.0)	Dec. (J2000.0)	Redshift	m_R	R_{comp} (arc sec)	P.A.$_{comp}$ (degrees)
(1)	(2)	(3)	(4)	(5)	(6)	(7)
CTQ 803	00 04 48.16	-41 57 28.2	2.76	17.117	89	214.4
J001743.9-293604 . . .	00 17 43.9	-29 36 04	2.84	17.499	71	178.9
J002830.4-281706 . . .	00 28 30.5	-28 17 06	2.40	17.279	202	161.4
J003354.7-295754 . . .	00 33 54.8	-29 57 54	2.66	17.674	164	192.3
CTQ 406	00 34 26.84	-37 12 52.4	3.18	17.773	153	150.4
CTQ 504	00 35 18.33	-52 49 08.2	2.70	17.075	119	180.7
CTQ 408	00 41 31.49	-49 36 12.4	3.24	15.944	148	203.1
CTQ 814	00 44 16.94	-31 14 38.2	2.34	17.442	240	203.7
CTQ 509	01 11 43.51	-35 03 01.4	2.41	17.125	93	148.9

TABLE 2.2: SAMPLE CHARACTERISTICS (CONTINUED)

Object	R.A. (J2000.0)	Dec. (J2000.0)	Redshift	m_R	R_{comp} (arc sec)	P.A.comp (degrees)
(1)	(2)	(3)	(4)	(5)	(6)	(7)
CTQ 412	01 41 53.71	-33 24 17.0	2.51	18.087	40	197.8
CTQ 830	02 00 31.51	-31 48 21.2	2.33	16.909	146	204.7
J023805.8-274337 . . .	02 38 05.8	-27 43 38	2.45	16.723	92	156.7
HB89[0329-385]	03 31 06.3	-38 24 05	2.43	17.605	181 / 259	143.0 / 164.0
CTQ 247	04 07 18.01	-44 10 29.7	3.00	17.236	65	189.1
CTQ 872	04 08 12.62	-34 37 49.0	3.1	17.395	146	205.1
CTQ 250	04 11 45.18	-42 54 44.2	2.40	17.561	96	151.2
CTQ 252	04 18 10.44	-45 32 17.6	2.5	16.409	105	183.4
G2912.	04 32 14.34	-49 44 57.9	2.7	19.315	91	168.7
CTQ 260	04 45 52.02	-31 58 43.4	3.00	16.879	173	176.3
CTQ 261	04 46 58.88	-41 46 01.9	2.70	17.049	123	175.1
CTQ 650	04 55 22.98	-42 16 17.1	2.66	17.021	151	230.5
CTQ 272	05 48 02.49	-35 42 27.9	2.45	16.954	100	181.9
CTQ 452	05 54 45.76	-33 05 17.0	2.36	15.491	124	178.8
CTQ 656	06 00 08.07	-50 40 36.8	3.13	17.306	85	189.7
CTQ 280	09 39 51.20	-18 32 15.9	2.4	16.727	61	164.1
CTQ 286	10 17 23.90	-20 46 58.5	2.80	16.905	85	177.4
CTQ 291	10 33 59.93	-25 14 26.7	2.9	16.545	146	179.5
CTQ 460	10 39 09.51	-23 13 25.7	3.13	16.76	171	190.1
CTQ 1060	10 41 33.46	-20 33 15.2	3.00	17.333	171	167.7
CTQ 1061	10 48 56.73	-16 37 09.5	3.37	16.163	48	185.3
CTQ 296	10 58 09.31	-26 05 42.3	3.0	17.272	44 / 100	170.8 / 162.0
CTQ 299	11 24 42.81	-17 05 18.0	2.95	16.008	106	171.8
CTQ 320	13 17 44.16	-31 47 13.3	3.10	17.895	138	174.4
CTQ 322	13 25 18.16	-29 50 45.0	2.44	17.648	52	194.1
J214355.0-295158 . . .	21 43 55.1	-29 51 59	2.62	17.131	161	198.9
CTQ 564	21 50 15.97	-44 11 23.9	2.66	16.939	125	213.4
CTQ 953	21 59 54.72	-40 05 50.4	2.52	16.888	168	143.0
CTQ 367	22 00 36.26	-35 02 17.7	2.70	16.794	157	163.8
J221516.0-294424 . . .	22 15 16.02	-29 44 23.3	2.70	16.618	142	192.0
J221814.4-300306 . . .	22 18 14.5	-30 03 07	2.38	17.411	62	163.5
J222006.7-280324 . . .	22 20 06.77	-28 03 23.4	2.41	15.648	170	191.4
CTQ 975	22 38 13.28	-32 48 24.2	2.86	17.563	129	183.6
J224743.5-310306 . . .	22 47 43.6	-31 03 07	2.61	16.652	173	229.8
CTQ 480	22 52 44.03	-50 21 38.2	2.90	16.784	56	156.2
CTQ 391	22 53 10.77	-36 58 16.6	3.20	17.891	107	193.8
CTQ 481	22 56 54.81	-35 52 51.9	2.64	17.734	136	188.0
CTQ 682	23 07 17.18	-42 03 19.4	2.63	16.955	229	203.2
CTQ 783	23 09 18.72	-51 18 15.2	2.59	16.69	199	195.0
CTQ 491	23 26 06.46	-35 34 50.0	2.43	16.839	91	156.5
J233133.4-274842 . . .	23 31 33.5	-27 48 42	2.66	16.268	90	215.5
CTQ 493	23 40 05.34	-36 16 30.9	2.43	17.824	142	164.6
CTQ 599	23 42 35.52	-55 34 39.2	2.70	16.401	191	166.6
CTQ 498	23 50 34.21	-43 25 59.6	2.9	16.325	172	183.5
CTQ 500	23 52 11.34	-32 59 07.5	2.45	17.997	241	178.3
J235340.3-292436 . . .	23 53 40.3	-29 24 36	2.35	17.213	60	178.1
CTQ 400	23 58 09.22	-46 05 00.5	2.37	16.774	141	170.7

2.3 Monitoring Campaign Length

The typical time scale of the BLR emission line variability in high luminosity quasars can be estimated from an extrapolation of previous works. This extrapolation gives us an idea of how long the monitoring campaign should last in order to find enough structure in the light curves needed for reverberation mapping analysis.
Using the $R_{\rm BLR} - L$ relation of Kaspi et al. (2007) for the C IV emission line, in addition to the characteristic luminosity of our sample, we can estimate the BLR size and then a time scale for the variations of their UV emission lines. In the rest frame, the BLR size for a source with $\lambda L_\lambda(1350\,\text{Å}) \sim 10^{47.5}\,\text{erg}\,\text{s}^{-1}$ is found to be

$$R_{BLR} = (1.7 \pm 0.4) \left[\frac{\lambda L_\lambda(1350\,\text{Å})}{10^{43}\,\text{erg}\,\text{s}^{-1}} \right]^{0.52\pm0.04} \text{lt} - \text{days} \approx 370\,\text{lt} - \text{days} \tag{2.1}$$

Thus we can expect that variations in the continuum flux should be followed by changes in the UV emission lines after roughly about a year. In addition, we have to take into account that high luminosity sources are also at high redshift, and therefore, the time scales are lengthened by the $(1+z)$ factor. Using $z = 2.7$ as a typical redshift of the sample, the observed time scale for quasars variability can be estimated to be

$$\tau_{\rm observed} = (1+z)\,\tau_{\rm rest\,frame} \approx 1300\,\text{days} = 3.6\,\text{yrs} \tag{2.2}$$

From time series analysis, a variability monitoring should be at least three times as long as the shortest time scale involved (Peterson 2006), therefore the expected monitoring length is

$$\tau_{\rm monitoring} \sim 3\,\tau_{\rm observed} \approx 10\,\text{yrs} \tag{2.3}$$

Since the observations of the campaign (started in 2005, with only ~ 3 years of spectroscopic monitoring), the project is still halfway through. The identification of variable sources with structured light curves (non monotonic) and preliminary reverberation analysis are discussed in the chapters 5 and 6.

2.4 Comparison with the Work of Kaspi et al. (2007)

The sample in the Kaspi et al. (2007, hereafter K07) monitoring program is composed by 11 high luminosity and high redshift sources ($z \sim 2.2 - 3.2$) located in the northern sky. Their photometric monitoring started in 1995, and the spectroscopic follow up started four years later in 1999, with a total duration of ~ 10 years. K07 found that only one object (S5 0836+71) of the whole sample presented enough structure in their light curves in order to obtain a preliminary lag between the continuum and the C IV emission line (shown in figure 1.4).

Our observational strategy do not differ strongly from the one used by K07. However, our sample is larger by a factor of 5, increasing the probability of finding "highly" variable sources. Therefore, we expect to increase the sources from which the BLR size can be estimated.

2.5 Observations

In the following I describe the two stages in which the campaign is divided: *broad band imaging* and *long slit spectroscopy*.

1. Broad Band Imaging: Broad band imaging is being carried out with the 0.9m Telescope at Cerro Tololo Inter-American Observatory (CTIO) in service mode[1]. Nearly monthly spaced observations are performed giving us a typically 10-11 observing runs per year, 1-2 of which are lost because of weather. Around 5-6 epochs per year are observed for each object.

Quasar fields are observed twice for 250 sec with the broad band *R* filter which has a transmission centered at 6577 Å with an equivalent width of 627 Å. In photometric nights a standard field is observed for 10 and 40 sec in order to have non saturated and well exposed data for bright and faint objects.

A wide CCD field is needed because the flux calibration must be secured through differential photometry between the quasar and a group of $5-10$ nearby field stars. This technique guarantees a photometric precision of $\lesssim 3\%$. General characteristics of the instrument are given in table 2.3.

TABLE 2.3: 0.9M TELESCOPE TEK CCD CHARACTERISTICS

Pixels	2048×2046
FOV (arc min^2)	13.5×13.5
Pixel scale (arc sec/pixel)	0.396
Read Noise (e^-)	3.4
Gain (e^-/ADU)	1.0

2. Long Slit Spectroscopy: Long slit spectroscopy is carried out in observing mode with the Irenee duPont 2.5m Telescope at Las Campanas Observatory (LCO) and with the SOAR 4.1m Telescope at Cerro Pachón. The spectra cover the $4\,000-9\,000$ Å wavelength range with moderate resolution ($R\sim\lambda/\Delta\lambda\approx1\,500-2\,000$). In order to have enough temporal coverage during the year we have teamed up with the CHASE supernova program to share observing nights. This typically gives us 8-10 spectroscopic runs per year.

For the purpose of measuring variability in the emission lines, differential spectroscopy is performed with respect to a nearby star which acts as a comparison standard[2]. Usually, *G*-type stars are preferred over late-type (*K*, *M*) stars because they have a smoother spectrum with weak Balmer absorption lines and fewer absorption bands. However, in the normalization step, the star spectrum is heavily smoothed (see §4.2), so the spectral type is not an important parameter.

The quasar and the comparison star are observed simultaneously along the same slit. This is accomplished by rotating the slit in such a way that both objects are aligned in the center. The Cassegrain Ring angle (CR) needed for this configuration is calculated for the WFCCD instrument using the triangle formed by the North, the comparison star and the quasar, with the latter located in the center of rotation of the field as shown in figure

[1] The 0.9m, 1.0m, 1.3m and 1.5m telescopes at CTIO are operated by the SMARTS consortium.
[2] Finding charts for the comparison stars of the spectroscopic targets are shown in appendix **??**

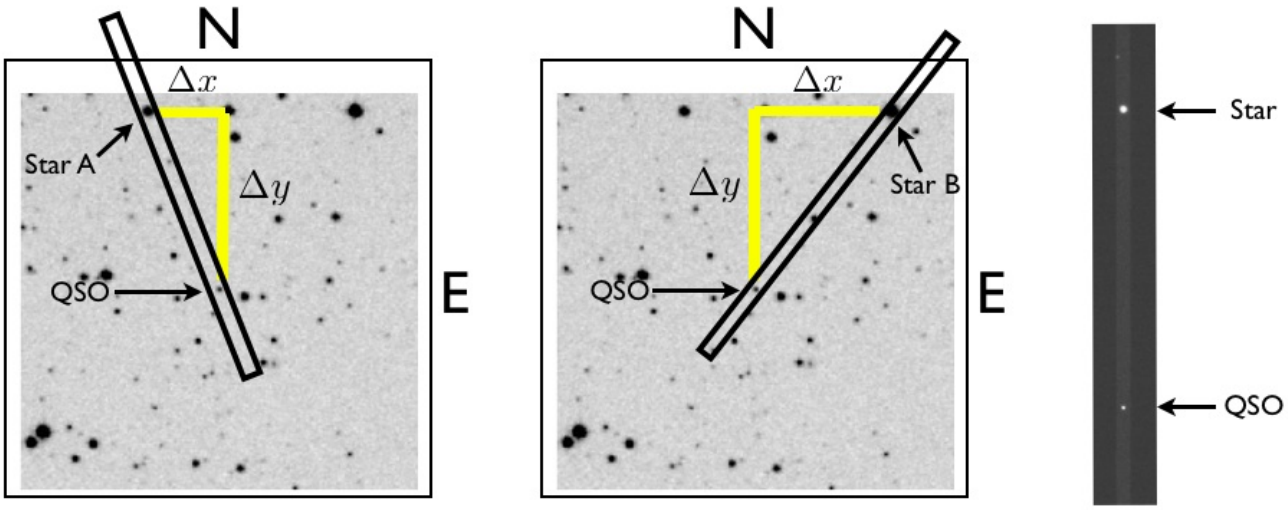

FIGURE 2.1: Cartoon which shows the way to calculate the Cassegrain Ring angle for a particular QSO. North and East are labeled and the slit is represented by the inclined rectangle. QSO is at the center of the image, assumed to be the center of rotation in this example.
In the left panel, the comparison star (A) is at the left, and then the slit has to be rotated clockwise. The middle panel shows the comparison star (B) at the right, so the slit should be rotated counter-clockwise. A snapshot of the acquisition image of a QSO and its comparison star is shown in the right panel. Both targets are perfectly aligned along the wide slit.

2.1, and using the equation

$$CR = 180^{\circ} \pm \arctan\left(\frac{\Delta x}{\Delta y}\right) \tag{2.4}$$

where Δx and Δy stands for the x and y offsets between the star and the quasar respectively. The sign ($\pm$) depends on the direction of the rotation (counter, clock wise).

This configuration ensures line fluxes measurements with a precision of $\sim 2\%$ (Kaspi et al. 2000). Since the resulting position angle is not the parallactic angle at the time of observation, we use a wide slit ($750\mu m \sim$ 9 arc sec) to minimize light losses due atmospheric refraction and any centering problems (see next discussion on the Boller&Chivens spectrograph). A narrow slit ($150\mu m \sim 1.7$ arc sec) is used during arcs exposures for wavelength calibration.

Generally, 3 spectra of 900 sec or 2 exposures of 1200 sec are taken depending on seeing conditions and observing time optimization. Arc lamps are taken for every object at the same position to correct for possible flexures in the telescopes (particularly at high airmasses). An arc lamp at the zenit is used for wavelength calibration of spectrophotometric standard stars spectra.

During the spectroscopic monitoring different instruments have been used, whose details are shown in table 2.4 and their performances are described below. I have been personally involved in most of the spectroscopic monitoring observations except for those observing runs for which the Boller & Chivens spectrograph has been used (see table 4.1).

TABLE 2.4: C100' (DUPONT) AND SOAR CCD INSTRUMENTS CHARACTERISTICS

	WFCCD	Boller & Chivens	Goodman
Pixels	4064×4064	2048×515	4096×4096
Acquisition FOV (arc min^2)	25 (diameter)	2.3×3.1	3×5
Pixel Scale (arc sec/pixel)	0.484	0.70	0.15
Read Noise (e^-)	3.6	4.0	3.99
Gain (e^-/ADU)	0.75	0.7	2.06
Wavelength Range (Å)	3600 – 7600	3100 – 10000	3200 – 8500
Grism (l/mm)	300	300	300
Dispersion (Å/pixel)	3	3	1.3
Slit Length (arc min)	8	4.5	3.9
Wide Slit Width (arc sec)	8.65	8.65	10
Narrow Slit Width (arc sec)	1.65	1.65	1.03
Comparison Lamp	HeNeAr	HeNeAr	HgNeAr

- **WFCCD (Wide Field CCD) camera:**

  Mounted on the 2.5m duPont Telescope at LCO, the WFCCD has proved to be by far the best instrument for our aims, because the quasar-star alignment along the slit can be determined with sub-pixel precision. Short acquisition images ($5-10$ sec, usually in the V band) are used to take an image of the quasar at the center of the slit. As mentioned before, the slit is rotated, so that the nearby star is in the slit as well by the end of the acquisition process. A final exposure taken with the wide slit mask and without the grism is obtained in order to make sure both objects are properly centered. By default, the WFCCD slits are oriented North-South, so the rotation angles calculated according to equation 2.4 and listed in tables 2.1 and 2.2 are refereed to such direction. In 2005 and 2006 we used the WFCCD to perform spectroscopy for the whole sample to have a zero baseline of the signal-to-noise for each quasar, and to verify that the selected sources showed the required strong broad lines needed for reverberation mapping, and to check the performance of this instrument. Initial rotation angles were calculated in order to align the quasar and the comparison star in the slit, and have been confirmed or slightly corrected over the campaign. These corrections are typically introduced because the slit mask might not be perfectly aligned with the CCD.

- **Boller & Chivens spectrograph:**

  Also mounted on the 2.5m duPont Telescope, the B&C spectrograph has been used when the WFCCD is not available (not mounted on the telescope), usually during the CHASE observing time. The B&C slits masks are oriented East-West, thus the rotator angles calculated for the WFCCD are also used with this instrument by adding 90 degrees. The acquisition process in this case is by visual inspection of the acquisition camera rather than through imaging exposures. The FOV of the acquisition camera is squared and smaller than the slit length. Consequently the quasar can be positioned at the center of the slit, but the comparison star might not be seen. However, a short exposure spectrum can be obtained to make sure that both objects are within the wide slit. Severe fringing affects the region above $\sim 7\,600$Å given the wider spectral range and the bigger size of the pixels of the instrument. Even though the obtained spectra have not shown severe differences with those obtained with WFCCD, we try to avoid observing with this instrument because to

avoid systematic errors due to slit losses and also because the slit is shorter than the one of the WFCCD. Hence, there are some quasars that have comparison stars that cannot be simultaneously observed with this instrument, in which cases another star must be used (e.g. HB89[0329-385]).

- **Goodman spectrograph:**

  The Goodman spectrograph has been used once in the second half of 2009, when the duPont telescope was not available. Mounted on the SOAR 4.1m Telescope, it is similar to the WFCCD, although the rotator angles differ from those calculated for the duPont instruments, so they had to be calculated especially for this instrument on site during the observing run.

3

Broad Band Imaging

The first stage of the project consists in the monitoring of the continuum emission of the quasar sample which is done using broad band imaging. This allows us to detect variability and the onset of "events" which are followed up by a spectroscopic campaign.

The broad band *R* filter centered at 6410 Å and a width of $\Delta\lambda \sim 1470$ Å was chosen because it is broad enough (the broadest of the JKC family of optical filters) to incorporate a good estimate of the continuum flux and also, because most strong broad emission lines like Lyα, Si IV and C IV fall out of the filter transmission, mostly in the blue side below $\sim$ 5500Å (see figure 4.6). Hence our *R* band light curves mostly sample variations in continuum emission and show little contribution from line variability.

Given the high luminosity of the objects, they are bright enough that a small telescope is sufficient to properly monitor the continuum. Imaging data have been obtained with the 0.9m telescope at CTIO and the data reduction has been done using standard IRAF procedures. In addition, perl scripts (using perl's scientific library PDL) were written in order to manage and analyze the information given by the IRAF outputs.

In this chapter the data reduction and photometry measurements are described in detail.

3.1 Data Reduction

Imaging data reduction is done using standard IRAF[1] procedures. In particular we use scripts from the `SNPHOT` package written by Mario Hamuy for data reduction and relative photometry of supernova observations.

The first step in the reduction process is to fix the image header keywords. A quick view of the keywords that are going to be used by the scripts is done running the `chkhead` task. For the 0.9m telescope, the keyword *EPOCH* has to be set to the current year of the observation using the `hedit` task. Finally, an update of airmass and other keywords is done running the `headers` task.

Once the header keywords are correctly set we proceed to reduce the images using the `ccd40` task, which performs the bias subtraction and flat fielding correction of the images. As a summary, `ccd40` performs the following operations:

1. Combine bias frames to produce a Zero image for bias subtraction using the `zerocombine` task.
2. Combine dome flat frames to produce a Dome Flat image for flat fielding using the `flatcombine` task.
3. Process target images: overscan and bias subtraction using the Zero image, flat fielding using the Dome Flat image and trimming using the `ccdproc` task.

A final step is done by hand by adding the keywords *XSN* and *YSN* to each image header using `hedit`. These parameters correspond to the x and y pixel position of the quasar in each processed image obtained with the `imexam` task. Final images are stacked and saved in a database using the `spread` script. Imaging observing runs of the monitoring are listed in tables 3.1 and 3.2.

3.2 Photometric Measurements

An important difference between low and high redshift AGNs is that the former are seen as the nuclei of an extended source (host galaxy) while the latter is seen as a point source, because the host galaxy is too faint (compared with its active nucleus) to be detected, as illustrated in figures 3.1 and 3.2. Therefore, no galaxy subtraction is needed for high redshift quasars and then photometric procedures for point sources can be used. With the purpose of measuring the continuum variability of the quasar we perform differential photometry relative to a group of stars in each target field. Relative photometry allows flux variability measurements with a precision of $\lesssim 3\%$ regardless of weather conditions, because the quasar and its field stars are simultaneously observed under the same conditions. Therefore, only magnitude differences, and not absolute fluxes, are important.

For relative photometry there are 3 basic steps involved: **1.** to define a field star catalogue, **2.** to measure instrumental magnitudes, and **3.** to obtain differential light curves. In the following I describe the steps to obtain quasars light curves.

[1] IRAF (Image Reduction and Analysis Facility) is distributed by the National Optical Astronomy Observatories, which are operated by the Association of Universities for Research in Astronomy, Inc., under cooperative agreement with the National Science Foundation.

TABLE 3.1: IMAGING OBSERVING RUNS

Date	Julian Date (-2450000)
(1)	(2)
October 31, 2010	5500.5
October 06, 2010	5475.5
September 02, 2010.....	5441.5
August 05, 2010	5413.5
July 13, 2010.....	5390.5
May 27, 2010	5343.5
April 19, 2010.....	5305.5
March 18, 2010	5273.5
March 08, 2010	5263.5
February 07, 2010	5235.5
January 09, 2010	5205.5
December 12, 2009	5177.5
November 18, 2009	5153.5
October 5, 2009	5119.5
September 17, 2009.....	5091.5
August 20, 2009	5063.5
July 24, 2009.....	5036.5
June 27, 2009	5009.5
June 16, 2009	4998.5
April 22, 2009.....	4943.5
March 19, 2009	4909.5
February 26, 2009	4888.5
January 24, 2009	4855.5
November 29, 2008.....	4799.5
October 30, 2008	4769.5
October 20, 2008	4759.5
October 02, 2008	4741.5
August 26, 2008	4704.5
July 28, 2008.....	4675.5
July 10-16, 2008.....	4630.5
June 04, 2008	4621.5
May 29, 2008	4615.5
April 22-23, 2008.....	4578.5
February 08, 2008	4504.5
January 11, 2008	4476.5
December 04, 2007	4438.5
October 10, 2007	4383.5

TABLE 3.2: IMAGING OBSERVING RUNS (CONTINUATION)

Date	Julian Date (-2450000)
(1)	(2)
September 09, 2007.....	4352.5
August 09, 2007.....	4321.5
July 26, 2007.....	4307.5
July 12, 2007.....	4293.5
June 20, 2007	4271.5
June 06, 2007	4257.5
May 23, 2007	4243.5
May 18, 2007	4238.5
April 25, 2007.....	4215.5
March 26, 2007	4185.5
March 08, 2007	4167.5
February 22, 2007	4153.5
January 25, 2007	4125.5
January 16, 2007	4116.5
December 20, 2006	4089.5
November 08, 2006.....	4047.5
October 18, 2006	4026.5
September 24, 2006.....	4002.5
August 26, 2006.....	3973.5
August 01, 2006.....	3948.5
June 30, 2006	3916.5
June 07, 2006	3893.5
April 20, 2006.....	3845.5
March 23, 2006	3817.5
February 23, 2006	3789.5
February 14, 2006	3780.5
December 21, 2005	3725.5
November 17, 2005.....	3691.5
October 18, 2005	3661.5
September 19, 2005.....	3632.5
August 22, 2005.....	3604.5
July 30, 2005.....	3581.5
June 11, 2005	3532.5
May 24, 2005	3514.5
April 29, 2005.....	3489.5
March 14, 2005	3443.5
February 01, 2005	3402.5

3.2.1 Field Stars Catalogue

A group of 5-15 stars, depending on the number of suitable stars found in the field, were selected using the very first images obtained for each quasar with the 0.9m telescope in 2005. The criteria was basically to select bright stars with high S/N ratio (typically greater than 2 times the S/N of the quasar for a good determination of their magnitudes) which are located near the quasar (typically within $\lesssim 7$ arc min).

A catalogue of the field stars was made using the Aladin Sky Atlas and the USNO-B1 catalogue to obtain their position

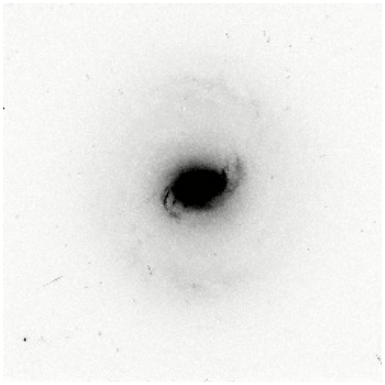

FIGURE 3.1: Galaxy Mk 579 cataloged as a Seyfert 2. With a redshift of $z = 0.017$ an extended host galaxy can be easily seen.

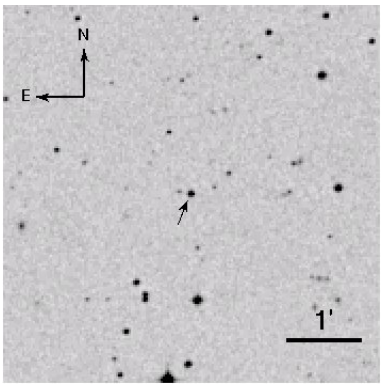

FIGURE 3.2: Quasar CTQ 286. With a redshift of $z = 2.8$ only a point source is seen.

in the sky (right ascension and declination) and a reference magnitude in the *R* filter. Owing to the difference between the USNO and the 0.9m telescope *R* filter, the reference USNO magnitudes were replaced by our very first instrumental measurements. However, we do not obtain the absolute photometry for them, so these reference magnitudes are never used.

3.2.2 Photometry

Photometry of point sources can be obtained using two approaches: *aperture* or *PSF* photometry. The former is based on the simple idea of calculating how many photons come from an aperture around the source, after subtracting the contribution from sky photons. The latter is a more sophisticated way of estimating fluxes and it is based on the idea of the Point Spread Function (PSF) of the image. In the following I briefly describe how to obtain fluxes and magnitudes by each method.

- **Aperture Photometry:** Let us assume that a point source spreads over an area called the *aperture* (generally set to a circle) equals to $n_{\rm ap}$ pixels in which fall N photons. The contribution of the sky within the aperture can be determinated from a circular anulus centered around the source composed of $n_{\rm sky}$ pixels in which the mean and standard deviation are $m_{\rm sky}$ and $\sigma_{\rm sky}$, respectively.

  Instrumental fluxes and magnitudes can be obtained using the equations

$$f = N - n_{\rm ap} \cdot m_{\rm sky} \tag{3.1}$$

$$\sigma_f^2 = \underbrace{N}_{(1)} + \underbrace{n_{\rm ap} \cdot \sigma_{\rm sky}^2}_{(2)} + \underbrace{\frac{n_{\rm ap}^2 \cdot \sigma_{\rm sky}^2}{n_{\rm sky}}}_{(3)} + \underbrace{\sigma_{\rm RN}^2}_{(4)} \tag{3.2}$$

  in which the final uncertainty σ_f is the quadratic sum of different error sources. Each error term can be identified as: **(1)** Poisson error, **(2)** error of the sky, **(3)** scatter of the sky noise in the aperture, and **(4)** read-out noise of the CCD.

Magnitudes and their uncertainties can be obtained from the previous equations through

$$m = \quad z_{\rm mag} - 2.5 \log\left(\frac{f}{\rm exptime}\right) \tag{3.3}$$

$$\sigma_m = \quad 1.0857 \frac{\sigma_f}{f} \tag{3.4}$$

where *exptime* is the exposure time and $z_{\rm mag}$ is the zero point constant for instrumental magnitudes which is set arbitrarily to $z_{\rm mag} = 25$.

- **PSF Photometry:** Photons from a point source do not fall on the same pixel in the CCD. In fact, point sources can be modeled by a bi-dimensional brightness distribution in the detector, mainly due the instrumental response of the instrument and seeing conditions. This 2D brightness distribution is called the *point spread function* (PSF). The PSF is nearly the same for every point source in the detector, and then fluxes can be obtained from this profile.

  PSF profiles can be found by two approaches: the analytical or the empirical one. **1.** The analytical approach consists basically in fitting a mathematical model to the brightness distribution. This function is usually assumed to be a gaussian, but it can be modeled by a Moffat function as well. **2.** The empirical approach performs a bivariate interpolation of the observed brightness distribution using cubic splines. The detailed process of the fitting of the PSF profile is out of the scope of this thesis.

  IRAF performs PSF photometry using a package called `DAOPHOT` (Stetson, 1987). The fitting process is done using a mixed approach, first fitting an analytic function and then interpolating to give a better fit to the real shape of the PSF for each image from which fluxes want to be obtained. The associated uncertainty for each pixel is given by the equation

$$\sigma^2_{\rm PSF} = \underbrace{I}_{(1)} + \underbrace{\left(0.01\,\sigma_{\rm prof}\,\frac{I - {\rm sky}}{\sigma^2_x \sigma^2_y}\right)^2}_{(2)} + \underbrace{\left(0.01\,\sigma_{\rm flat} \cdot I\right)^2}_{(3)} + \underbrace{\sigma^2_{\rm RN}}_{(4)} \tag{3.5}$$

  where I is the intensity of each pixel, $\sigma_{\rm flat}$ and $\sigma_{\rm prof}$ are estimates of the flat fielding and profile uncertainties and σ_x and σ_y are the standard deviation of the bi-dimensional fitting function. Each term in (3.5) can be interpreted as: **(1)** Poisson error of the source, **(2)** uncertainty associated to the fitting process, **(3)** quantitative estimate of the flat fielding error and **(4)** read-out noise of the CCD.

Each term in the uncertainty for aperture photometry (eq. 3.2) has its analogue in the PSF photometry (eq. 3.5). Terms **(1)** are associated with the Poisson statistics of the photons. The second terms **(2)** are associated with the sky level subtraction, **(3)** are associated with the scatter of the signal over the aperture, and **(4)** are the noise introduced by the read-out of the CCD.

We have decided to perform PSF photometry because it automatically gives instrumental magnitudes associated with the PSF of each image, and therefore is an efficient way to obtain photometry for a large amount of data. On the contrary, aperture photometry would be very inefficient because for each image, an optimal aperture has to be found, slowing the data processing. In addition, some fields are evidently more crowded than others, making the PSF photometry the natural way to perform photometric measurements in our monitoring.

Photometric measurements were obtained using the `sne` task in the `SNPHOT` package. This script performs PSF photometry not only to the central quasar but for the field star catalogue too. In order to do so, the task selects field stars using `daofind` to derive a geometric transformation identifying the stars of the catalogue using a reference point in the field (given by XSN and YSN, the quasar position). This geometric transformation needs to be done only once if the scale of the images does not change over the monitoring campaign. Then, preliminary aperture photometry of the catalogue stars is performed in order to obtain a rough estimation of their magnitudes. A PSF is fitted to the best stars (highest signal-to-noise) in the catalogue using the mixed approach mentioned before, and then an instrumental magnitude is derived for the selected stars using the `allstar` task in `DAOPHOT`.

An analysis of the photometric uncertainties of the objects with large error bars in some epochs has shown that the dominant term in the error equation is the one associated with the Poisson photon statistics. Thus, large uncertainties are associated with poor weather conditions. A minimum uncertainty of 0.015 mag is assumed to account for the unknown error sources that might affect our data.

The mean magnitude of the field stars for each quasar in our sample show an intrinsic scatter of $\sigma \sim 0.03$ mag which represent an uncertainty of $\sim 3\%$ in flux, in agreement with the expected accuracy of this method (see §5.3).

3.2.3 Diferential Light Curves (DLCs)

Once the instrumental magnitudes are obtained using IRAF, data are analyzed using a perl program called `qsoproc.pl`. This program reads the output files from IRAF to get the julian day, instrumental magnitudes and uncertainties of the quasar and each field star for every observed epoch to obtain the differential light curve (hereafter DLC) of the quasar.

Since the main aim is to measure the quasar variability, we compare its magnitude with the combined magnitude of the stars in the catalogue. However, these stars might not have constant flux with time, so we need to constrain the stars used to make the quasar DLC.

3.2.3.1 Field Stars Analysis

Field stars magnitudes will not be the same from one observing run to another because of changes in weather conditions between different epochs. However, this variability will affect every source, since they are all observed under the same conditions, and then, the relative magnitudes between field stars will remain constant for different epochs.

Hence, field star magnitudes are used as a relatively constant (within the photometric errors) for comparison against the quasars magnitude. Therefore, it is important to make sure that these stars are not intrinsically variable. If a field star does not appear in the field in every observed epochs, it is automatically discarded.

Intrinsic variability test: In the other hand, we need to discard intrinsic variable stars, because it would introduce variability on the quasars DLC which would not be due the quasar itself. Once each field star has a complete set of magnitudes for all observations, individual stars are checked in order to select non variable sources. Variability of each field star is tested against the mean of the remaining field stars.

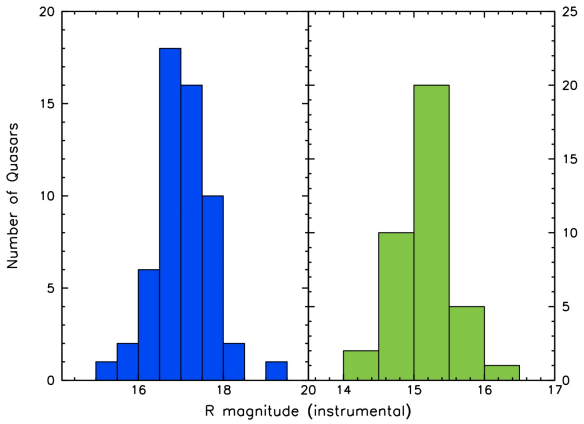

FIGURE 3.3: Histogram with the instrumental magnitudes for the quasar sample (left) and for the mean magnitude of the comparison field stars of each quasar (right).

Again, for M observations for a particular quasar with N field stars, we define for the k star

$$\Delta m_k(t_j) = m_k(t_j) - \frac{1}{s_k^2}\sum_{i\neq k}^{N}\frac{m_i(t_j)}{\sigma_i^2}, \quad j = 1,\ldots,M \tag{3.6}$$

where $s_k^2 = \sum_{i\neq k} 1/\sigma_i^2$. The time serie $\Delta m_k(t)$, $t = t_1 \ldots t_M$ defines its DLC.

This differential light curve is then scaled to have a mean of 0, and then the amplitude and RMS are measured. We expect that a *non variable* (within the photometric errors) star has a maximum amplitude variability[2] of $A_{max} = 5\%$ in flux, which translates into $\Delta m_k \leq 0.05$. In addition a constrain in the root-mean-square (RMS) is given by RMS ≤ 0.005.

Finally, the weighted mean of field stars for each field is calculated according to

$$\langle m\rangle_\star = \frac{1}{s^2}\sum_{i=1}^{N} w_i \frac{m_i}{\sigma_i^2} \tag{3.7}$$

where $w_i = 0$ if star i is discarded and $w_i = 1$ if the star is selected according to the requirements mentioned above.

On average, quasar magnitudes are ~ 2 magnitudes fainter than their field stars as shown in the histogram in figure 3.3.

3.2.3.2 Quasar and Mean Field Stars DLCs

During the photometric monitoring we define two light curves for each quasar: one for the field stars mean (DLC$_\star(t)$) and other for the quasar itself (QDLC(t)). The former to check the the non variable field stars mean and the latter to quantify the variability of the quasar.

1. **Field Star DLC**

   Once we have N non variable stars selected, we proceed to evaluate their weighted mean. For a particular epoch

[2] See chapter 5

this is calculated according to

$$\langle m\rangle_\star = \frac{1}{s^2}\sum_i \frac{m_i}{\sigma_i^2} \tag{3.8}$$

where the weight is the inverse of the square error for each star, and s^2 is defined as

$$s^2 = \sum_i \frac{1}{\sigma_i^2}$$

The associated uncertainty of the mean is calculated as

$$\sigma^2_{\langle m\rangle_\star} = \frac{1}{s^4}\sum_i \left(\frac{\partial\langle m\rangle_\star}{\partial m_i}\right)^2 \sigma_i^2 \tag{3.9}$$

$$\frac{\partial\langle m\rangle_\star}{\partial m_i} = \frac{1}{\sigma_i^2} \tag{3.10}$$

and then

$$\sigma^2_{\langle m\rangle_\star} = \sum_i \frac{1}{\sigma_i^4\, s^4}\sigma_i^2 = \frac{1}{s^4}\sum_i \frac{1}{\sigma_i^2} = \frac{s^2}{s^4} = \frac{1}{s^2} \tag{3.11}$$

$$\sigma^2_{\langle m\rangle_\star} = \frac{1}{\sum_i 1/\sigma_i^2} \tag{3.12}$$

If all field stars had the same error $\sigma_i = \sigma$ then we would have

$$\sigma^2_{\langle m\rangle_\star} = \frac{1}{\sum_i 1/\sigma^2} = \frac{\sigma^2}{N} \tag{3.13}$$

which is the same result if we were used the unweighted mean for the field stars.

The time serie of $\langle m\rangle_\star$ is scaled to have zero mean which defines the Differential Light Curve (DLC) of the field star mean.

$$\mathbf{DLC}_\star(t_i) \;=\; \langle m\rangle_\star(t_i) \;-\; \underbrace{\frac{1}{M}\sum_{j=1}^{M}\langle m\rangle_\star(t_j)}_{\text{constant}} \tag{3.14}$$

2. **Quasar's DLC**

For a particular epoch we define

$$x = m_{\mathrm{QSO}} - \langle m\rangle_\star \tag{3.15}$$

where m_{QSO} is the instrumental magnitude of the quasar. The Quasar Differential Light Curve (QDLC) is defined as the scaled time series of x with zero mean according to

$$\mathbf{QDLC}(t_j) \;=\; x(t_j) \;-\; \underbrace{\frac{1}{M}\sum_{j=1}^{M} x(t_j)}_{\text{constant}} \tag{3.16}$$

QDLC uncertainty is obtained as the quadratic sum of each uncertainty term in (3.16)

$$\sigma^2_{\mathrm{QDLC}} = \sigma^2_{\mathrm{QSO}} + \sigma^2_{\langle m\rangle_\star} \tag{3.17}$$

In the particular case that $\sigma_i = \bar{\sigma}$ for every i star selected in the catalogue we get

$$\sigma^2_{\mathrm{QDLC}} = \sigma^2_{\mathrm{QSO}} + \frac{\bar{\sigma}^2}{N} \tag{3.18}$$

3.2.3.3 Continuum Relative Flux

Using the transformation between a magnitude m and its flux f given by

$$m = -2.5 \log f + \text{constant} \tag{3.19}$$

we have that for a particular run the mean field stars magnitude can be written as

$$\langle m \rangle_\star = \frac{1}{s^2} \sum_i \frac{m_i}{\sigma_i^2} = -\frac{2.5}{s^2} \sum_i \frac{1}{\sigma_i^2} \log f_i \tag{3.20}$$

using the properties of the logarithm we get

$$\langle m \rangle_\star \; = \; -2.5 \, \frac{1}{s^2} \log \Pi_i \, f_i^{1/\sigma_i^2} \tag{3.21}$$

and finally we identify

$$\langle m \rangle_\star \; = \; -2.5 \log \underbrace{\left(\Pi_i \, f_i^{1/\sigma_i^2} \right)^{1/\sum_i 1/\sigma_i^2}}_{\begin{array}{c}\text{weighted}\\ \text{geometrical}\\ \text{mean}\end{array}} \tag{3.22}$$

Therefore, if we call

$$\langle f \rangle_\star = \left(\Pi_i \, f_i^{1/\sigma_i^2} \right)^{1/\sum_i 1/\sigma_i^2} \tag{3.23}$$

we have that

$$m_{\mathrm{QSO}} - \langle m \rangle_\star = -2.5 \log \left(\frac{f_{\mathrm{QSO}}}{\langle f \rangle_\star} \right) \tag{3.24}$$

We define the relative flux of the continuum as

$$\text{Rel. Flux}_{\mathrm{cont}} = \frac{f_{\mathrm{QSO}}}{\langle f \rangle_\star} = 10^{-0.4 \left(m_{\mathrm{QSO}} - \langle m \rangle_\star \right)} \tag{3.25}$$

4

Spectroscopy

The second part of the monitoring campaign consists of a spectroscopic follow up of the most variable quasars in the sample to measure the variability of the BLR emission lines.

Spectra were obtained with the 2.5m telescope at LCO (Las Campanas Observatory) and 4.1m SOAR telescope and the reduction and extraction were done using standard IRAF procedures. Flux calibrated spectra for 14 of the 15 spectroscopically monitored quasars are presently available.

4.1 Data Reduction

Bias and flat fields combination was done using `zerocombine` and `flatcombine`, respectively. Bias and overscan subtraction and flat fielding were done using the `ccdproc` task. A mask was also used to fix bad columns in images taken with the WFCCD instrument.

Spectra were extracted using the `apall` task in *multispec* mode allowing the extraction of several objects simultaneously. The trace of both spectra are well fitted by a 3rd order Legendre polynomial. Windows of 60 pixels on each side were used to estimate the background sky level. Large background windows of $\sim 100-200$ pixels on each side were used in observations under poor weather conditions for a good estimate of the sky counts level.

Wavelength calibration is performed using the `identify` and `reidentify` tasks with a 7th order Chebyshev polynomial fit. Wavelength solution is achieved when the residuals are lower than $15\,\mathrm{km\,s^{-1}}$ in velocity scale, which is roughly the resolution of the narrow slit ($150\,\mu$m). The final dispersion coordinates of the spectra correspond to a linear

function with a step of $\Delta\lambda = 1$ Å starting from 4000 Å to 9000 Å.

Spectroscopic observing runs are listed in table 4.1. Dates and the instruments used are shown (see chapter 2). Columns from (1) to (6) are self explanatory. Column (7) correspond to the observed spectrophotometric standards.

TABLE 4.1: SPECTROSCOPIC OBSERVING RUNS

Date	Julian Date (-2450000)	Telescope	Instrument	Slit (μm)	Exposure Time (sec)	Spectrophotometric Standard
(1)	(2)	(3)	(4)	(5)	(6)	(7)
October 29-30, 2010	5500.5	2.5m, LCO	B&C	450, 150	900×3	LTT7987, LTT9239
October 05, 2010	5474.5	2.5m, LCO	WFCCD	750, 150	900×3	LTT7379, LTT7987
September 29, 2010	5468.5	2.5m, LCO	WFCCD	750, 150	900×3	LTT7379, LTT7987
September 13, 2010	5452.5	2.5m, LCO	WFCCD	750, 150	900×3	LTT7379, LTT9239
July 11, 2010	5388.5	2.5m, LCO	WFCCD	750, 150	900×3	CD 32
July 07, 2010	5384.5	2.5m, LCO	WFCCD	750, 150	900×3	CD 32
May 19, 2010	5335.5	2.5m, LCO	B&C	450, 150	900×3	LTT7379, LTT7987
March 24, 2010	5279.5	2.5m, LCO	WFCCD	750, 150	900×3	LTT3864, LTT6248
March 14, 2010	5269.5	2.5m, LCO	WFCCD	750, 150	900×3	–
December 6-7, 2009	5171.5	2.5m, LCO	WFCCD	750, 150	900×3	LTT3864
September 11, 2009	5085.5	4.1m, SOAR	Goodman	1000, 103	???×3	–
May 30, 2009	4981.5	2.5m, LCO	B&C	450, 150	900×3	–
March 26, 2009	4916.5	2.5m, LCO	WFCCD	750, 150	900×3	–
February 24, 2009	4886.5	2.5m, LCO	WFCCD	750, 150	900×3	–
February 22, 2009	4884.5	2.5m, LCO	WFCCD	750, 150	900×3	–
December 19-23, 2008 ...	4822.5	2.5m, LCO	WFCCD	750, 150	900×3	LTT4364, LTT3218
October 27, 2008	4766.5	2.5m, LCO	WFCCD	750, 150	900×3	–
October 19, 2008	4758.5	2.5m, LCO	WFCCD	750, 150	900×3	LTT377, LTT9491
September 28, 2008	4737.5	2.5m, LCO	WFCCD	750, 150	900×3	–
September 20-21, 2008 ...	4729.5	2.5m, LCO	WFCCD	750, 150	900×3	LTT7379, LTT9491
May 10-11, 2008	4596.5	2.5m, LCO	WFCCD	750, 150	900×3	–
May 04, 2008	4590.5	2.5m, LCO	WFCCD	750, 150	900×3	–
April 28, 2008	4584.5	2.5m, LCO	WFCCD	750, 150	900×3	–
March 30, 2008	4555.5	2.5m, LCO	WFCCD	750, 150	900×3	–
December 8-9, 2007	4442.5	2.5m, LCO	WFCCD	750, 150	900×3	LTT1788, LTT2415
September 11, 2007	4354.5	2.5m, LCO	B&C	450, 150	900×3	LTT7379, EG274
May 10, 2007	4230.5	2.5m, LCO	B&C	450, 150	900×3	LTT2415
April 11, 2007	4201.5	2.5m, LCO	WFCCD	750, 150	900×3	LTT4364, LTT6248

4.2 Normalized Spectra

Spectroscopic monitoring has been carried out during several years under different weather conditions. This means that the spectra taken over the campaign are of different quality. In order to have a good measure of the variability of each observable emission line we performed differential spectroscopy relative to a nearby bright star.

The idea behind relative spectroscopy is that the comparison star is used to normalize the quasar spectrum, and then all the measurements can be done reliably. To do such normalization, the star spectrum is heavily smoothed so that

absorption features (intrinsic and telluric) and noise disappear. The smooth curve is then used to normalize the quasar spectrum from which emission line fluxes and line widths are measured. The normalization of the quasar is performed by IRAF scripts made by Shai Kaspi and modified for our purposes by Paulina Lira. For a particular set of spectra for an object obtained in a particular epoch, the procedure consist of the next steps:

1. A first inspection is done to check the wavelength dispersion and quality of the spectrum. In this step, the quasar is divided by its comparison star for each observed spectra. The resulting normalized spectrum is then divided between each other giving a ratio which should be nearly constant in flux centered in 1. Systematic errors are estimated by taking the mean of this ratio spectrum and recording it by hand in a log file to have an estimation of the quality of the spectra.

2. Spectra are averaged to improve the signal-to-noise spectra of both the quasar and the nearby star.

3. The combined spectrum of the comparison star is heavily smoothed with a boxcar[1] of 501 Å, twice. This gives a very smooth curve. Figures 4.1 and 4.2 show the spectrum of the comparison star of CTQ 953 before and after the smoothing respectively as example of this step.

4. The combined quasar spectrum is divided by the smoothed star, giving a nearly flat spectrum, from which the emission lines fluxes and widths are measured. Normalized spectra can be found in appendix B.

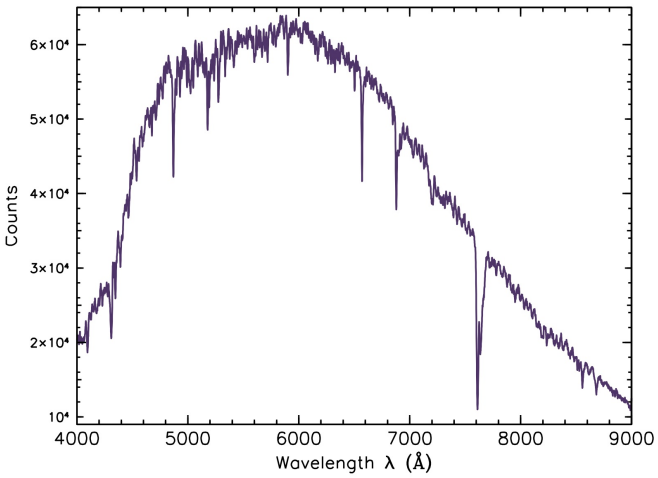

FIGURE 4.1: CTQ 953 comparison star optical spectrum. Noise and absorption lines (Balmer an telluric) can be seen.

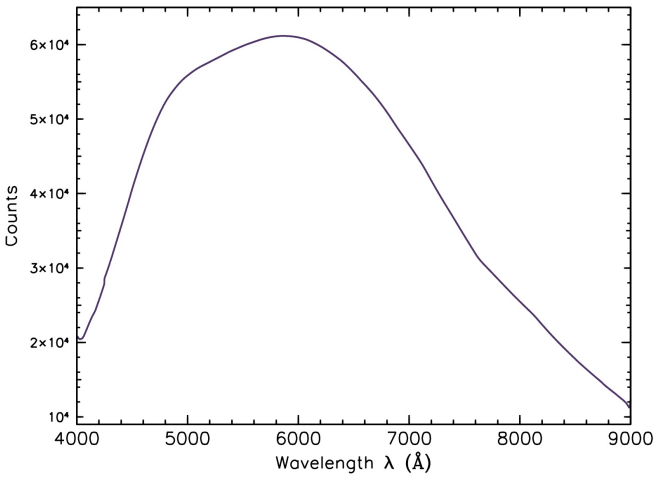

FIGURE 4.2: CTQ 953 comparison star optical spectrum after boxcar filtering. The resultant spectrum is smooth and featureless.

As already explained in chapter 2, in order to observe both targets, the quasar and the comparison star simultaneously, the slit has to be oriented in a particular fixed direction on the sky which is different from the parallactic angle at the time of the observation. This might introduce problems because there would be light losses due the atmospheric refraction. To minimize this effect we have used a wide slit. In addition, observations are performed at low airmass ($X \lesssim 1.4$) were the atmospheric refraction is not dominant.

[1] boxcar smoothing function is defined using odd numbers

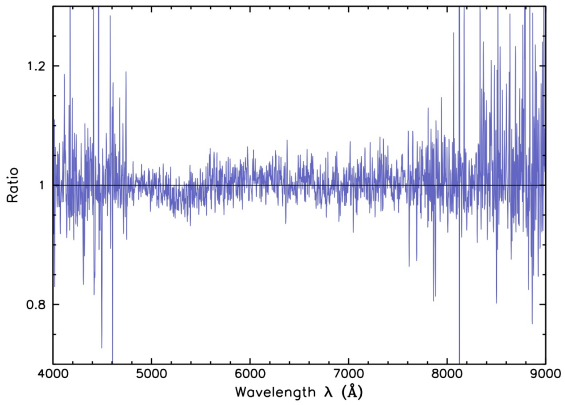

FIGURE 4.3: Ratio between CTQ CT320 spectra obtained in two consecutive nights (December 20th and 21st, 2008).

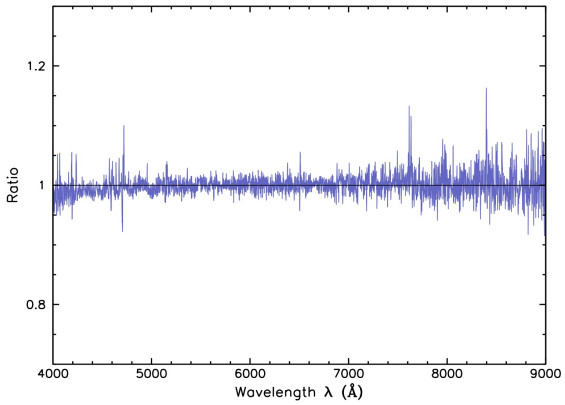

FIGURE 4.4: Ratio between CTQ 953 spectra obtained in two observations four days apart (July 7th and July 11th, 2010).

However, it is important to quantify this effect in order to incorporate it in the final measurement of the flux. An attempt of that was done using observations of a couple of targets (CTQ 953 and CTQ 320) in two different but close epochs. It is important to note that these two epochs had different weather conditions, and the observations were made at different times, so the parallactic angle of one observation is different from the other and then both spectra have different angles respect to its parallactic value. The typical variability time scale for high redshift quasars are much longer than a few weeks and therefore there should not be any significant difference between both normalized spectra.

Weather conditions for both ratios are completely different: CTQ 953 was observed under optimal weather conditions, while CTQ 320 was observed in cloudy nights. The ratio between spectra from different epochs for each object are shown in figures 4.3 and 4.4. A simple statistics of the ratios between 5 000Å and 7 500Å (where the emission lines are measured) show a mean value of 1.001 for CTQ 953 and 1.06 for CTQ 320 with a root-mean-square of 0.0273 and 0.0585 respectively. This is in perfect agreement with Kaspi et al. (2000) who argues that these difference are of order of $\lesssim 2\%$. However, poor weather introduce noise which has to be taken into account when estimating the continuum level and measuring emission lune fluxes. We will come back to this in the next section.

4.3 Emission Lines Fluxes

Once the quasar spectrum is normalized the emission line fluxes and widths can be measured. For the flux measurements we use a method developed by Shai Kaspi[2] which consists in a simple linear interpolation of the continuum flux level under the emission line. The procedure for continuum subtraction and the flux measurement is as follows:

Continuum Fitting: For each broad emission line in the spectrum, three wavelength windows are defined as shown in figure 4.5: one which correspond to the emission line itself, and two windows on each side from which the continuum will be estimated. Hereafter, I will refer to the continuum windows located at a lower and higher wavelength of the emission line window as the *blue* and *red* side respectively. Each window is centered at

[2]Private communication.

wavelengths $\lambda_{\rm B}$, $\lambda_{\rm R}$ and $\lambda_{\rm line}$ where the subscripts "B" and "R" stands for the blue and red side respectively. As an example from real data, windows defined according the scheme of figure 4.5 are shown in the normalized spectrum of CTQ 953 in figure 4.6. Continuum blue and red windows are marked above the normalized spectrum whereas emission line windows for Si IV , C IV and C III] emission lines are shown below the spectrum. Continuum window widths are small in order to avoid absorption lines near the emission lines.

From the previous combination of spectra of each observing run, there is an error source that must be taken into account related to how noisy are the combined spectra. As mentioned before, not all observations are of the same quality. This is incorporated in the measure of the flux uncertainty using the log described in the first step of the normalization process. The "noise" uncertainty due the quality of the observations is quantified by

$$\sigma^2_{\rm noise} = \frac{1}{N}|1-q| \tag{4.1}$$

where N is the number of spectra obtained and q is the quality of the observation which correspond to the mean measured in the normalization process. If the spectra are of high enough quality, the systematic error is $\sigma^2_{\rm noise} \sim 0$. In the opposite case of observations under poor weather conditions, q could differ strongly from 1, and then $\sigma^2_{\rm noise}$ is significant.

Statistics are computed in the final normalized spectra using the IRAF task `imstat` which gives the mean fluxes per unit wavelength and the root-mean-square of each window obtaining the values $f_\lambda \pm \delta f_\lambda$ at the central window wavelength $\lambda_{\rm window}$. The uncertainty of single fluxes are the quadratic sum of the measured root-mean-square determinated for each continuum window and the systematic error:

$$\sigma^2_B = \delta f^2_B + (\sigma_{\rm noise} \cdot f_B)^2 \tag{4.2}$$

$$\sigma^2_R = \delta f^2_R + (\sigma_{\rm noise} \cdot f_R)^2 \tag{4.3}$$

We can construct a continuum spectrum by a simple linear interpolation between the blue and red continuum windows. The continuum as a function of wavelength is given by

$$f_{\rm cont}(\lambda) = \left(\frac{f_R - f_B}{\lambda_R - \lambda_B}\right)(\lambda - \lambda_B) + f_B \tag{4.4}$$

where the error is given by the propagation equation

$$\sigma^2_{f_\lambda} = \left(\frac{\partial f_\lambda}{\partial f_B}\right)^2 \sigma^2_B + \left(\frac{\partial f_\lambda}{\partial f_R}\right)^2 \sigma^2_R \tag{4.5}$$

We will define the error coefficients e_i as

$$\frac{\partial f_\lambda}{\partial f_B} \equiv e_B = \left(\frac{\lambda - \lambda_B}{\lambda_B - \lambda_R}\right) + 1 = \left(\frac{\lambda - \lambda_R}{\lambda_B - \lambda_R}\right) \tag{4.6}$$

$$\frac{\partial f_\lambda}{\partial f_R} \equiv e_R = \left(\frac{\lambda - \lambda_B}{\lambda_B - \lambda_R}\right) \tag{4.7}$$

The continuum fit and its error is given by

$$f_{\rm cont}(\lambda) = \left(\frac{f_R - f_B}{\lambda_R - \lambda_B}\right)(\lambda - \lambda_B) + f_B, \qquad \sigma^2_{f_\lambda} = e^2_B \sigma^2_B + e^2_R \sigma^2_R \tag{4.8}$$

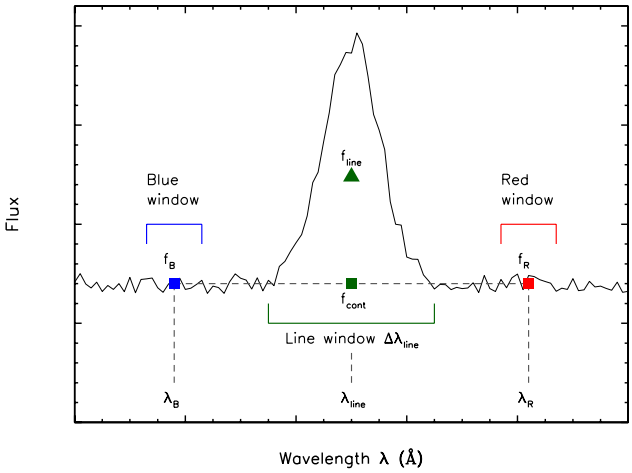

FIGURE 4.5: Scheme for the continuum fitting.

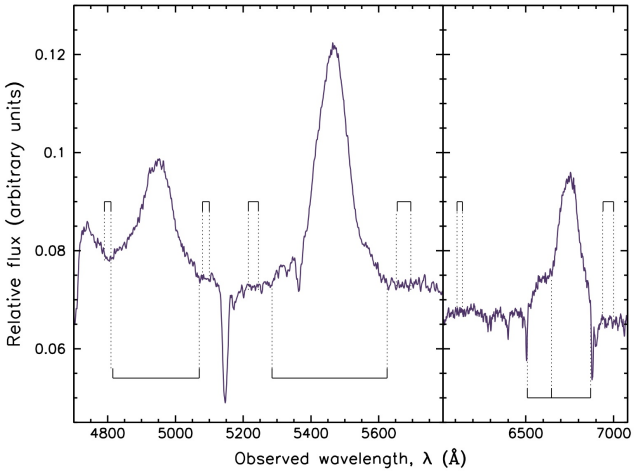

FIGURE 4.6: Normalized spectrum of CTQ 953. Blue and red continuum windows for each emission line are shown above the spectrum, while the emission lines windows are shown below for Si IV λ1400 + O IV] λ1402, C IV λ1549 and Si III] λ1892 + C III] λ1909respectively.

Emission line Flux: The continuum fit is then subtracted from the emission line and then multiplied by the line width to measure the flux inside the window. We now define the relative line flux $F_{\rm line}$ according to the equation

$$F_{\rm line} = [f_{\rm line} - f_{\rm cont}(\lambda_{\rm line})]\,\Delta\lambda_{\rm line} \tag{4.9}$$

where $\Delta\lambda_{\rm line}$ is the width of the emission line window in Å.

The uncertainty $\sigma_{F_{\rm line}}$ associated with the measured flux is given by

$$\sigma^2_{F_{\rm line}} = \Delta\lambda^2_{\rm line}\left[\sum_{i=B,R} e_i^2\cdot\delta f_i^2 \;+\; \sigma^2_{\rm sys}\cdot\left((f_{\rm line}-f_{\rm cont})^2_{\lambda_{\rm line}} + \sum_{i=B,R} e_i^2\, f_i^2\right)\right] \tag{4.10}$$

or simply

$$\sigma^2_{F_{\rm line}} = \Delta\lambda^2_{\rm line}\left[\sigma^2_{\rm noise}\cdot(f_{\rm line}-f_{\rm cont})^2_{\lambda_{\rm line}} \;+\; \sum_{i=B,R} e_i^2\cdot\sigma_i^2\right] \tag{4.11}$$

Therefore, $F_{\rm line}$ is an adimensional flux measure of the emission line relative to the smoothed star spectrum. Wavelength windows are summarized in table 4.3 for each object an each emission line available in the spectra.

4.4 Emission Lines Widths

We will follow the Peterson et al. (2004) procedure for the measurements of the emission line widths. The line width of a line profile $P(\lambda)$ can be estimated using the *FWHM* of the line. The Full Width at Half Maximum can be measured depending on whether the line is single or doubled peaked. In our spectroscopic sample, all the lines are single peaked, so we do not deal with more complex profiles.

For each line, the peak emission is identified as $P(\lambda)_{\max}$ at $\lambda_{\max}$. If we start from the shortest wavelength of the line window (short wavelength limit in column 8 in table 4.3) toward longer wavelengths, we will find a λ_1 that satisfies $P(\lambda_1) = \frac{1}{2}P(\lambda)_{\max}$. If we start to look from $\lambda_{\max}$ to shorter wavelengths, we will find a λ_2 that also satisfies $P(\lambda_1) = \frac{1}{2}P(\lambda)_{\max}$. If the emission line had a symmetric profile $P(\lambda)$, then $\lambda_1 = \lambda_2$. For real lines, however, $\lambda_1 \neq \lambda_2$ in general. The mean of these two wavelengths is said to be the shortest limit λ_1^{FWHM} of the FWHM. The procedure is the same for the longer wavelength side that will give a λ_2^{FWHM}.

The difference between the wavelengths found by this method is said to be the FWHM according to the equation

$$\mathbf{FWHM} = \lambda_2^{FWHM} - \lambda_1^{FWHM} \tag{4.12}$$

The doppler velocity can be inferred from the FWHM using the relation

$$\mathrm{v}_{\mathrm{FWHM}} = \frac{c \cdot \mathbf{FWHM}}{\lambda_{\mathrm{line}}} \tag{4.13}$$

There is another way to estimate the width of an emission line which is using the first and second moment of the line profile which yield the centroid wavelength λ_0 and the dispersion σ_{line} of the emission line respectively. Quantitatively we have

$$\lambda_0 = \frac{\int \lambda P(\lambda)\, d\lambda}{\int P(\lambda)\, d\lambda} \tag{4.14}$$

$$\sigma_{\mathrm{line}}^2 = \frac{\int \lambda^2 P(\lambda)\, d\lambda}{\int P(\lambda)\, d\lambda} - \lambda_0^2 \tag{4.15}$$

and the doppler velocity inferred from the line dispersion is found to be

$$\mathrm{v}_{\mathrm{line}} = \frac{c \cdot \sigma_{\mathrm{line}}}{\lambda_0} \tag{4.16}$$

The definition of σ_{line} is very useful because it is well defined for arbitrary line profiles. Besides, Peterson et al. (2004) found that using σ_{line} the relative uncertainties for the virial mass of black holes in AGN at low redshift (equation (1.4)) are smaller when compared with virial masses using the FWHM as the line width measurement. The FWHM and σ_{line} widths are related by a simple relation when the line profile is gaussian, in which case we have $\mathbf{FWHM}/\sigma_{\mathrm{line}} = 2\sqrt{2\ln 2} \approx 2.355$. A smaller ratio between these two quantities indicates that the line wings are important. The FWHM and σ_{line} widths are listed in table 4.3.

The uncertainty of the line width for both methods can be estimated from the resolution of the slit, namely $\Delta\lambda_{\mathrm{slit}}$. Then, in velocity units the uncertainty is given by

$$\sigma_{\mathrm{V}} = \frac{c \cdot \Delta\lambda_{\mathrm{slit}}}{\lambda_0} \tag{4.17}$$

TABLE 4.2: FLUX, LUMINOSITY AND COSMOLOGICAL MEASUREMENTS FROM THE SPECTROSCOPIC SAMPLE

Redshift has been calculated from the C IV $\lambda 1549$ in the spectra. CTQ 564 does not have a calibration yet.

Object	Redshift	D_L	Look Back Time	$F_\lambda(1350\,\text{Å})$	$\lambda L_\lambda(1350\,\text{Å})$
	z	(10^3 Mpc)	(Gyrs)	(10^{-16} erg cm^{-2} s^{-1} Å^{-1})	(10^{46} erg s^{-1})
(1)	(2)	(3)	(4)	(5)	(6)
CTQ 286	2.56	21.60	11.22	1.15 ± 0.02	3.09 ± 0.05
CTQ 320	2.95	25.73	11.60	1.29 ± 0.02	5.46 ± 0.10
CTQ 367	2.61	22.10	11.27	2.64 ± 0.05	7.53 ± 0.14
CTQ 406	3.18	28.15	11.78	1.24 ± 0.03	6.66 ± 0.15
CTQ 564	2.65	22.59	11.32	–	–
CTQ 650	2.67	22.70	11.33	5.05 ± 0.13	15.40 ± 0.40
CTQ 803	2.76	23.70	11.15	3.13 ± 0.12	10.71 ± 0.40
CTQ 953	2.53	21.25	10.92	5.97 ± 0.12	15.37 ± 0.30
CTQ 975	2.85	24.65	11.51	1.59 ± 0.09	6.00 ± 0.36
CTQ 1061	3.38	30.27	11.92	1.24 ± 0.04	9.23 ± 0.32
HB89 [0329-385]	2.43	20.30	11.08	3.46 ± 0.08	7.92 ± 0.17
J 002830	2.41	20.11	11.06	2.75 ± 0.07	6.14 ± 0.16
J 214355	2.62	22.25	11.29	2.62 ± 0.06	7.60 ± 0.17
J 221516	2.71	23.14	11.38	4.53 ± 0.02	14.52 ± 0.08
J 224743	2.59	21.90	11.25	3.32 ± 0.10	9.23 ± 0.28

4.5 Calibrated spectra

A couple of spectrophotometric standards were observed each run in order to calibrate in flux the spectra of each object. The flux calibration of the whole spectroscopic sample were done using the tasks `standard`, `sensfunc` and `calibrate` in IRAF.

For each object, I have selected the calibrated spectrum with the highest signal to noise ratio in order to measure the luminosity of the UV continuum, whose results are shown in table 4.2. Bolometric luminosity can be estimated from the observed UV luminosity using a transformation given by Marconi et al. (2004) which will be explained in section §6.4.

TABLE 4.3: WAVELENGTH WINDOWS AND EMISSION LINES WIDTHS
The wavelengths are in the observer's reference frame.

Object	Emission Line	Blue window (Å)	Red window (Å)	Line window (Å)	**FWHM** ($km s^{-1}$)	σ_{line} ($km s^{-1}$)
(1)	(2)	(3)	(4)	(5)	(6)	(7)
CTQ 286	C IV	5230 – 5280	6130 – 6180	5355 – 5745	4436 ± 120	3132 ± 120
	C III]	6100 – 6160	7225 – 7275	6520 – 6880	4385 ± 120	3096 ± 120
CTQ 320	Si IV	5370 – 5405	5715 – 5765	5420 – 5680	3660 ± 120	2427 ± 120
	C IV	5910 – 5950	6750 – 6830	5980 – 6355	7459 ± 120	3279 ± 120
	C III]	7090 – 7150	8010 – 8050	7220 – 7790	4257 ± 120	1723 ± 120
CTQ 367	Si IV	5370 – 5405	5715 – 5765	5420 – 5680	4540 ± 120	2319 ± 120
	C IV	5910 – 5950	6750 – 6830	5980 – 6355	4760 ± 120	3075 ± 120
	C III]	7090 – 7150	8010 – 8050	7220 – 7790	7656 ± 120	3993 ± 120
CTQ 406	Si IV	5640 – 5685	6040 – 6075	5695 – 6010	2946 ± 120	1267 ± 120
	C IV	6115 – 6160	7140 – 7200	6240 – 6760	4657 ± 120	3197 ± 120
CTQ 564	Si IV	4785 – 4835	5310 – 5345	5010 – 5295	4535 ± 120	2865 ± 120
	C IV	5375 – 5420	6215 – 6270	5530 – 5870	5711 ± 120	3336 ± 120
	C III]	6350 – 6420	7225 – 7300	6620 – 7175	4656 ± 120	4017 ± 120
CTQ 650	C IV	5460 – 5500	5920 – 5960	5615 – 5800	3275 ± 120	1820 ± 120
	C III]	6630 – 6700	7250 – 7300	6750 – 7195	3189 ± 120	1818 ± 120
CTQ 803	C IV	5600 – 5630	6005 – 6055	5645 – 5970	4409 ± 120	2418 ± 120
	C III]	6490 – 6550	7365 – 7450	6940 – 7325	4271 ± 120	2923 ± 120
CTQ 953	Si IV	4790 – 4810	5080 – 5130	4815 – 5070	6060 ± 120	2850 ± 120
	C IV	5200 – 5250	5830 – 5910	5270 – 5675	5793 ± 120	2700 ± 120
	C III]	6415 – 6485	6915 – 7010	6510 – 6870	5650 ± 120	2155 ± 120
CTQ 975	C IV	5675 – 5695	6395 – 6430	5750 – 6185	5176 ± 120	1833 ± 120
	C III]	6795 – 6835	7695 – 7740	7030 – 7590	4933 ± 120	2673 ± 120
CTQ 1061	Si IV	5880 – 5910	6275 – 6310	5950 – 6260	3745 ± 120	2289 ± 120
	C IV	6375 – 6435	6950 – 7040	6575 – 6880	3208 ± 120	1940 ± 120
	C III]	7740 – 7800	8620 – 8690	8210 – 8515	2315 ± 120	1988 ± 120
HB 89 [0329-385]	Si IV	4630 – 4670	4955 – 5000	4705 – 4930	4627 ± 120	2629 ± 120
	C IV	5060 – 5110	5900 – 6000	5130 – 5525	6284 ± 120	4242 ± 120
	C III]	6010 – 6050	6945 – 6985	6290 – 6820	6509 ± 120	3126 ± 120
J 002830.....	C IV	6460 – 6510	7835 – 7870	6620 – 7190	2775 ± 120	3668 ± 120
J 214355.....	Si IV	4915 – 4940	5275 – 5320	4960 – 5240	5542 ± 120	2324 ± 120
	C IV	5325 – 5375	6210 – 6280	5405 – 5760	4870 ± 120	2976 ± 120
	C III]	6460 – 6510	7835 – 7870	6620 – 7190	7409 ± 120	5668 ± 120
J 221516.....	Si IV	5000 – 5050	5310 – 5370	5095 – 5300	4331 ± 120	2239 ± 120
	C IV	5370 – 5430	5900 – 5960	5615 – 5870	2589 ± 120	2048 ± 120
	C III]	6600 – 6650	7295 – 7340	6915 – 7190	2948 ± 120	1784 ± 120
J 224743.....	Si IV	4675 – 4735	5225 – 5275	4905 – 5180	4587 ± 120	2993 ± 120
	C IV	5220 – 5280	5720 – 5765	5335 – 5690	7924 ± 120	3658 ± 120
	C III]	6315 – 6390	7135 – 7215	6540 – 7130	–	–

5

Variability Measurements

Continuum and emission line light curves are shown in appendix A. In this chapter, a variability analysis of them is presented using some common estimators defined below.

5.1 Variability Estimators

There are several parameters in the literature to estimate variability. In this work we have used estimators that are frequently used in reverberation studies. One of the most frequently used is the *mean fractional variation* (Rodrigues-Pascual et al. 1996, Peterson et al. 2005), which in addition with the *maximum-minimum ratio* and the *variability amplitude*, will describe the variability of our sample.

Let us say that we are estimating the variability of the flux f for each quasar in the sample. Then, each estimator is defined as follows:

Maximum - Minimum Ratio ($R_{\rm max}$): Is defined as the ratio between the maximum and minimum values of f.

$$R_{\rm max} = \frac{f_{\rm max}}{f_{\rm min}} \tag{5.1}$$

Variability Amplitude ($A_{\rm var}$): Defined as the peak-to-peak difference of f relative its minimum value given in percentage.

$$A_{\rm var} = \left(\frac{f_{\rm max} - f_{\rm min}}{f_{\rm min}}\right) \cdot 100\% = \left(\frac{f_{\rm max}}{f_{\rm min}} - 1\right) \cdot 100\% = (R_{\rm max} - 1) \cdot 100\% \tag{5.2}$$

$A_{\rm var}$ and $R_{\rm max}$ measure the amplitude of the variability and they are linked together by the relation

$$A_{\rm var} = 100 \cdot (R_{\rm max} - 1) \tag{5.3}$$

thus, both give us the same information, even when $A_{\rm var}$ is more direct at first sight. However, these estimators are very sensitive to outliers.

Mean Fractional Variation ($F_{\rm var}$): Commonly used in reverberation studies (Rodrigues-Pascual 1996, Peterson 2001), it is an estimate of the root-mean-square of the light curve with respect to its mean, correcting by the effect of data uncertainty. Quantitatively,

$$F_{\rm var} = \frac{\left(\sigma^2 - \Delta^2\right)^{1/2}}{\bar{f}} \tag{5.4}$$

where σ, Δ and $\bar{f}$ are defined as

$$\bar{f} = \frac{1}{N}\sum_{i=1}^{N} f_i \tag{5.5}$$

$$\sigma^2 = \frac{1}{N-1}\sum_{i=1}^{N} (f_i - \bar{f})^2 \tag{5.6}$$

$$\Delta^2 = \frac{1}{N}\sum_{i=1}^{N} \delta^2 \tag{5.7}$$

where $\bar{f}$, σ and Δ refers to the mean flux, light curve root-mean-square and the mean uncertainty of the measurements, respectively. Kaspi et al. (2000, 2005, 2007) used the so called *intrinsic normalized variability measure* σ_N which is defined in terms of $F_{\rm var}$ according to $\sigma_N = 100 \cdot F_{\rm var}$. By definition, the mean fractional variation $F_{\rm var}$ is less sensitive to outliers than the variability amplitude $A_{\rm var}$.

Beyond the importance of the quantitative information given by these estimators, a simple way to check variability is by visual inspection of every light curve. In fact, visual inspection of different light curves for a particular object is done to select the best reverberation data. This is because besides a large variability we also require enough structure in the light curves in order to carry out reverberation mapping.

5.2 Variability Measurements

Variability measurements in this work have to be treated with caution. The variability amplitude scale is different for continuum and emission line measurements since the normalization of the fluxes in both cases are with respect to different things. On one hand we have that continuum variability is measured against a weighted geometrical mean of field stars according with (3.25), and, on the other hand we have that emission lines are compared against a nearby star according with (4.9). Fractional variability $F_{\rm var}$ is an exception of this since it is normalized by the mean flux.

However, since we aim to compare the variability pattern between continuum and emission lines, the scale of the variability measurement is not important.

The first checking task we do to select potentially variable sources is a χ^2_ν test, in which the null hypothesis is that the differential light curve is constant with time. This test is performed every time a new data point is obtained for the DLC. The advantage of the χ^2_ν test is its low sensitivity to outliers measurements and then, if a quasar passes the test, its variability is ensured at a 95% of confidence level.

Variability measurements are listed in tables 5.1, 5.2 and 5.3. Columns (1) and (2) correspond to the object name and the type of light curve (continuum or emission line light curve). Columns (3), (4) and (5) correspond to the variability estimators already defined for each light curve. In columns (6) and (7) the χ^2_ν values are listed for the real light curve and for a constant magnitude light curve at a 95% confidence level, where ν is the number of points in the light curve. If the value in column (6) is larger than in column (7), then the null hypothesis (constant light curve) is rejected. Quasars are sorted from the highest to lowest variability given by $A_{\rm var}$ in the continuum light curve.

5.3 Analysis

From the beginning of this project (early 2005), the amplitude variability has played an important role selecting variable objects from the continuum monitoring. In the following years, the implementation of the χ^2_ν test confirmed that the variability selection criterion has been successful for most of the sample. Nevertheless, there are some objects that were catalogued as suitable candidates for spectroscopic monitoring because of their large amplitude variation, but without taking into account the intrinsic uncertainty of the DLC. An example of this is G 2912, the faintest quasar of the sample with a very high amplitude of its DLC ($\sim 37\%$). However the error bars show a very high uncertainty in magnitude, mostly due to the low signal-to-noise of the object. This effect is reflected in the χ^2_ν test which shows that, within the uncertainties, is not an intrinsic variable object, and even if it were, it is not a good candidate for reverberation studies. Other few cases presenting this effect or random DLCs have been found (CTQ 412 and CTQ 299 for instance) and reveal the significant role of the χ^2_ν test and the visual inspection of the light curves.

5.3.1 Continuum Variability

An histogram for the variability amplitude for the whole sample is shown in figure 5.1, from which outlier measurements, like G 2912 mentioned before, are ignored. In general, all quasars show some intrinsic variability whose amplitude spans from $\sim 5\%$ to $\sim 50\%$ in flux from which, most of them are found to vary between 10% and 20% in amplitude, with mean of 18.91% and median 15.78%.

The variability amplitude of the mean field stars magnitudes is very low and is also shown on the right of the histogram. The mean and median amplitudes correspond to 2.05% and 1.69% respectively, which translates into ~ 0.02 mag which validates the fixed minimum magnitude uncertainty in the photometry of $\Delta m \sim 0.03$ discussed in section §**??**. Therefore field stars are constant within the photometric errors, and then the variability measured for each quasar is intrinsic and not due to changes in the comparison field stars flux.

In a first stage of the monitoring campaign, the histogram for the amplitude variability of quasars has been divided in three groups according to the following selection criteria: Quasars with variability amplitude $A_{\rm var} \geq 22\%$ have been selected for the spectrophotometric monitoring, defining the spectrophotometric sample which is composed by 15 sources. Objects with $A_{\rm var}$ between 10 and 22% are continued being photometrically monitored and those with amplitudes less than 10% are discarded from both monitoring. We expect to have the most variable objects in the spectrophotometric monitoring according to the criteria adopted. However, the most variable sources, those with a highly structured light curves, do not necessarily have the highest variability amplitude as shown in the light curves (see appendix A). For example, high amplitude variations can be obtained from sources whose light curves are monotonically increasing/decreasing. This is important since the long term aim of this project is to obtain reverberation measurements based on cross correlation analysis, where the presence of "events" (i.e. change in the derivative in the light curve) are necessary in order to obtain reliable measurements of time delays. This effect can be seen in figure 5.2 which shows an histogram for the fractional variability (which is, as mentioned before, a measure of the root-mean-square of the light curve). The spectrophotometric sample, selected by $A_{\rm var}$, is shown in blue and has a nearly uniform distribution, farther to be concentrated as the most variable sources when using the $F_{\rm var}$ estimator.

However, line response is expected for sources with large amplitude variability and, therefore, a new selection criteria needs to consider both requirements. For sake of automatization, the sources will be sorted by fractional variability instead their amplitudes. Objects with $F_{\rm var} \geq 0.05$ and $A_{\rm var} \geq 15\%$ will be selected for a visual inspection of their light curves, which will confirm or discard the object depending on the structure showed by its light curve.

Highly variable sources with variability amplitudes larger than 30%, for which we expect a highly variable line response, represent $\sim 20\%$ of the complete sample. From the size of our sample, this implies that ~ 11 sources should be suitable for reverberation studies and this validates our implemented observational strategy. However, this result might be biased because of the same reason: the observational strategy gives denser light curves for quasars that show an early high variability, at the expense of poorer light curves for the remaining objects, which seem to have spurious variability because of few observations. Therefore, there might be object with undetected high variability due to the smaller sampling of their DLCs.

We can use the σ_N estimator to compare our results with those of Kaspi et al. 2007 who used a sample of 11 high luminosity quasars to study their variability and the feasibility of reverberation mapping on them. In this small sample, quasars were found to be variable using σ_N with a mean of 5.8% and median of 4.1%. In our 5 times bigger sample we found that the mean and median values of σ_N are 3.75% and 3.32% respectively, which are marked in figure 5.2 as vertical dashed lines. The results are not significantly different and reflect the fact that high luminosity and high redshift AGN vary with smaller amplitudes than of lower redshift AGNs.

5.3.2 Emission Lines Variability

Unlike continuum monitoring, emission line light curves are, in general, much shorter and under sampled when compared to broad band data. This is partly because the observational strategy, which trigger the spectroscopic follow up $\sim 1.5-2$ years after the beginning of the imaging monitoring resulting in shorter emission line light curves, and

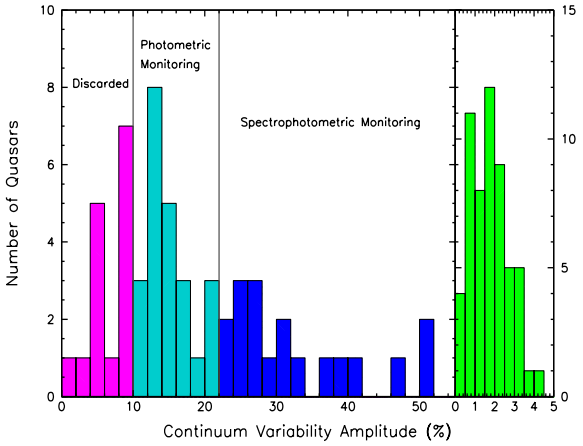

FIGURE 5.1: Histogram with the variability amplitude ($A_{\rm var}$) of the 56 quasars in the sample. Vertical lines represents the limits for discarded, photometric and spectrophotometric monitored objects. The histogram on the right shows the amplitude of the mean field stars variability, used as a comparison in the continuum monitoring.

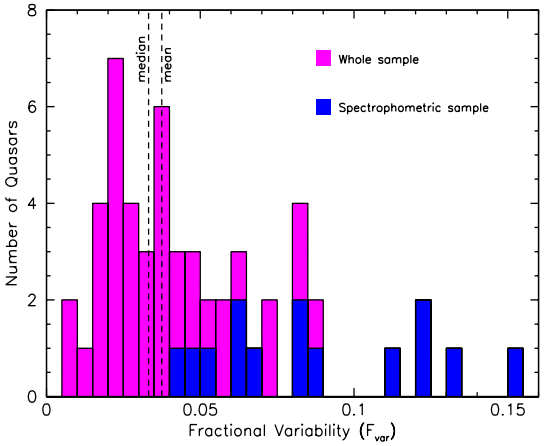

FIGURE 5.2: Mean fractional variability $F_{\rm var}$ parameter for the continuum light curves of the whole sample. The spectrophotometric sample is shown in blue. The mean and median of the distribution are shown as vertical lines.

partly because the allocated observing time, which implies a prioritization[1] of the sources resulting in some quasars better sampled than others. However, there are some objects with enough data points in their light curves to give some preliminary results.

It is found that, in general, all broad emission lines vary in time. Fractional variability of the emission lines is shown in figure 5.3. The mean and median for each emission line are marked with vertical dashed lines. It is found that the mean and median for each line are 7.4% and 5.17% for C IV λ1549 , 9.46% and 6.4% for Si IV λ1400 + O IV] λ1402and 11.6% and 5.76% for the Si III] λ1892 + C III] λ1909. The mean variability is quite large for the emission lines, which might be mainly due noisy data or calibration problems in the spectra. However, the median is quite the similar between the emission lines.

Some objects present extremely high $F_{\rm var}$ values for some emission lines, particularly Si III] λ1892 + C III] λ1909. This effect of very high variability of this particular line can be due to a large uncertainty in the continuum estimate of the line. The C III] rest frame wavelength is redshifted between 7 000 – 8 000 Å where fringing in some observations is severe. Therefore some outlier measurements can be expected for that line in some observations (mainly obtained with the Boller&Chivens spectrograph). In addition, the C III] line usually falls nearly or within the 7 600 Å telluric absorption band, and therefore the line flux is highly uncertain. However, high variability of the C III] line in CTQ 650, J 214355 and J 221516 would be reliable in the sense that they follow the same tendency of the remaining emission lines for each object.

An important empirical result is that the most variable objects in the continuum are not necessary the more variable objects in the emission lines when using the $A_{\rm var}$ estimator. This might be explained in several ways. On the one side, the largest variability amplitude did not ensure the highest variability shown by the fractional variability in the

[1]The prioritization is done according the structure of the continuum light curve.

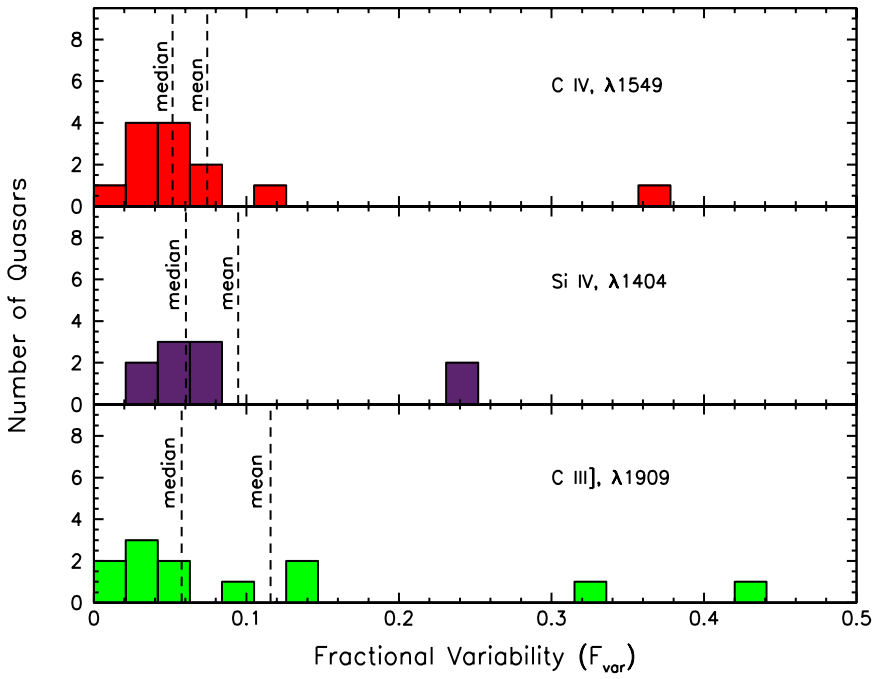

FIGURE 5.3: Mean fractional variability $F_{\rm var}$ histogram of the broad emission lines for our spectroscopic sample with a bin width of 0.02. Mean and median of the distributions are represented by vertical lines.

continuum as mentioned in the continuum analysis. Then, we are probably also seeing this effect in the emission lines.

Focusing in the C IV line, we detect that for highly variable continuum sources ($A_{\rm var} \geq 30\%$)the line amplitude is roughly 3-4 times lower. For continuum variations of $A_{\rm var} \sim 20-30$ the line response is of the same order. Using the $F_{\rm var}$ estimator we found similar results but the difference in the first case decrease to 1.5-2. Hence, it can be possible that other properties in he physics of the BLR, such as geometry or the physical state of the gas, can be playing an active role diluting or reinforcing the emission of the line emitting gas. However, due the limited length of the emission line light curves it is too early to draw statistical conclusions about them, so we can consider this result tentative.

Only a handful of objects are found to have enough points in their light curves to see some structure for each emission line. The most promising sources are CTQ 953, CTQ 803 and J 221516.

TABLE 5.1: VARIABILITY MEASUREMENTS

Object (1)	Light Curve (2)	$A_{\rm var}$ (3)	$F_{\rm var}$ (4)	$R_{\rm max}$ (5)	χ^2_ν (6)	$\chi^2_\nu(P=0.05)$ (7)
Photometric and Spectrophotometric Monitored Objects						
CTQ 975	Continuum	51.08	0.12	1.5108 ± 0.0764	463.076	27.59
	C IV	21.27	0.0774	1.2127 ± 0.0697	33.74	13.28
	C III]	113.87	0.331	2.1387 ± 0.3162	22.27	13.28
J002830.4-281706...	Continuum	50.63	0.1507	1.5063 ± 0.0491	492.388	18.31
	C IV	–	–	–	–	–
CTQ 320	Continuum	46.02	0.1105	1.4602 ± 0.0444	549.132	31.41
	Si IV	39.86	0.0408	1.3986 ± 0.3161	15.97	20.09
	C IV	13.18	0.0287	1.1318 ± 0.0531	22.35	20.09
	C III]	83.09	0.1418	1.8309 ± 0.3427	11.99	20.09
CTQ 286	Continuum	41.78	0.1235	1.4178 ± 0.0474	878.849	36.42
	Si IV	14.61	0.0511	1.1461 ± 0.0421	127.56	11.35
	C IV	6.45	0.0328	1.0645 ± 0.0836	4.04	11.35
	C III]	6.45	0.0328	1.0645 ± 0.0836	4.04	11.35
CTQ 650	Continuum	39.9	0.1301	1.399 ± 0.0617	337.813	18.31
	C IV	111.94	0.3634	2.1194 ± 0.118	454.83	9.21
	C III]	173.01	0.4389	2.7301 ± 0.4044	90.9	9.21
J214355.0-295158...	Continuum	32.68	0.0818	1.3268 ± 0.0552	400.075	36.42
	Si IV	28.3	0.0738	1.283 ± 0.147	6.29	11.35
	C IV	33.97	0.123	1.3397 ± 0.0722	36.4	11.35
	C III]	24.34	0.1038	1.2434 ± 0.246	1.48	11.35
CTQ 367	Continuum	31.46	0.0871	1.3146 ± 0.0369	413.71	30.14
	Si IV	0.8	0.0792	1.008 ± 0.1131	0.01	6.64
	C IV	3.41	0.0223	1.0341 ± 0.0476	0.53	6.64
	C III]	7.85	0.0604	1.0785 ± 0.123	0.44	6.64
CTQ 564	Continuum	29.02	0.0629	1.2902 ± 0.0508	413.71	30.14
	Si IV	110.91	0.3166	2.1091 ± 0.4921	11.95	9.21
	C IV	3.41	0.0369	1.0864 ± 0.0318	8.15	9.21
	C III]	21.03	0.0397	1.2103 ± 0.1893	2.48	9.21
HB89[0329-385]....	Continuum	27.97	0.0626	1.2797 ± 0.0557	107.195	25
	Si IV	28.59	0.0566	1.2859 ± 0.1861	3.63	11.35
	C IV	7.87	0.0311	1.0787 ± 0.0168	26.52	11.35
	C III]	16.75	0.0547	1.1675 ± 0.0569	10.28	11.35
CTQ 953	Continuum	27.57	0.0612	1.2757 ± 0.0478	160.326	35.17
	Si IV	21.21	0.0495	1.2121 ± 0.0796	45.74	21.67
	C IV	19.95	0.0672	1.1995 ± 0.0347	139.31	21.67
	C III]	11.64	0.0259	1.1164 ± 0.0382	31.97	21.67
J224743.5-310306...	Continuum	27.41	0.0683	1.2741 ± 0.0379	184.301	26.3
	Si IV	67.54	0.2372	1.6754 ± 0.1267	58.24	11.35
	C IV	17.35	0.0609	1.1735 ± 0.057	11.85	11.35
	C III]	15.45	0.0197	1.1545 ± 0.0988	4.78	11.35
J221516.0-294424...	Continuum	24.41	0.0454	1.2441 ± 0.0612	92.544	32.67
	Si IV	150.44	0.2471	2.5044 ± 0.2396	126.84	16.81
	C IV	16.12	0.0517	1.1612 ± 0.0234	125.21	16.81
	C III]	51.17	0.137	1.5117 ± 0.1262	88.22	16.81

TABLE 5.2: VARIABILITY MEASUREMENTS – CONTINUED

Object (1)	Light Curve (2)	$A_{\rm var}$ (3)	$F_{\rm var}$ (4)	$R_{\rm max}$ (5)	χ^2_ν (6)	$\chi^2_\nu(P=0.05)$ (7)
Photometric and Spectrophotometric Monitored Objects						
CTQ 1061	Continuum	24.11	0.0809	1.2411 ± 0.0356	391.507	33.92
	Si IV	12.73	0.0715	1.1273 ± 0.0726	3.48	6.64
	C IV	1.28	0.0036	1.0128 ± 0.0118	1.26	6.64
	C III]	0.09	0.0374	1.0009 ± 0.0521	0	6.64
CTQ 803	Continuum	22.18	0.053	1.2218 ± 0.0361	117.299	26.3
	C IV	19.89	0.0544	1.1989 ± 0.0794	41.55	16.81
	C III]	12.56	0.0066	1.1256 ± 0.125	13.27	16.81
CTQ 406	Continuum	16.63	0.0444	1.1663 ± 0.0377	61.257	22.36
	Si IV	26.91	0.0394	1.2691 ± 0.1498	4.84	13.28
	C IV	17.46	0.0495	1.1746 ± 0.0766	17.75	15.09
Photometric Monitored Objects						
CTQ 252	*R*	27.51	0.0845	1.2751 ± 0.0382	152.374	16.92
CTQ 250	*R*	25.61	0.0591	1.2561 ± 0.0438	93.032	21.03
CTQ 261	*R*	22.78	0.0578	1.2278 ± 0.0361	87.55	18.31
J001743.9-293604...	*R*	22.59	0.071	1.2259 ± 0.0354	150.088	21.03
CTQ 500	*R*	21.56	0.0852	1.2156 ± 0.0389	118.199	14.07
CTQ 299	*R*	20.263	100.331	0.1001 ± 0.0094	6.859	1.878
J023805.8-274337...	*R*	19.59	0.0499	1.1959 ± 0.0423	28.662	12.59
CTQ 272	*R*	19.44	0.0708	1.1944 ± 0.035	93.782	14.07
J222006.7-280324...	*R*	16.91	0.0302	1.1691 ± 0.0487	48.043	22.36
CTQ 656	*R*	16.64	0.0537	1.1664 ± 0.0367	77.699	16.92
CTQ 391	*R*	16.38	0.0389	1.1638 ± 0.0621	36.2	18.31
CTQ 481	*R*	16.11	0.0475	1.1611 ± 0.0379	58.942	16.92
CTQ 491	*R*	15.45	0.0396	1.1545 ± 0.0361	34.156	14.07
CTQ 460	*R*	15.45	0.0411	1.1545 ± 0.0332	106.745	31.41
J221814.4-300306...	*R*	15.13	0.0349	1.1513 ± 0.0422	57.933	23.69
CTQ 504	*R*	15.08	0.0399	1.1508 ± 0.033	41.157	15.51
CTQ 682	*R*	14.49	0.0392	1.1449 ± 0.0461	27.607	14.07
CTQ 280	*R*	14.25	0.0355	1.1425 ± 0.0402	76.299	30.14
CTQ 247	*R*	13.86	0.0411	1.1386 ± 0.0371	42.08	15.51
CTQ 322	*R*	13.76	0.0368	1.1376 ± 0.0314	86.464	30.14
CTQ 291	*R*	12.62	0.0268	1.1262 ± 0.0331	55.56	31.41
CTQ 480	*R*	11.46	0.0283	1.1146 ± 0.0455	30.718	19.68
CTQ 412	*R*	11.41	0.0251	1.1141 ± 0.0429	10.347	12.59
CTQ 1060	*R*	11.28	0.009	1.1128 ± 0.0434	30.528	35.17
J003354.7-295754...	*R*	10.63	0.0315	1.1063 ± 0.0344	25.162	15.51
Photometrically Discarded Objects						
G 2912	*R*	35.87	0.0805	1.3587 ± 0.1129	20.212	12.59
CTQ 296	*R*	9.85	0.0227	1.0985 ± 0.0304	34.592	25
CTQ 260	*R*	9.59	0.0222	1.0959 ± 0.0315	21.072	16.92
CTQ 493	*R*	9.41	0.0197	1.0941 ± 0.0366	13.292	12.59
J233133.4-274842...	*R*	9.34	0.0247	1.0934 ± 0.0392	16.841	12.59
CTQ 400	*R*	8.72	0.024	1.0872 ± 0.0387	6.682	9.49

TABLE 5.3: VARIABILITY MEASUREMENTS – CONTINUED

Object (1)	Light Curve (2)	$A_{\rm var}$ (3)	$F_{\rm var}$ (4)	$R_{\rm max}$ (5)	χ^2_ν (6)	$\chi^2_\nu(P=0.05)$ (7)
Photometrically Discarded Objects						
CTQ 872	*R*	8.51	0.0217	1.0851 ± 0.0356	10.758	12.59
CTQ 452	*R*	8.33	0.0211	1.0833 ± 0.0318	18.664	16.92
CTQ 814	*R*	7.05	0.0178	1.0705 ± 0.0316	9.439	11.07
J235340.3-292436...	*R*	6.36	0.0231	1.0636 ± 0.0323	9.695	9.49
CTQ 783	*R*	5.882	4.862	0.0294 ± 0.0107	0.597	0.981
CTQ 498	*R*	5.54	0.0098	1.0554 ± 0.0291	4.654	12.59
CTQ 408	*R*	5.42	0.0101	1.0542 ± 0.0313	4.725	12.59
CTQ 599	*R*	4.07	0.0161	1.0407 ± 0.0341	1.983	11.07
CTQ 509	*R*	1.58	0.0183	1.0158 ± 0.0281	0.621	11.07

6

Preliminary Results and Reverberation Measurements

To date, the monitoring program has yielded three objects with emission line light curves with enough structure to perform a preliminary reverberation analysis of them. The selected objects are CTQ 803, CTQ 953 and J 221516 and in the following I will present preliminary results for them.

6.1 Lag estimate

The estimate of the BLR size is a key step in reverberation mapping and depends on the emission line used. To obtain $R_{\rm BLR}$ we need to measure the emission line response time lag with respect to continuum changes. This is done using a cross correlation analysis between the continuum and the emission line light curves.

Because of the unevenly sampled nature of the light curves, we have used a technique developed by Edelson & Krolik (1988) known as the Discrete Correlation Function, or DCF, which is the cross correlation between binned light curves. There are many other techniques for cross correlation analysis such as the ICCF (Gaskell and Peterson 1987) and ZDCF (Alexander 1997) methods, commonly used for reverberation studies. However, the number of points in our emission line light curves are still less than plays a fundamental role on them, and therefore we have used the DCF as a first attempt to obtain preliminary results.

The choice of the bin size is a trade-off between the desired resolution and the precission of the DCF. We have found that a bin size of $\Delta\tau \sim 85-95$ days is a good choice given the resolution of the spectroscopic light curves (one point every ~ 3 months).

TABLE 6.1: PRELIMINARY REST FRAME TIME LAGS FROM TIME-SERIES ANALYSIS

Object	Line	R_{max}	F_{var}		τ_{peak}	τ_{cent}	σ_τ
			Continuum	Line	(days)	(days)	(days)
(1)	(2)	(3)	(4)	(5)	(6)	(7)	(8)
CTQ 803	C IV	1.199 ± 0.079	0.053	0.0544	303	284	18
	C III]	1.126 ± 0.125	0.053	0.007	253	276	25
CTQ 953	Si IV	1.2121 ± 0.0796	0.0612	0.0495	189	205	92
J 221516.....	Si IV	2.5044 ± 0.2396	0.0454	0.2471	180	174	87
	C IV	1.1612 ± 0.0234	0.0454	0.0517	282	278	50

The lag can be calculated from the peak (τ_{peak}) or the centroid (τ_{cent}) of the DCF distribution. The τ_{peak} corresponds to the lag at which the DCF reaches its maximum value, while the τ_{cent} corresponds to

$$\tau_{cent} = \frac{\int \tau \cdot \mathrm{DCF}(\tau)\, d\tau}{\int \mathrm{DCF}(\tau)\, d\tau} \tag{6.1}$$

It is usual in reverberation studies to perform this integration within a lag region where $\mathrm{DCF}(\tau) \geq 0.6\,\mathrm{DCF}_{max}$. However, the DCF of the selected quasars argues that they are well behaved functions in most of the lag domain except at the boundaries where peaks appear sometimes (P. Arévalo, private communication). In order to determinate if the peaks in the DCF arise from boundary effects or from real correlations of the time series we have calculated curves of significance using 1000 Monte Carlo simulations of the continuum light curves and then cross correlated them with the emission line light curves. Each simulation consists on a cross correlation of a synthetic continuum DLC, which has the same properties of the real continuum DLC such as variability amplitude and power spectrum, with the emission line light curve. As a result we obtain curves for a 95 and 99% confidence level for the real DCF (i.e. the DCF calculated from the real continuum and emission line light curves). Therefore, any peak of the real DCF larger than this confidence curves is real at a 95 or 99% confidence level, respectively. In this work the centroid determination is done over the lags where $\mathrm{DCF}(\tau) \geq \mathrm{CL}_{95}(\tau)$, where $\mathrm{CL}_{95}(\tau)$ corresponds to the 95% confidence level curve.

The uncertainty associated with the centroid lag τ_{cent} is calculated from the dispersion of the DCF in the same lag domain

$$\sigma_\tau^2 = \frac{\int \tau^2 \cdot \mathrm{DCF}(\tau)\, d\tau}{\int \mathrm{DCF}(\tau)\, d\tau} - \tau_{cent}^2 \tag{6.2}$$

Discrete cross correlation functions are shown in figures 6.1, 6.2 and 6.3. From them, some noisy DCF can be seen which do not show any structure or have several peaks. Those cases have been excluded from further analysis and correspond to the DCF using C III] for J 221516 and CTQ 953, and also the DCF of C IV for CTQ 953. Peak and centroid lags for each DCF are presented in table 6.1.

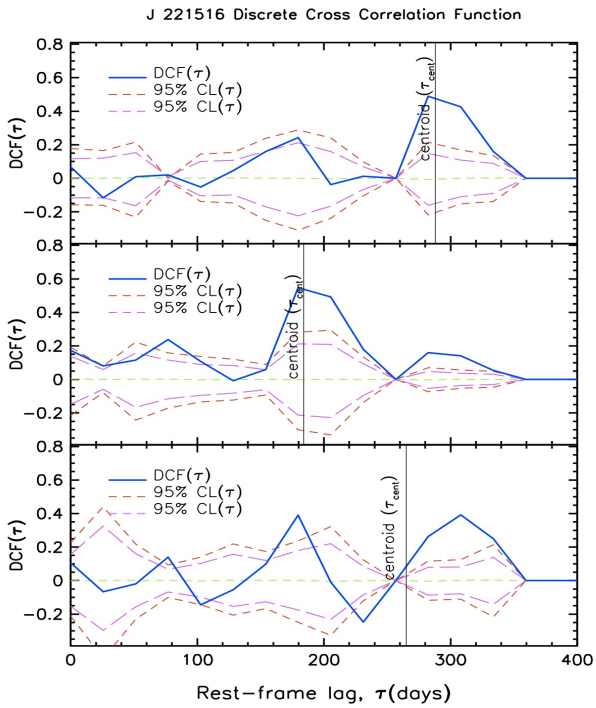

FIGURE 6.1: Discrete Correlation Function between the continuum and C IV (top), Si IV (middle) and C III] (bottom) emission lines for quasar J 221516.

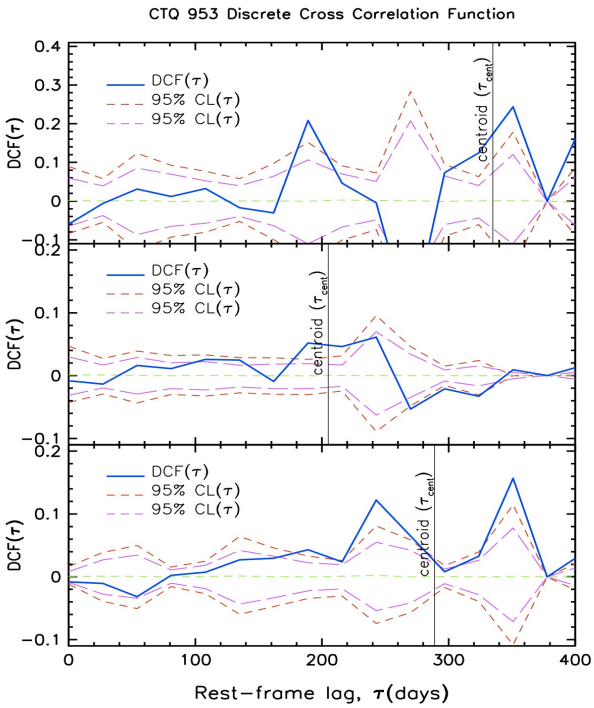

FIGURE 6.2: Discrete Correlation Function between the continuum and C IV (top), Si IV (middle) and C III] (bottom) emission lines for quasar CTQ 953.

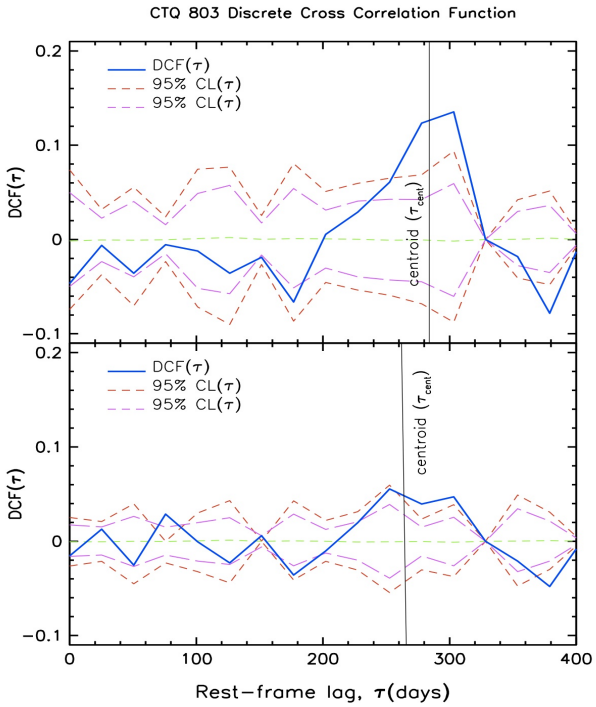

FIGURE 6.3: Discrete Correlation Function between the continuum and the C IV (top) and C III] (bottom) emission lines for quasar CTQ 803. The vertical line in each plot indicates the centroid lag $\tau_{\rm cent}$ of the distribution.

6.2 Filling the high end of the luminosity range in the $R_{\rm BLR} - L_{\rm UV}$ relation

Before calculating black hole masses we would like to determine whether our objects follow the $R_{\rm BLR} - L_{\rm UV}$ relation in the UV based on reverberation mapping of the C IV emission, studied by Peterson et al. (2005) and re examined by Kaspi et al. (2007). A well calibrated $R_{\rm BLR} - L_{\rm UV}$ relation of the form $R_{\rm BLR} \propto L_{\rm UV}^{\alpha}$ is crucial to obtain reliable black hole masses from single epoch observations. Nevertheless, the slope α for high redshift (and therefore, high luminosity) objects is still unexplored.

We start from the baseline of an existing relationship between luminosity and the BLR size as mentioned in chapter 1, and parametrized according to

$$\log R_{\rm BLR} \propto \alpha \log L_{\rm UV} \tag{6.3}$$

In 2005, Peterson et al. measured the BLR size of the dwarf Seyfert NGC 4395 and added it to the sample of Seyferts with BLR size measured from the C IV emission line in the UV, which extends the $R_{\rm BLR} - L_{\rm UV}$ relation to the lowest possible luminosities, covering a luminosity range between $10^{39} - 10^{45}\,{\rm erg\,s^{-1}}$. The results were categoric and the slope in the UV was found to be $\alpha = 0.79 \pm 0.06$, quite different compared from an earlier estimate of 0.56 from Kaspi et al. (2005), and farther away from the expected naive slope of 0.5 assuming the same BLR parameters for all AGNs.

In 2007, Kaspi et al. obtained the first BLR size measurement for a high luminosity (and hence high redshift) quasar and the revised relation in the UV was found to have a slope of 0.52 ± 0.04, much closer to the optical relation. These changes of the value of α every time a point is added to the relation clearly shows the need of reverberation mapping measurements, particularly at the high luminosity end. Did Kaspi et al. find a representative BLR size at high redshift or it is just an outlier measurement?. This was particularly worrying since the object studied by Kaspi et al. was classified as a radio-loud AGN, and therefore its luminosity and continuum variability could be influenced by the jet emission.

Our preliminary results suggest that Kaspi et al. (2007) was right. Actually, adding the BLR size $R_{\rm BLR}$ and the specific luminosity at 1350Å of our three sources to the Peterson and Kaspi samples, we find with a simple lineal regression that

$$\log R_{\rm BLR}\,({\rm C\,IV}) = (-22 \pm 0.12) + (0.52 \pm 0.07) \log L_{\rm UV} \tag{6.4}$$

in perfect agreement with the relation (1.10) of Kaspi et al. 2007, as shown in figure 6.4. This is an important preliminary confirmation of the $R_{\rm BLR} - L_{\rm UV}$ relation at high-redshift and high luminosity AGN based in the C IV emission line.

6.3 Preliminary Black Hole Masses

Based on a study of 35 low and intermediate luminosity AGNs using the Hβ line, Peterson et al. (2004) found that the most consistent virial products (or black hole masses) were those estimated from the centroid lag $\tau_{\rm cent}$ and the line dispersion $\sigma_{\rm line}$ as measures of the BLR size and emission line velocity, respectively. In addition, if we consider that the peak lag is dependent on the bin size used by the DCF, we will adopt the centroid lag ($\tau_{\rm cent}$) as the measurement of the BLR size for our objects.

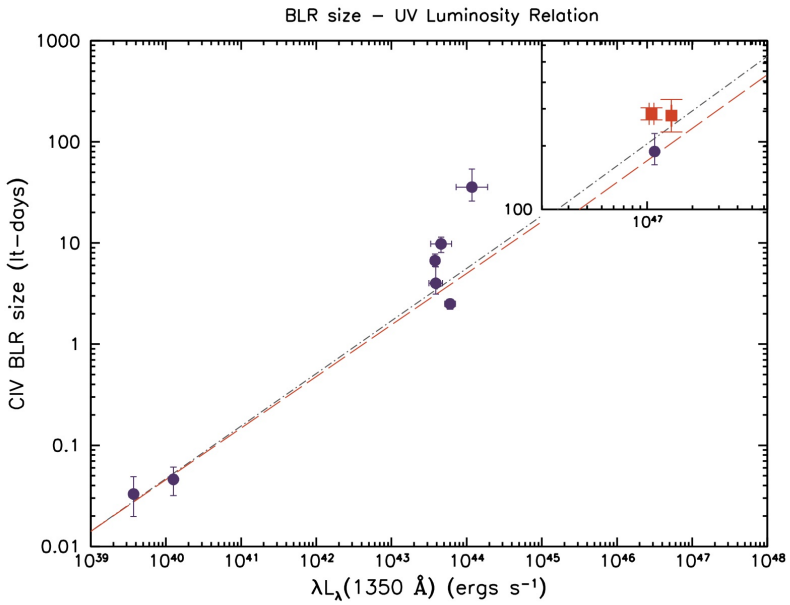

FIGURE 6.4: $R_{\rm BLR} - L_{\rm UV}$ relation for the UV continuum based on C IV reverberation measurements. CTQ 803, J 221516 (red squares) and S5 0836 (in violet, from Kaspi et al. 2007) are in the upper right corner zoom. Peterson et al (2005) sample are shown as violet dots. The dot-dashed grey line is the relation obtained by Kaspi et al. in 2007 with a slope of 0.52 ± 0.05, while the dashed red line is our fit with a slope of 0.52 ± 0.07.

The uncertainty in the measure of the black hole mass is as important as the black hole mass itself. In terms of the virial product

$$M_{\rm BH} = f\,{\rm VP}(R_{\rm BLR}, {\rm v}) = f\,\frac{R_{\rm BLR}\,{\rm v}^2}{G} \tag{6.5}$$

we have that the relative uncertainty is given by

$$\sigma^2_{\rm VP} = \left(\frac{\sigma^2_\tau}{\tau^2} + \frac{4\sigma^2_{\rm v}}{{\rm v}^2}\right){\rm VP}^2 \tag{6.6}$$

Our main goal of measuring black hole masses of high redshift quasars is determinated by the scale factor f in (6.5), which holds information about the geometry and kinematics of the BLR. Generally, f is assumed to be $\sim 1-3$. However, Onken (2004) found a mean value of $\langle f \rangle = 5.5$ assuming that both, active and quiescent galaxies follow the same $M_{\rm BH} - \sigma_\star$ scaling relation. Hence, in the following we will assume f=5.5.

Virial products and black hole masses for our three objects are presented in table 6.2. Also, black hole masses for each quasar are shown in figures 6.5, 6.6 and 6.7 using the Si IV , C IV and C III] emission lines, respectively. Diagonal lines correspond to BH masses accreting at $1L_{\rm Edd}$ and $10L_{\rm Edd}$ according to equation (1.5).

These black hole masses are the largest ever measured using reverberation mapping, with the exception of S5 0836+71, the quasar studied by Kaspi et al. (2007). Nevertheless, the mass of S5 0836 was calculated using a gas velocity of $\sqrt{3}{\rm v}_{\rm FWHM}/2$ rather than with the line dispersion $\sigma_{\rm line}$.

TABLE 6.2: PRELIMINARY REST-FRAME LAG, LINE WIDTH, VIRIAL PRODUCT AND BLACK HOLE MASS

Object	Line	$\tau_{\rm cent}$ (days)	$\sigma_{\rm line}$ ($\rm km\,s^{-1}$)	$c\tau_{\rm cent}\sigma^2_{\rm line}/G$ ($10^8\,\rm M_\odot$)	$M_{\rm BH}$ ($10^9\,\rm M_\odot$)
(1)	(2)	(3)	(4)	(5)	(6)
CTQ 803	C IV	284 ± 19	2419 ± 120	3.24 ± 0.39	1.78 ± 0.21
	C III]	276 ± 25	2924 ± 120	4.63 ± 0.55	2.53 ± 0.30
CTQ 953	Si IV	205 ± 92	2845 ± 120	3.24 ± 1.49	1.78 ± 0.82
J 221516.....	Si IV	174 ± 87	2239 ± 120	1.70 ± 0.87	0.94 ± 0.48
	C IV	278 ± 50	2048 ± 120	2.28 ± 0.48	1.25 ± 0.26

An weighted average BH mass for each quasar can be calculated according to

$$M_{BH} = \frac{\sum_i M_i/\sigma_i^2}{\sum_i 1/\sigma_i^2}, \qquad i = \rm Si\,IV, C\,IV, C\,III] \tag{6.7}$$

We have obtained that $M_{\rm BH}^{\rm CTQ\,803} = 2.03 \pm 0.37 \times 10^9\,\rm M_\odot$, $M_{\rm BH}^{\rm CTQ\,953} = 1.78 \pm 0.82 \times 10^9\,\rm M_\odot$ and finally $M_{\rm BH}^{\rm J\,221516} = 1.18 \pm 0.55 \times 10^9\,\rm M_\odot$. It can be seen from figure 6.8 that the mean BH mass for these three objects fall in the super Eddington regime, as discussed in the next section.

6.4 Preliminary Accretion Rates

A rough estimate of the accretion rates for our objects can be made using the transformation between specific and bolometric luminosity given by Marconi et al. (2004) for the *B* band

$$\log\left(\frac{L_{\rm bol}}{\nu_B L_{\nu_B}}\right) = 0.80 - 0.067\,\mathcal{L} + 0.017\,\mathcal{L}^2 - 0.0023\,\mathcal{L}^3 \tag{6.8}$$

where $\mathcal{L} = \log L_{\rm bol} - 12$ and $L_{\rm bol}$ is in units of $\rm L_\odot$. Given that the *B* broad band effective wavelength is ~ 4400Å and the rest frame continuum wavelength 1350Å reaches $4700 - 5000$Å in the observed frame at $z \sim 2.5 - 2.7$, this relation can be used as a first approximation.

Using the specific luminosity in table 4.2 and re arranging (6.8) we find that the bolometric luminosity can be estimated from the root of a cubic polynomial given by

$$0 = \log\left(\frac{\lambda L_\lambda}{10^{12}\,\rm L_\odot}\right) + 0.80 - 1.067\,\mathcal{L} + 0.017\,\mathcal{L}^2 - 0.0023\,\mathcal{L}^3 \tag{6.9}$$

Solving this equation for $\mathcal{L}$ in *Mathematica* we get that $\mathcal{L}^*_{\rm CTQ\,803} = 2.16$, $\mathcal{L}^*_{\rm CTQ\,953} = 2.31$ and $\mathcal{L}^*_{\rm J\,221516} = 2.29$ and thus the bolometric luminosity for each object is given by $L_{\rm bol} = 10^{12+\mathcal{L}^*}\,\rm L_\odot$. The results are shown in table 6.3. For the three quasars the bolometric correction correspond to a factor of 5.2 of the specific luminosity measured in the UV continuum.

TABLE 6.3: BOLOMETRIC LUMINOSITY AND ACCRETION RATES

Object	M_{BH} (10^9 $M_\odot$)	L_{Edd} (10^{47} erg s^{-1})	$\lambda L_\lambda(1350\,\text{Å})$ (10^{46} erg s^{-1})	L_{bol} (10^{47} erg s^{-1})	L_{bol}/L_{Edd}
(1)	(2)	(3)	(4)	(5)	(6)
CTQ 803	2.03 ± 0.37	2.54	10.71 ± 0.40	5.51 ± 0.21	2.17
CTQ 953	1.78 ± 0.82	2.23	15.37 ± 0.30	7.99 ± 0.16	3.58
J 221516.....	1.18 ± 0.55	1.48	14.52 ± 0.08	7.55 ± 0.04	5.10

Surprisingly the L_{bol}/L_{Edd} ratio, which is a measure of the accretion rate for an AGN are found to be larger than one. A possible explanation for this result is that the estimate of the bolometric luminosity is larger than the real one; or the measured specific luminosity at 1350 Å is over estimated from the spectra since the zero flux level in the flux calibration step of the spectra is rather uncertain , which seems to be the most likely. In order to check that, absolute photometry will be required from the broad band imaging. Another explanation would be that Eddington ratio is a strong constrain for accretion but is based on a spherical accretion which might not be case for those objects. Thus, the geometry and kinematics of the accretion might be playing an important role in these sources. In fact, our sample has been drawn from the most luminous quasars found in the southern sky and therefore very high accretion rates are an expected result for our sources.

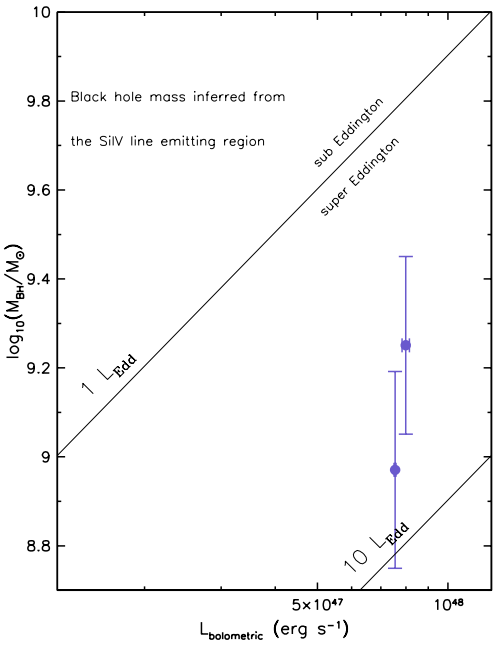

FIGURE 6.5: Black hole masses for CTQ 953 and J 221516 using the Si IV emitting line region versus bolometric luminosity.

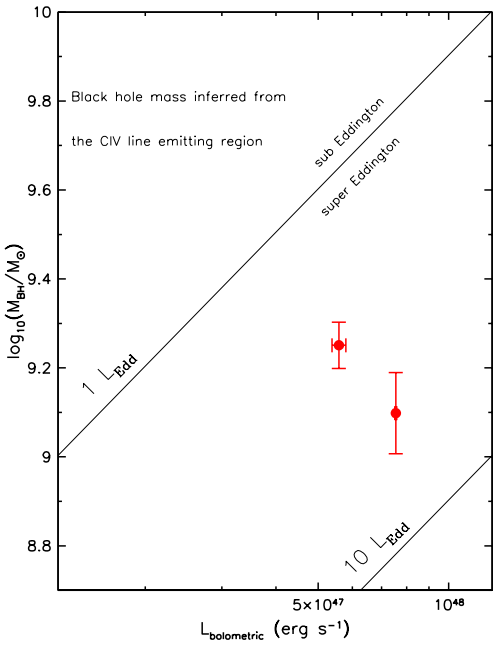

FIGURE 6.6: Black hole masses for CTQ 803 and J 221516 using the C IV emitting line region versus bolometric luminosity.

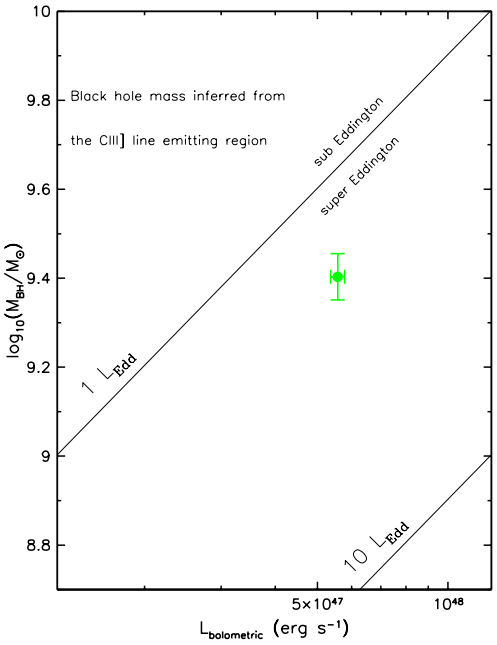

FIGURE 6.7: Black hole mass for CTQ 803 using the C III] emitting line region versus bolometric luminosity.

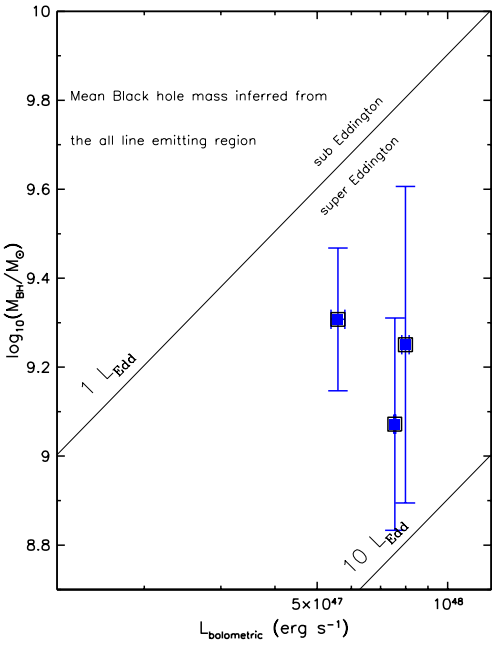

FIGURE 6.8: Weighted mean of black hole masses for CTQ 803, CTQ 953 and J 221516 using the available emission lines for each object versus bolometric luminosity.

7

Conclusions

The actual status and preliminary results of a long term monitoring campaign designed to study the AGN and black hole properties at high redshift has been presented. It has to be kept in mind that the presented preliminary results are based on a monitoring program which is at the mid time of being completed. Here we briefly summarize our findings.

Variability at High Redshift

The variability analysis of the sample has resulted in the identification of 15 "highly" variable quasars in the continuum for which a spectroscopic monitoring has been triggered, which correspond to CTQ 286, CTQ 320, CTQ 367, CTQ 406, CTQ 564, CTQ 650, CTQ 803, CTQ 953, CTQ 975, CTQ 1060, J 002830, J 221516, J 214355, J 224743 and HB89. Furthermore, four more candidates (CTQ 250, CTQ 322, CTQ 261, CTQ 481) will be added to this sample in 2011, increasing the number of candidates for reverberation mapping studies. Comparing with the 4 variable sources found by K07, we have improved the detection of variable sources by a factor of $\sim 4-5$ only by increasing the size of the sample.

The use of a large sample of 56 high luminosity and high redshift quasars allow us to study statistical properties about their variability in the continuum. We find that quasars UV continuum of high luminosity sources vary with lower amplitudes with respect to the optical of low-intermediate luminosity AGNs. In fact, we find that the median of the variability amplitude is around 16% where the optical variability reaches $\sim 70\%$ from Kaspi optical sample (Kaspi et al. 2000). This is basically due to a difference of the system size. High luminosity quasars, where very massive black holes are expected ($M_{\odot} \sim 10^{9}\,M_{\odot}$), have much larger BLR than those of Seyfert galaxies (with $M_{\odot} \sim 10^{6-7}\,M_{\odot}$) and

therefore the probability of a coherent high flux variation is much lower, which yields variability amplitudes lower than of the Kaspi et al. (2000) sample composed by low and intermediate luminosity AGN.

With respect to the emission lines, we found that larger variability amplitude in the continuum does not translate in a larger variability amplitude for the emission lines, which would imply some role of the physical state or kinematics of the gas in the line response. However, more observations are needed to explore this effect at a significant level.

BLR size and the $R_{\rm BLR} - L_{\rm UV}$ Relation

Only three quasars, CTQ803, CTQ953 and J221516, presented enough variability and structure to perform a cross correlation analysis, obtaining the BLR size of them based in three emission lines (C IV , C III] , Si IV). However, the cross correlation function for CTQ953 is still very noisy and therefore, its results are not very significant. Since these quasars have similar luminosity, their BLR might be similar in size. The average size of the C IV emitting region for these sources is found to be ~ 0.24 pc, a factor of ~ 30 larger than the C IV BLR found in typical Seyferts. We can also suggest a stratification of the BLR since the average size for the Si IV and C IV emitting regions are 0.16 pc and 0.24 pc, respectively. Such stratification has been also seen for other species in local AGNs (Onken and Peterson, 2002). Increasing the results for other emission lines also represents a very important result since this gives direct information on the BLR physics.

We have obtained a slope of 0.52 ± 0.07 for the $R_{\rm BLR} - L_{\rm UV}$ relation. Thus we can also confirm, based on these preliminary results, that the $R_{\rm BLR} - L_{\rm UV}$ relation estimated by Kaspi et al. (2007) for the UV continuum holds when adding our sources.

From my point of view, the obtained slope for the $R_{\rm BLR} - L_{\rm UV}$ relation is an important (very) preliminary confirmation, but it is far from being a conclusive result given the relatively high uncertainty in the lags for each emission line of the three sources. Of course, adding more objects to this relation would increase the significance of the resultant slope of the $R_{\rm BLR} - L_{\rm UV}$ relation. Hence, the continuation of the spectrophotometric monitoring for the remaining sources is essential to hopefully obtain more points to improve the relation.

Black Hole Mass and Accretion Rates

The black hole mass and accretion rates of these high luminous sources is the main goal of the reverberation mapping project. As expected, we have found large black hole masses in the early Universe, with masses of the order of $10^9\,{\rm M}_\odot$ based on the preliminary measurements of the most promising sources in our sample (CTQ 803, CTQ 953 and J 221516).

As such, very massive BHs are expected to have very high rates of accretion in the early Universe (those black holes are still around us at $z \sim 0$ but they are not very active anymore because $\dot{M}_{z\sim 0} \ll \dot{M}_{z\sim 2}$). Using a first approximation for the bolometric luminosity we found that all of them are accreting in the Super Eddington regime ($L_{\rm bol} > L_{\rm Edd}$). However, bolometric luminosity from absolute photometry is needed to confirm this preliminary result.

Future Work

The observing program for reverberation mapping was planned for a period of *at least* 9-10 years. To date, 5 years have passed yielding important preliminary results mentioned above.

However, the monitoring is expected to span *at least* 3-4 more years in order to improve the sampling in the continuum and spectroscopic light curves. Improving the sampling of the continuum and emission line light curves is very important in order to obtain reliable and more accurate measurements of the BLR size. In addition, the use of other methods for cross correlation analysis, like the interpolated cross-correlation function (ICCF) of White & Peterson (1994) and the z-transformed discrete correlation function (ZDCF) of Alexander (1997), would possibly enhance the significance of the lag estimation since they are the commonly used for several authors (for example, Kaspi et al. 2007, Peterson et al. 2005, etc) and also would allow a direct comparison between the results of this program with others in the literature.

Also, there are several objects that are expected to be useful for reverberation analysis (15 and 4 more sources to be added in 2011) in the near future. Compared with the six objects currently found in the literature with a measured C IV BLR size, this reverberation mapping project represents a significant step forward. Assuming that half of our sources yield reliable lags and black hole masses, then we would be doubling the number of objects with a BLR size and black hole mass estimated from the C IV emission line.

A Final Remark

It is quite impressive that very massive black holes can be found at high redshift. Considering a present age of the Universe of 13.86 Gyrs old, these quasars are placed in the very early Universe, only ~ 2 Gyrs after the Big Bang. The formation and evolution of these systems is still quite intriguing and is still part of the debate in current astronomy.

Bibliography

[1] BARKHOUSE, W. A. and HALL, P. B. 2001. Quasars in the 2MASS Second Incremental Data Release. The Astronomical Journal 121, Issue 5:2843-2850.

[2] BLANDFORD, R. D., MCKEE, C. F. 1982. Reverberation Mapping of the emission line regions of Seyfert galaxies and quasars. The Astrophysical Journal 255:419-439.

[3] BOYLE, B. J. et al. 1987. The evolution of optically selected QSOs. Mon. Not. R. Astron. Soc. 227:717-738.

[4] BOYLE, B. J. et al. 1988. The evolution of optically selected QSOs - II. Mon. Not. R. Astron. Soc. 235:935-948.

[5] CROOM, S. M. et al. 2004. The 2dF QSO Redshift Survey - XII. The spectroscopic catalogue and luminosity function. Mon. Not. R. Astron. Soc. 349, Issue 4:1397-1418.

[6] EDELSON, R. A., KROLIK, J. H. 1988. The Discrete Correlation Function: A new method for analyzing unevenly sampled variability data. The Astrophysical Journal 333:646-659.

[7] FUKUGITA, M. et al. 1996. The SLOAN Digital Sky Survey photometric system. The Astronomical Journal 111, Issue 4:1748-1756.

[8] GASKELL, C. M., PETERSON, B. M. 1987. The accuracy of cross-correlation estimates of quasar emission-line region sizes. The Astrophysical Journal 65:1-11.

[9] GIVEON, U. et al. 1999. Long-term optical variability properties of the Palomar-Green quasars. Mon. Not. R. Astron. Soc. 306:637-654.

[10] KASPI, S. et al. 2007. Reverberation Mapping of high luminosity quasars: First results. The Astrophysical Journal 659:997-1007.

[11] KASPI, S. et al. 2005. The relationship between luminosity and Broad-Line Region size in Active Galactic Nuclei. The Astrophysical Journal 629:61-71.

[12] KASPI, S. et al. 2000. Reverberation measurements for 17 quasars and the Size-Mass-Luminosity relation in Active Galactic Nuclei.. The Astrophysical Journal 533:631-649.

[13] KASPI, S. et al. 1996. Measurement of the Broad-Line region size in two bright quasars. The Astrophysical Journal 471:L75-L78.

[14] KEMBHAVI, A. K., NARLIKAR, J. V. 1999. Quasars and Active Galactic Nuclei, an introduction. 1ª ed. Cambridge, UK, Cambridge University Press. 463p.

[15] MAOZ , D. et al. 1990. High-rate spectroscopic active galactic nucleus monitoring at the Wise Observatory. I - Markarian 279. The Astrophysical Journal 351:75-82.

[16] MAOZ , D. et al. 1994. How fast do quasar emission lines vary? First results from a program to monitor the Balmer lines of Palomar-Green quasars. The Astrophysical Journal 421:34-45.

[17] MARCONI , A. et al. 2004. Local supermassive black holes, relics of active galactic nuclei and the X-ray background. Mon. Not. R. Astron. Soc. 351:169-185.

[18] MAZA , J. et al. 1993. Calan-Tololo Survey. V. Two hundred new southern quasars. Rev. Mex. Astron. Astrofis. 25, Issue 1:51-57.

[19] MAZA , J. et al. 1995a. Calan-Tololo Survey. VI. One hundred new southern quasars. Rev. Mex. Astron. Astrofis. 31:119-129.

[20] MAZA , J. et al. 1995b. Calan-Tololo Survey. VII. One hundred new southern quasars. Rev. Mex. Astron. Astrofis. 31:159-169.

[21] MAZA , J. et al. 1996. Calan-Tololo Survey. VIII. One hundred new southern quasars. Rev. Mex. Astron. Astrofis. 32:35-45.

[22] NETZER, H. 2003. The largest black holes and the most luminous galaxies. The Astrophysical Journal 583:L5-L8.

[23] NETZER, H. et al. 2007. Black Hole Mass and Growth Rate at High Redshift. The Astrophysical Journal 671, Issue 2:1256-1263.

[24] ONKEN, C. A., PETERSON, B. M., 2002. The Mass of the Central Black Hole in the Seyfert Galaxy NGC 3783. The Astrophysical Journal, Volume 572, Issue 2:746-752.

[25] ONKEN, C. A. et al., 2004. Supermassive Black Holes in Active Galactic Nuclei. II. Calibration of the Black Hole Mass-Velocity Dispersion Relationship for Active Galactic Nuclei. The Astrophysical Journal 615, Issue 2:645-651.

[26] OSTERBROCK, D. E., FERLAND, G. J., 2006. Active Galactic Nuclei - Diagnostics and Physics and Active Galactic Nuclei - Results. In: Astrophysics of Gaseous Nebulae and Active Galactic Nuclei. 2ª ed. Sacramento, CA, USA, University Science Books. pp. 325-393.

[27] PETERSON, B. M. 2006. The Broad-Line Region in Active Galactic Nuclei. Lect. Notes Phys. 693:77-100.

[28] PETERSON, B. M. et al. 2005. Multiwavelength Monitoring of the Dwarf Seyfert 1 Galaxy NGC 4395. I. A Reverberation-based Measurement of the Black Hole Mass. The Astrophysical Journal 632, Issue 2:799-808.

[29] PETERSON, B. M. et al. 2004. Central masses and Broad-Line Region sizes of Active Galactic Nuclei. II. A homogeneous analysis of a large Reverberation-Mapping database. The Astrophysical Journal 613:682-699.

[30] PETERSON, B. M. 2001. Variability of Active Galactic Nuclei. En: Advanced Lectures on the Starburst-AGN Connection: 26-30 June, 2000. Tonantzintla, Puebla, Mexico, 26-30 June, 2000. Singapore: World Scientific, 2001, pp. 3-64

[31] PETERSON, B. M. 2000. The Broad-Line Region. In: An introduction to Active Galactic Nuclei. 1ª ed. Cambridge, UK, Cambridge University Press. pp. 67-92.

[32] RODRIGUEZ-PASCUAL, P. M. et al. 1997. Steps towards determination of the size and structure of the Broad-Line Region in Active Galactic Nuclei. IX. Ultraviolet observations of Fairall 9. The Astrophysical Journal Supplement Series 110:9-20.

[33] STETSON, P. 1987. DAOPHOT: A computer program for crowded-field stellar photometry. Astronomical Society of the Pacific 99:191-222.

[34] VANDEN BERK, D. E. et al. 2004. The ensemble photometric variability of ~ 25.000 quasars in the SLOAN Digital Sky Survey. The Astrophysical Journal 601:692-714.

[35] VESTERGAARD, M. 2004. Early growth and efficient accretion of massive black holes at high redshift. The Astrophysical Journal 601:733-752.

[36] VESTERGAARD, M. 2002. Determining central black hole masses in distant active galaxies. The Astrophysical Journal 571:676-691.

[37] WOO, J. et al, 2010. Evolution of the $M_{\rm BH} - \sigma_\star$ and $M_{\rm BH} - L_{\rm bulge}$ Relations. In: Co-Evolution of Central Black Holes and Galaxies, Proceedings of the International Astronomical Union, IAU Symposium 267:183-188.

A

Continuum and BLR Emission Lines Light Curves

A.1 Light Curves: Spectrophotometrically Monitored Objects

The light curve for each of those object is divided in the continuum and the available emission lines in its spectra. The *Y* axis is a measure of the relative flux between the quasars and the geometrical weighted mean flux of field stars for the continuum (as discussed in §3.2.3.3) and the relative flux given by a normalized spectrum for each emission line (as discussed in §4.3).

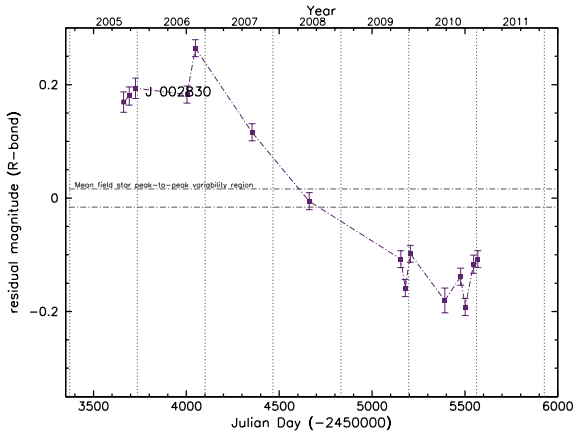

FIGURE A.1: Light curve of the continuum and BLR emission lines of J 002830. To date there is only one measurement for the C IV emission line, thus only its continuum light curve is shown. Y axis corresponds to the residual magnitude according to (3.16).

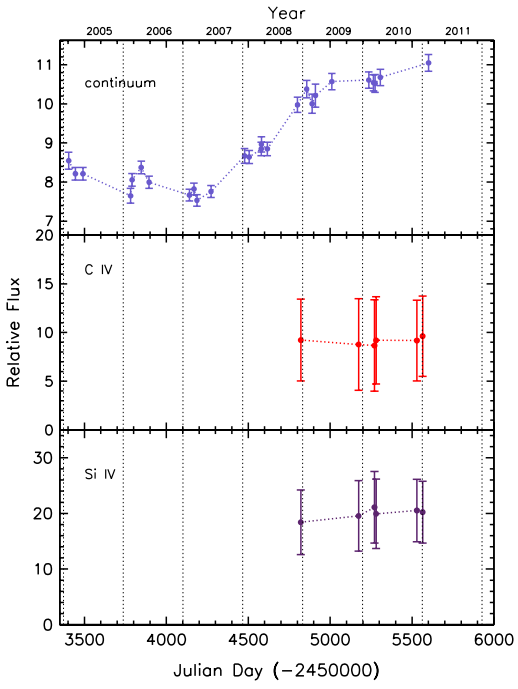

FIGURE A.2: Light curve of the continuum and BLR emission lines of CTQ 286

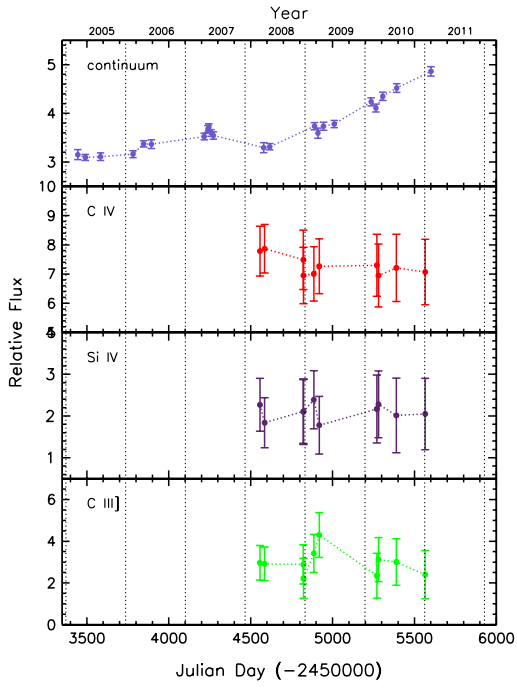

FIGURE A.3: Light curve of the continuum and BLR emission lines of CTQ 320

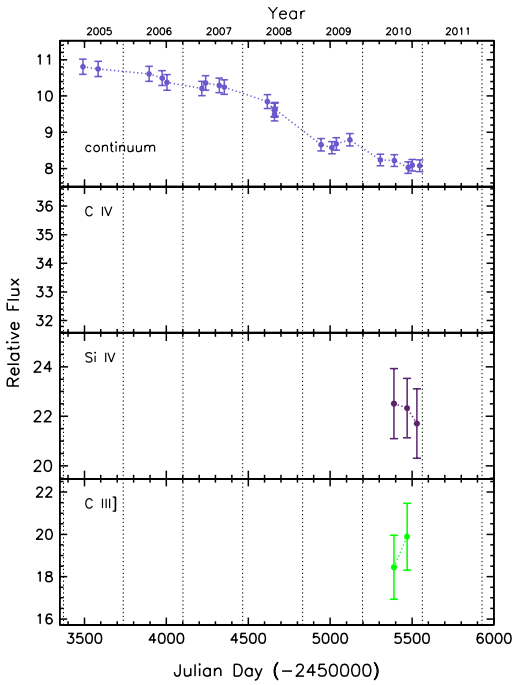

FIGURE A.4: Light curve of the continuum and BLR emission lines of CTQ 367

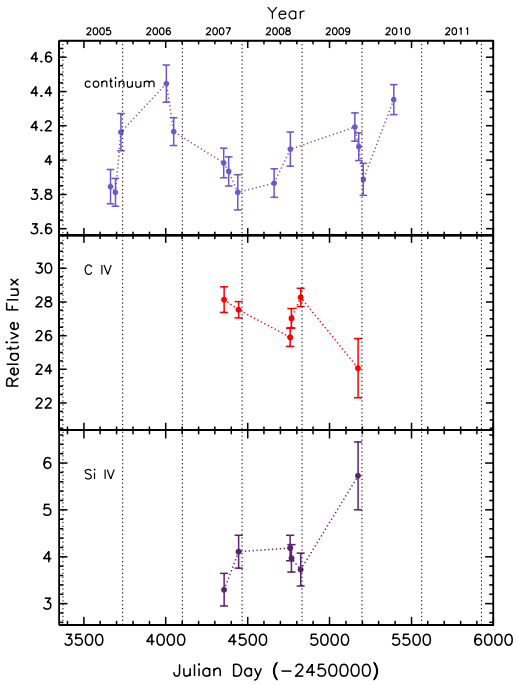

FIGURE A.5: Light curve of the continuum and BLR emission lines of CTQ 406

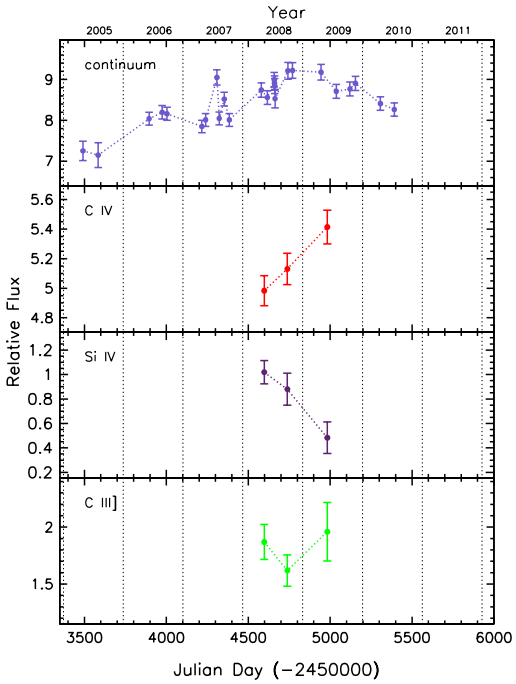

FIGURE A.6: Light curve of the continuum and BLR emission lines of CTQ 564

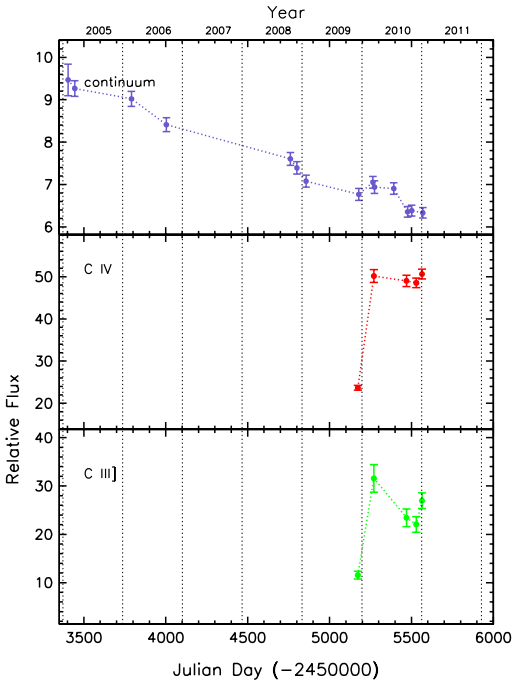

FIGURE A.7: Light curve of the continuum and BLR emission lines of CTQ 650

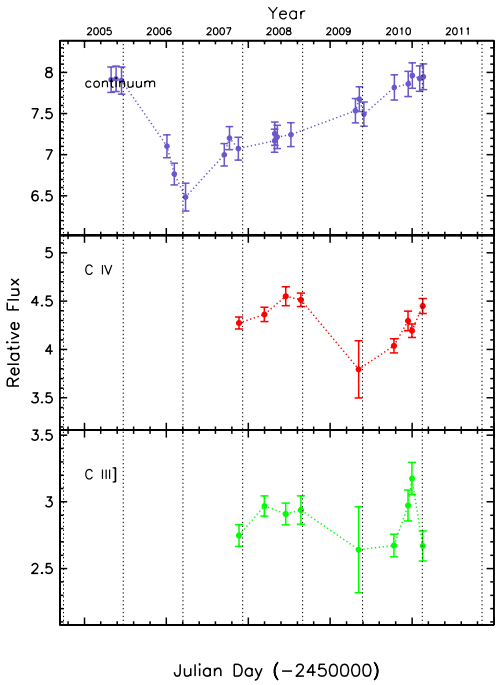

FIGURE A.8: Light curve of the continuum and BLR emission lines of CTQ 803

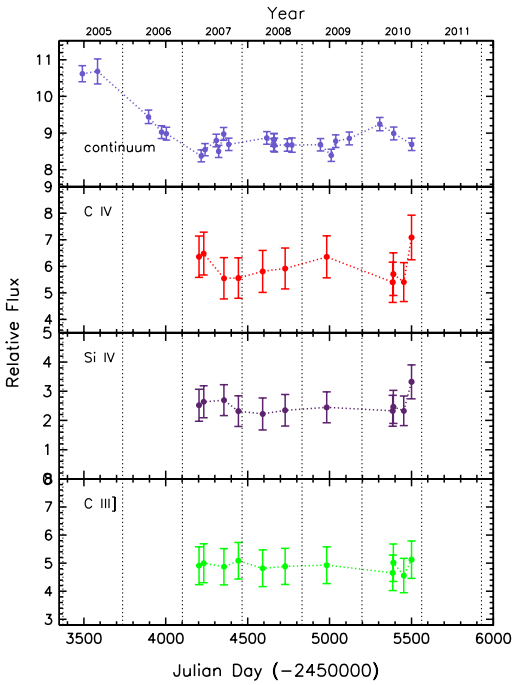

FIGURE A.9: Light curve of the continuum and BLR emission lines of CTQ 953

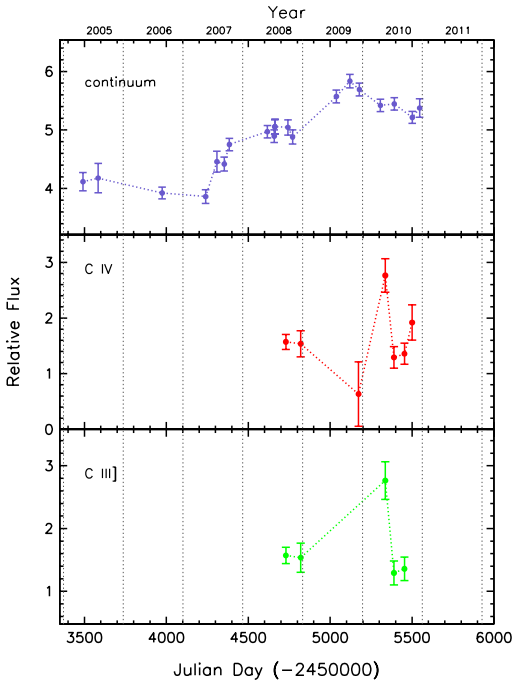

FIGURE A.10: Light curve of the continuum and BLR emission lines of CTQ 975

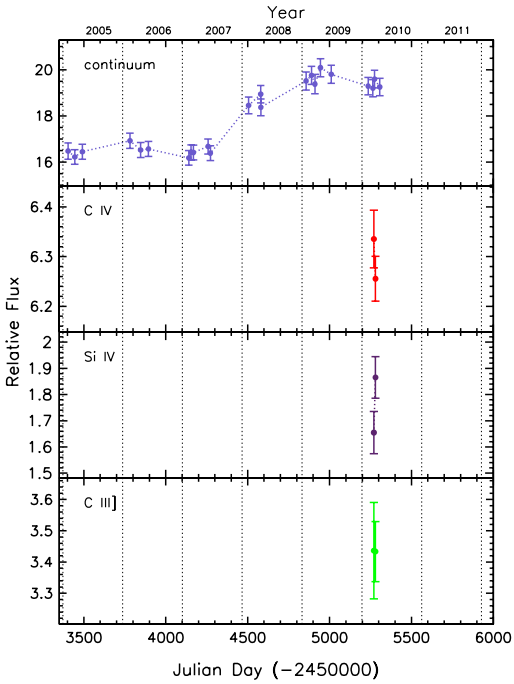

FIGURE A.11: Light curve of the continuum and BLR emission lines of CTQ 1061

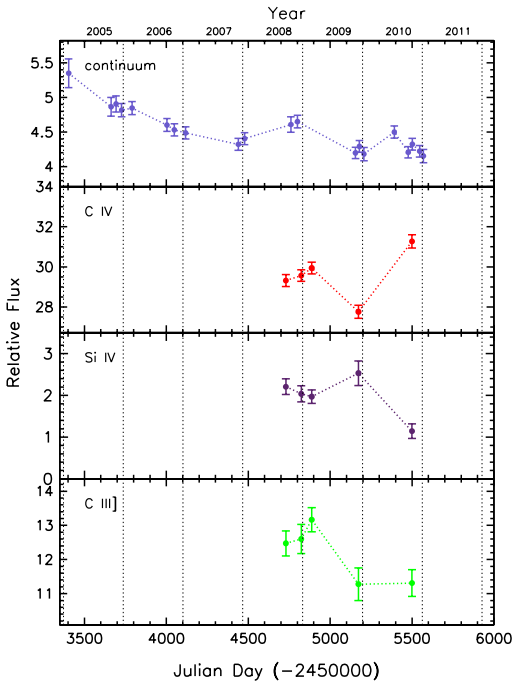

FIGURE A.12: Light curve of the continuum and BLR emission lines of HB89 [0325-385]

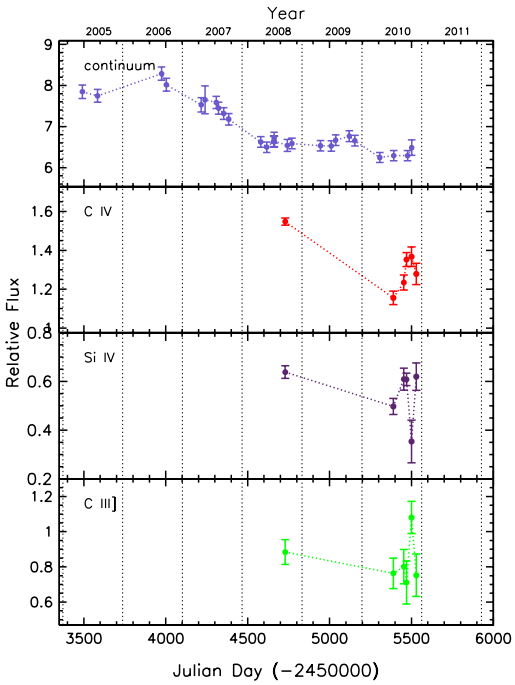

FIGURE A.13: Light curve of the continuum and BLR emission lines of J 214355

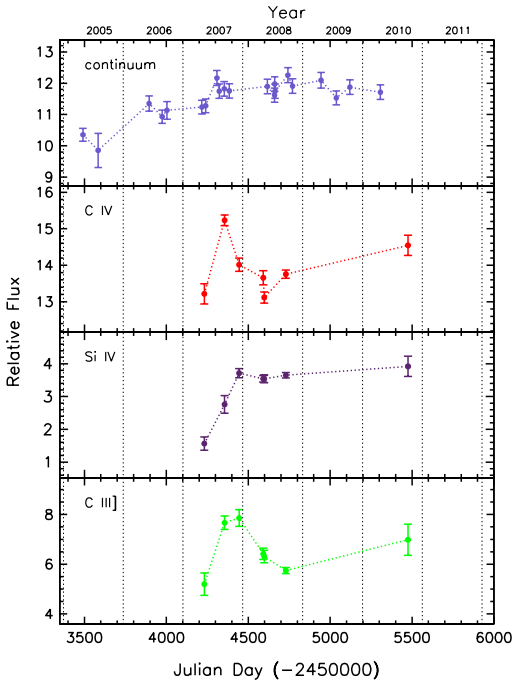

FIGURE A.14: Light curve of the continuum and BLR emission lines of J 221516

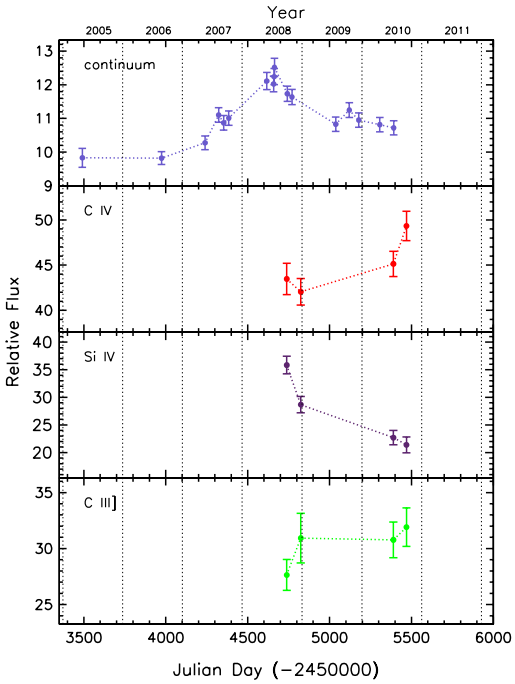

FIGURE A.15: Light curve of the continuum and BLR emission lines of J 224743

A.2 Continuum Light Curves: Photometrically Monitored Objects

Differential light curves in magnitude scale are shown for photometrically monitored objects with the Y axis in magnitude scale. A 3% variability amplitude region is plotted in dashed line. The mean field star magnitude is inside this region.

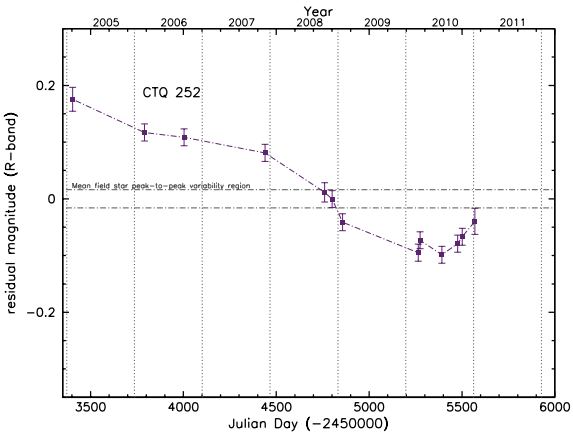

FIGURE A.16: Continuum differential light curve in the R band of CTQ 252

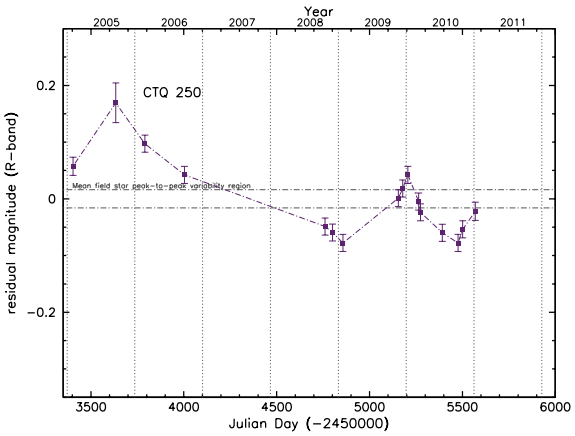

FIGURE A.17: Continuum differential light curve in the R band of CTQ 250

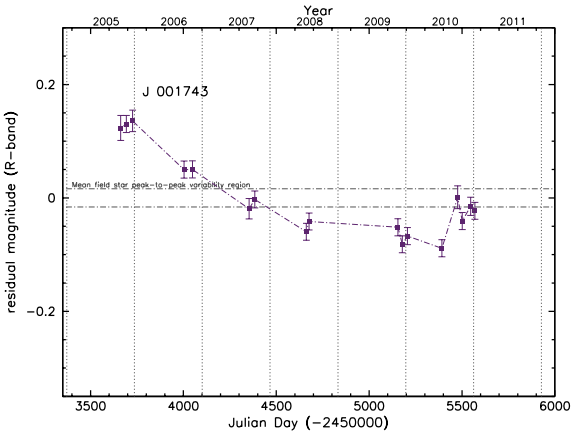

FIGURE A.18: Continuum differential light curve in the R band of J 001743

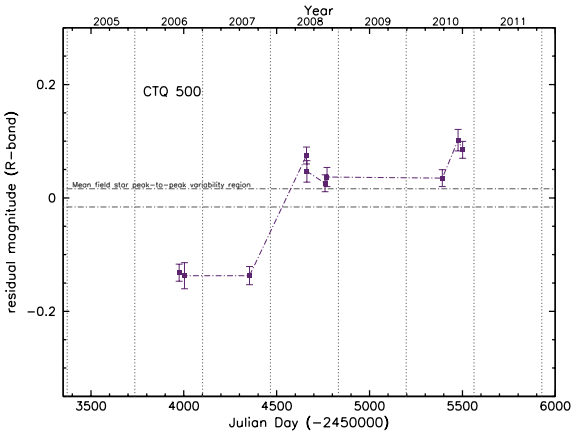

FIGURE A.19: Continuum differential light curve in the R band of CTQ 500

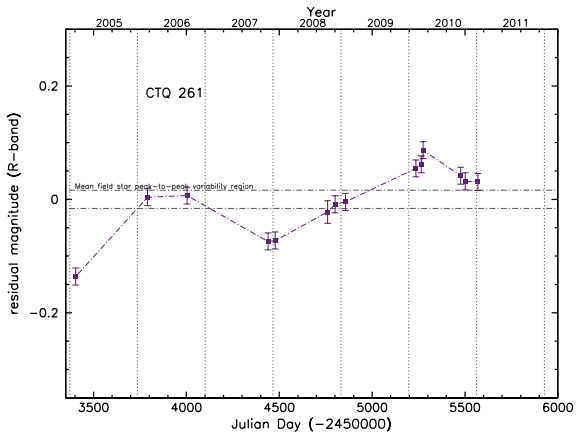

FIGURE A.20: Continuum differential light curve in the R band of CTQ 261

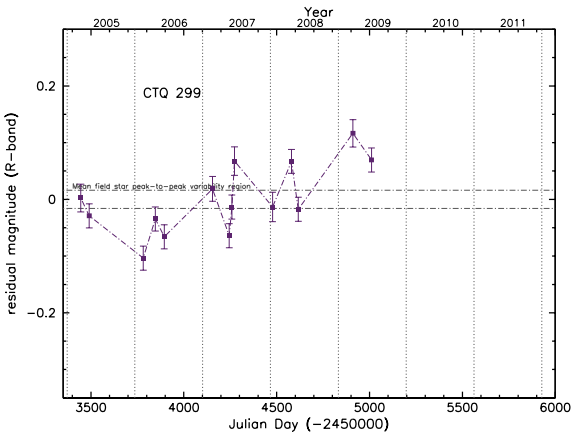

FIGURE A.21: Continuum differential light curve in the R band of CTQ 299

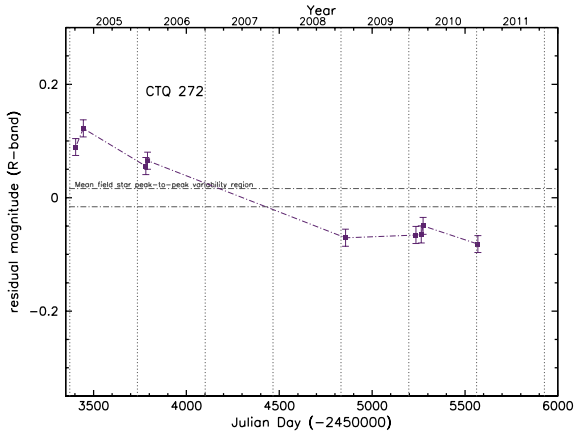

FIGURE A.22: Continuum differential light curve in the R band of CTQ 272

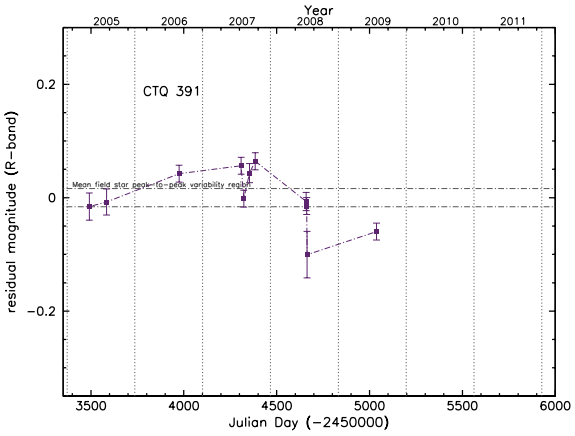

FIGURE A.23: Continuum differential light curve in the R band of CTQ 391

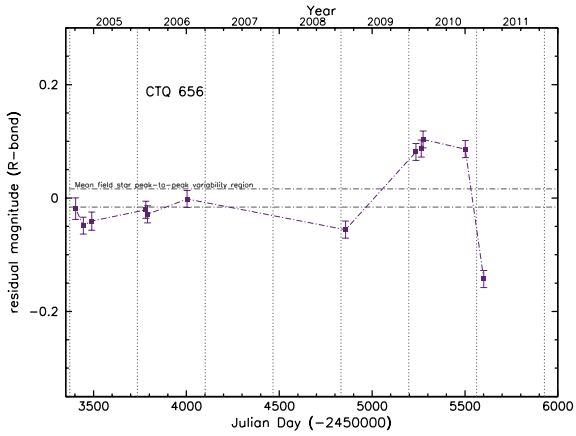

FIGURE A.24: Continuum differential light curve in the R band of CTQ 656

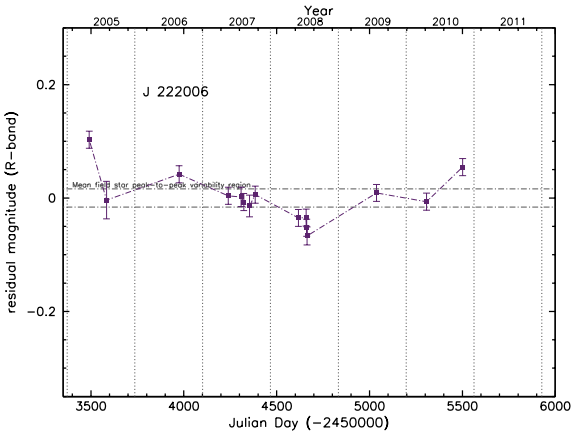

FIGURE A.25: Continuum differential light curve in the R band of J 222006

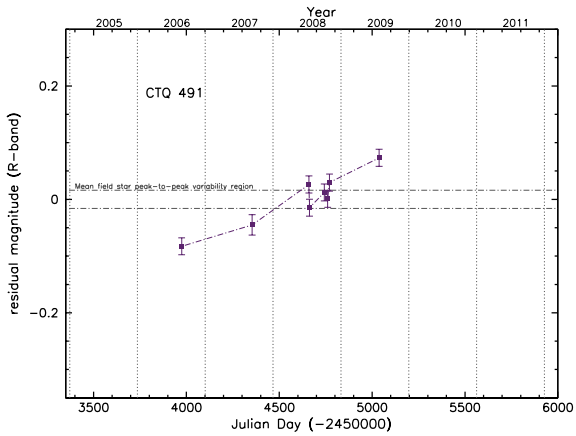

FIGURE A.26: Continuum differential light curve in the R band of CTQ 491

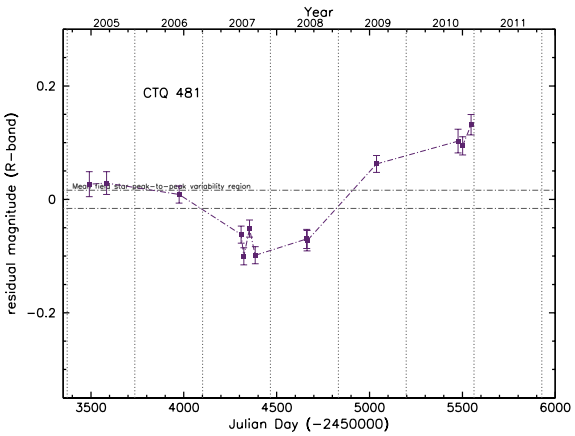

FIGURE A.27: Continuum differential light curve in the R band of CTQ 481

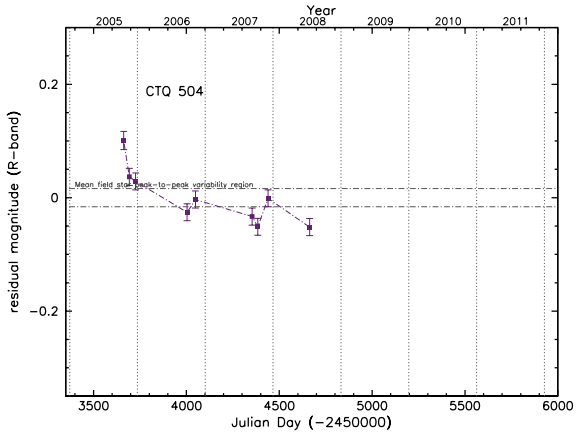

FIGURE A.28: Continuum differential light curve in the R band of CTQ 504

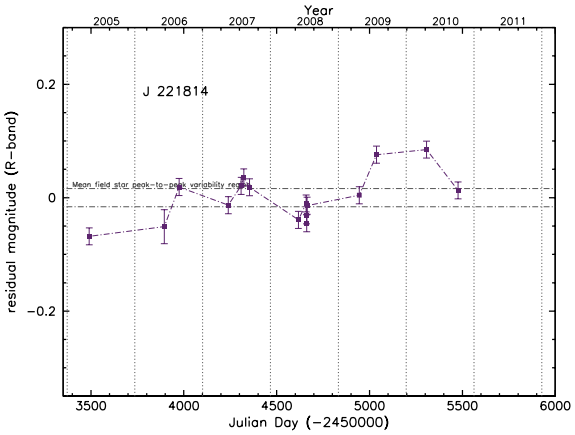

FIGURE A.29: Continuum differential light curve in the R band of J 221814

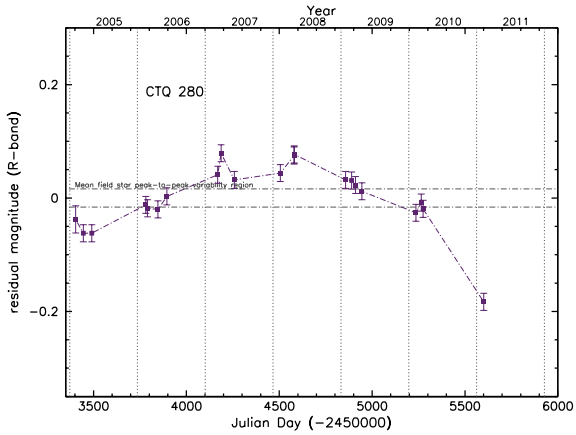

FIGURE A.30: Continuum differential light curve in the R band of CTQ 280

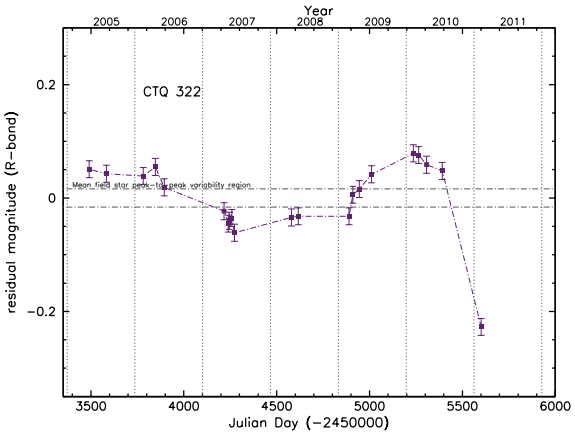

FIGURE A.31: Continuum differential light curve in the R band of CTQ 322

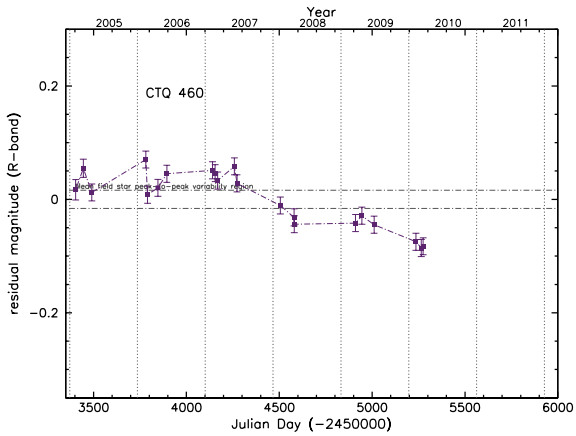

FIGURE A.32: Continuum differential light curve in the R band of CTQ 460

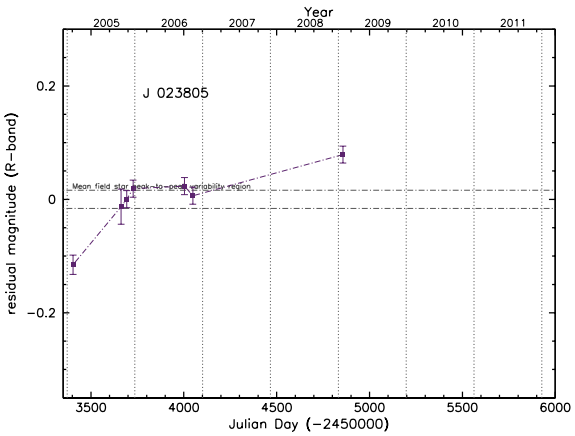

FIGURE A.33: Continuum differential light curve in the R band of J 023805

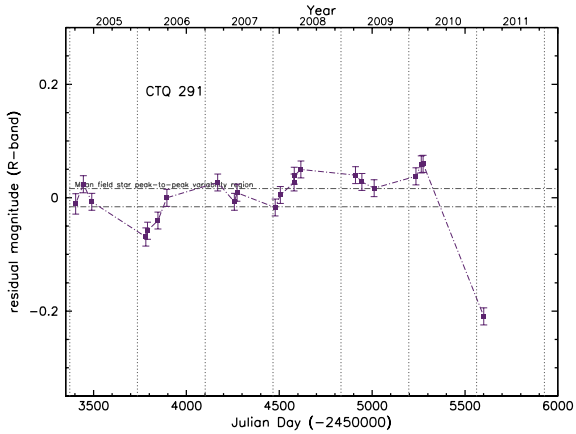

FIGURE A.34: Continuum differential light curve in the R band of CTQ 291

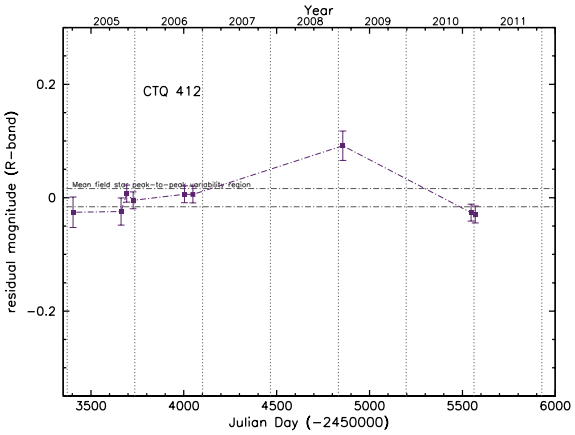

FIGURE A.35: Continuum differential light curve in the R band of CTQ 412

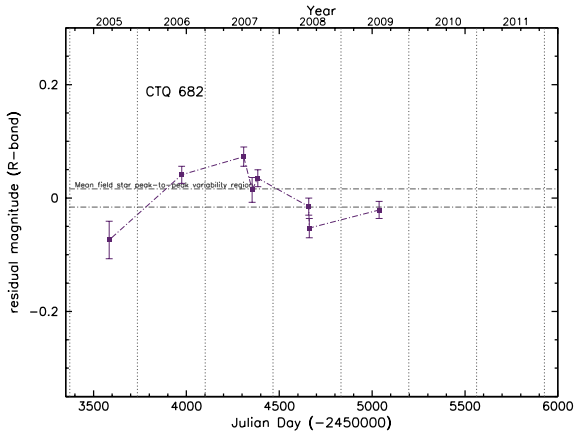

FIGURE A.36: Continuum differential light curve in the R band of CTQ 682

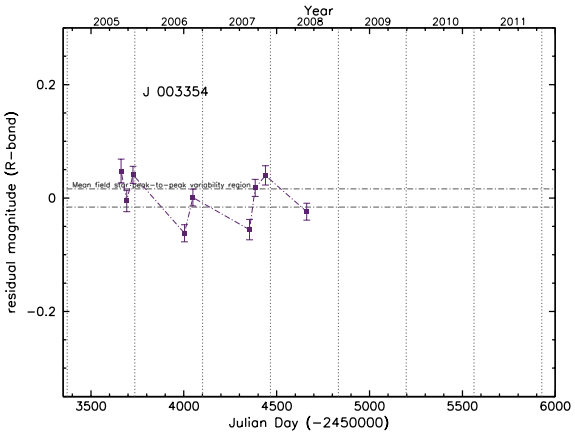

FIGURE A.37: Continuum differential light curve in the R band of J 003354

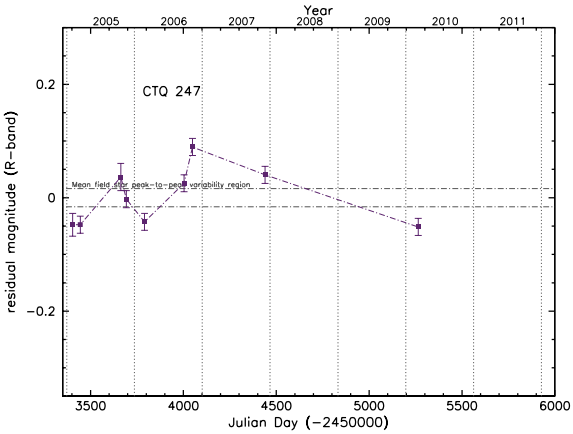

FIGURE A.38: Continuum differential light curve in the R band of CTQ 247

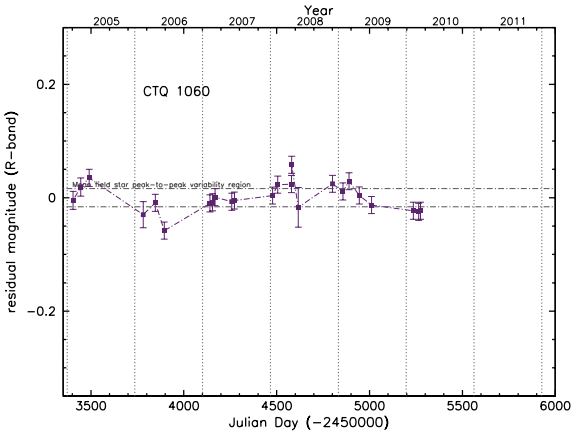

FIGURE A.39: Continuum differential light curve in the R band of CTQ 1060

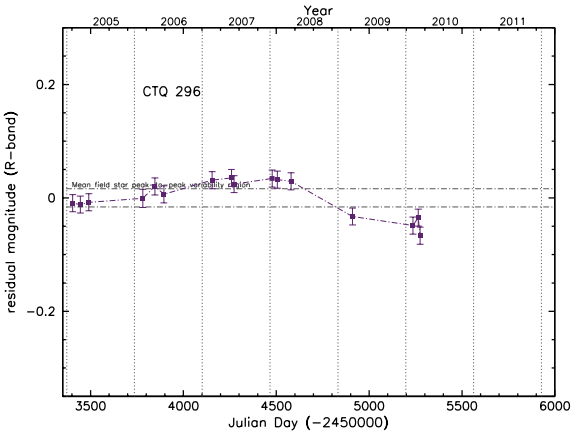

FIGURE A.40: Continuum differential light curve in the R band of CTQ 296

A.3 Continuum Light Curves: Photometrically Discarded Objects

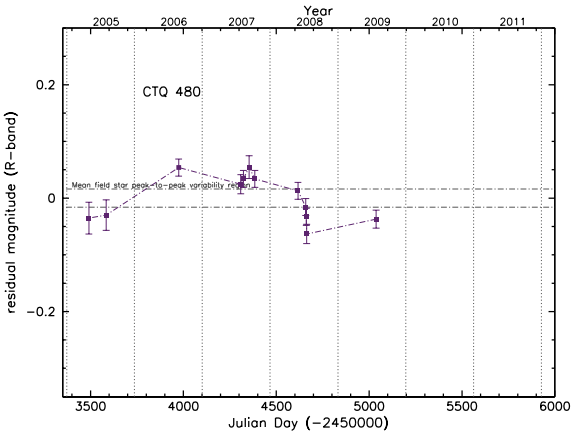

FIGURE A.41: Continuum differential light curve in the R band of CTQ 480

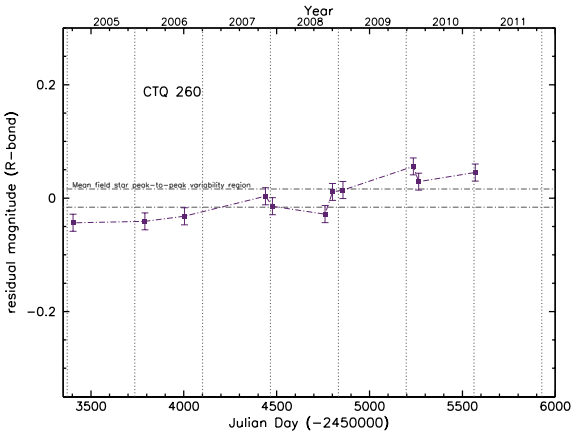

FIGURE A.42: Continuum differential light curve in the R band of CTQ 260

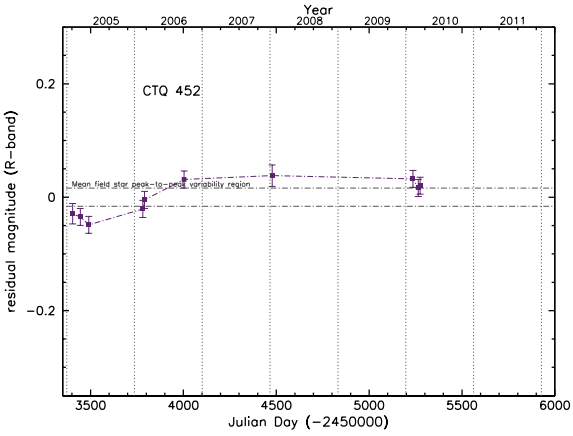

FIGURE A.43: Continuum differential light curve in the R band of CTQ 452

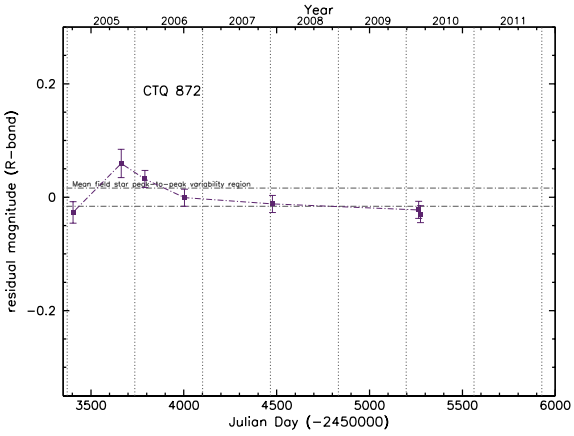

FIGURE A.44: Continuum differential light curve in the R band of CTQ 872

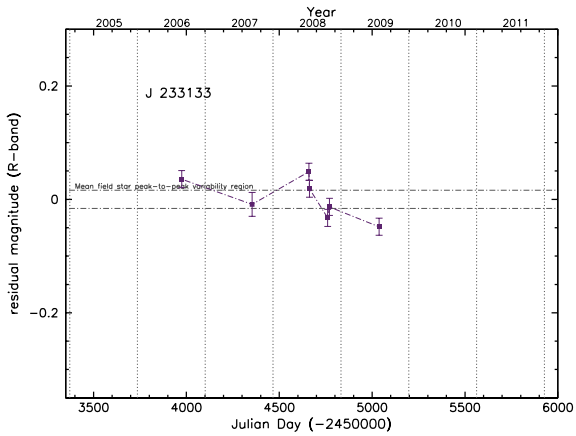

FIGURE A.45: Continuum differential light curve in the R band of J 233133

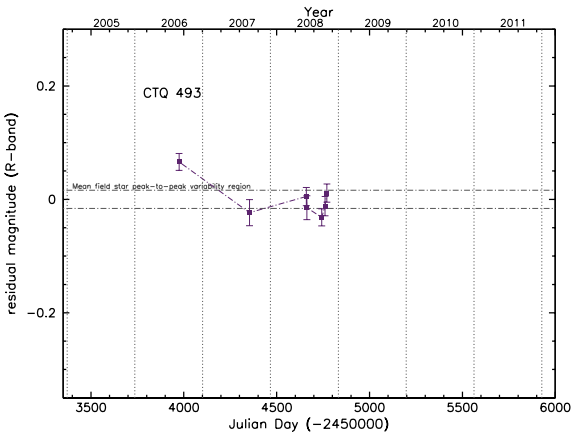

FIGURE A.46: Continuum differential light curve in the R band of CTQ 493

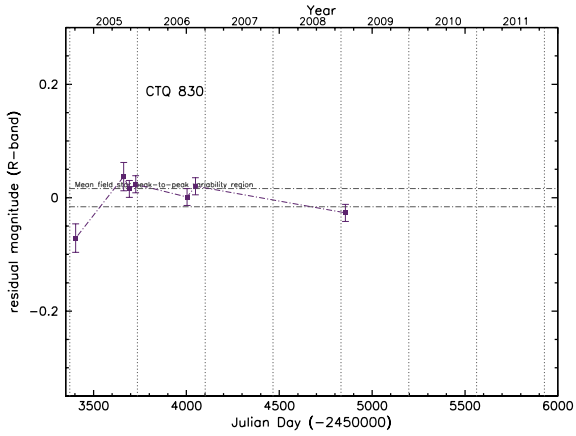

FIGURE A.47: Continuum differential light curve in the R band of CTQ 830

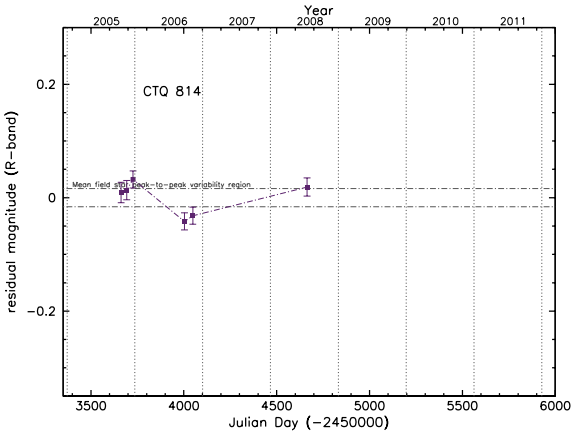

FIGURE A.48: Continuum differential light curve in the R band of CTQ 814

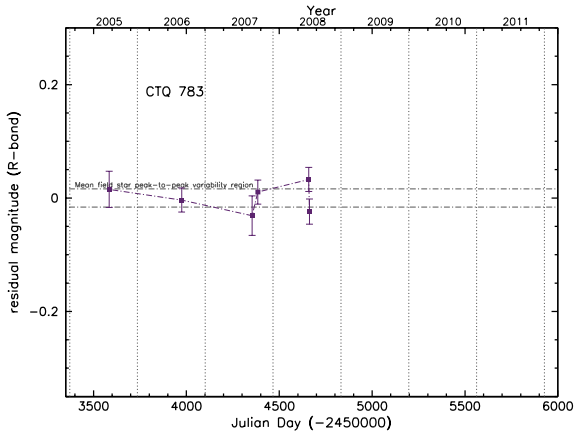

FIGURE A.49: Continuum differential light curve in the R band of CTQ 783

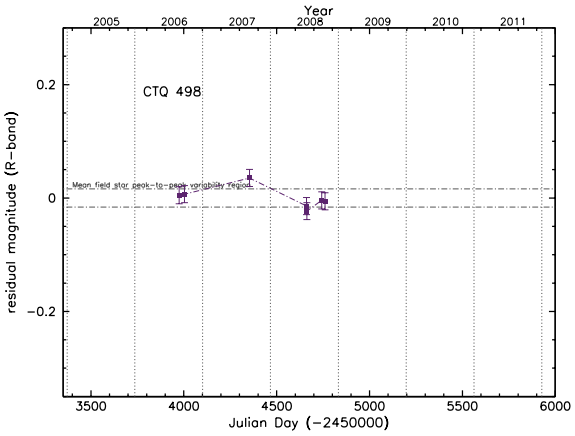

FIGURE A.50: Continuum differential light curve in the R band of CTQ 498

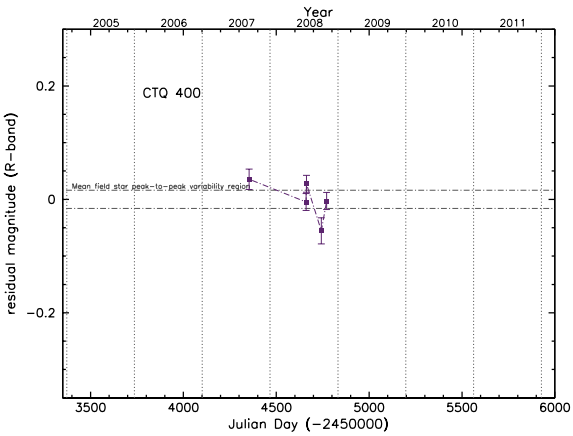

FIGURE A.51: Continuum differential light curve in the R band of CTQ 400

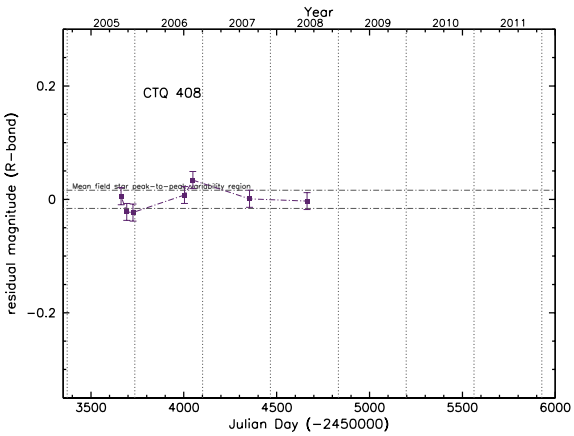

FIGURE A.52: Continuum differential light curve in the R band of CTQ 408

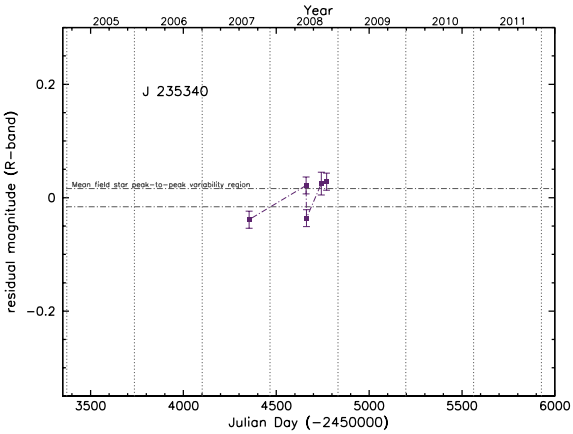

FIGURE A.53: Continuum differential light curve in the R band of J 235340

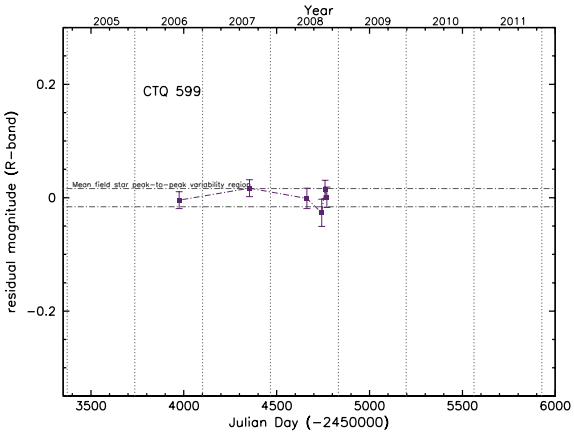

FIGURE A.54: Continuum differential light curve in the R band of CTQ 599

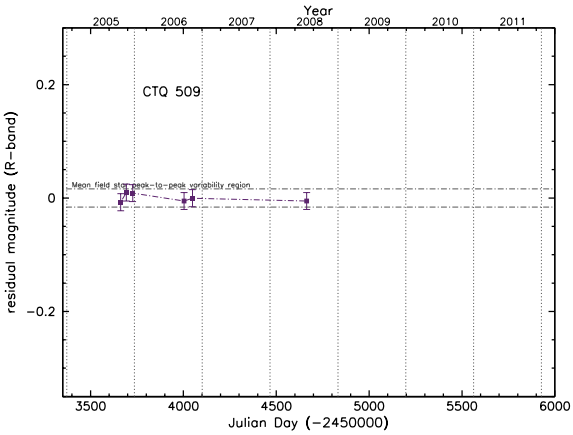

FIGURE A.55: Continuum differential light curve in the R band of CTQ 509

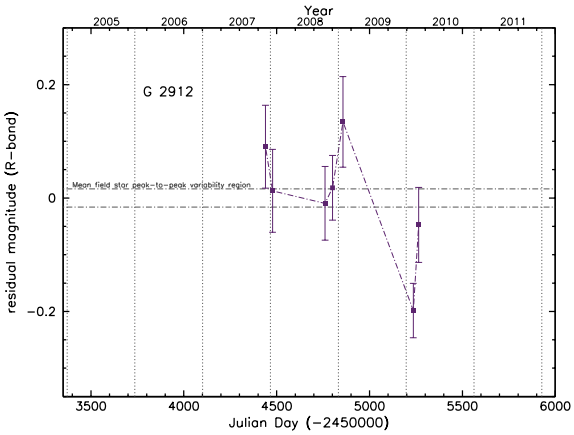

FIGURE A.56: Continuum differential light curve in the R band of G 2912

B

Optical Spectra

Calibrated spectra of the quasar and its comparison star are shown for the spectrophotometric sample. The only exception is CTQ 564 for which there are not calibrated spectra to date, thus the flux is given in counts. Normalized spectra are also shown for each object.

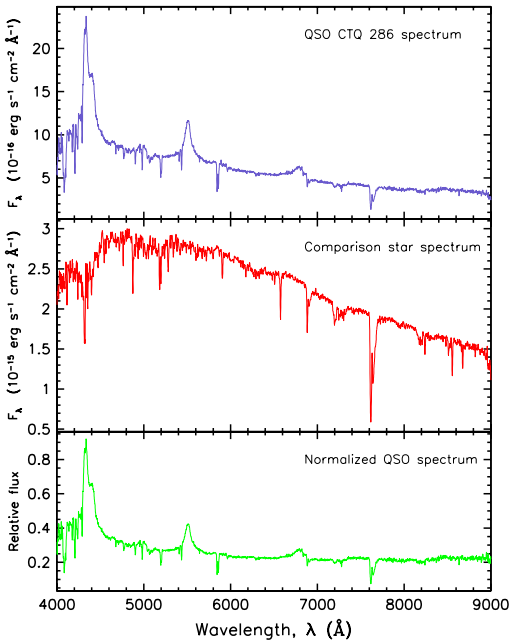

FIGURE B.1: Spectrum of CTQ 286 (top), its comparison star (middle) and the normalized QSO spectrum (bottom).

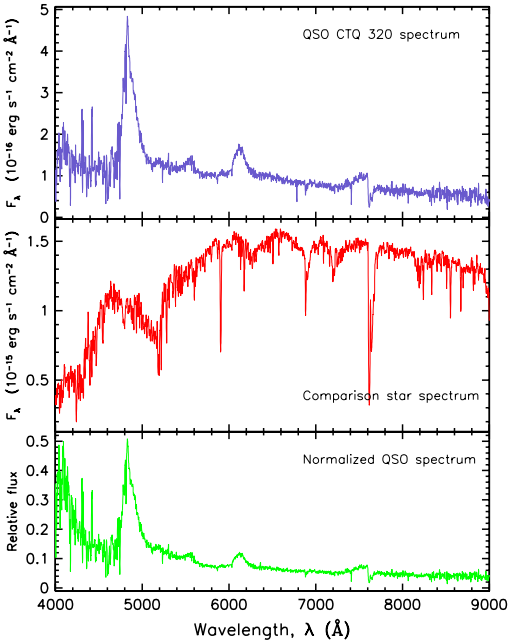

FIGURE B.2: Spectrum of CTQ 320 (top), its comparison star (middle) and the normalized QSO spectrum (bottom).

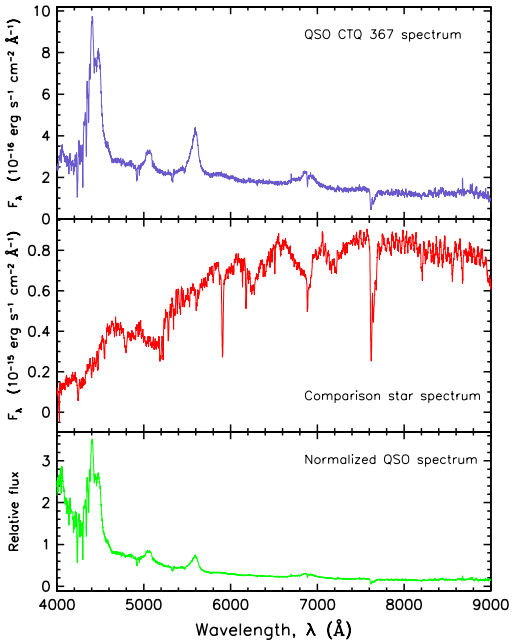

FIGURE B.3: Spectrum of CTQ 367 (top), its comparison star (middle) and the normalized QSO spectrum (bottom).

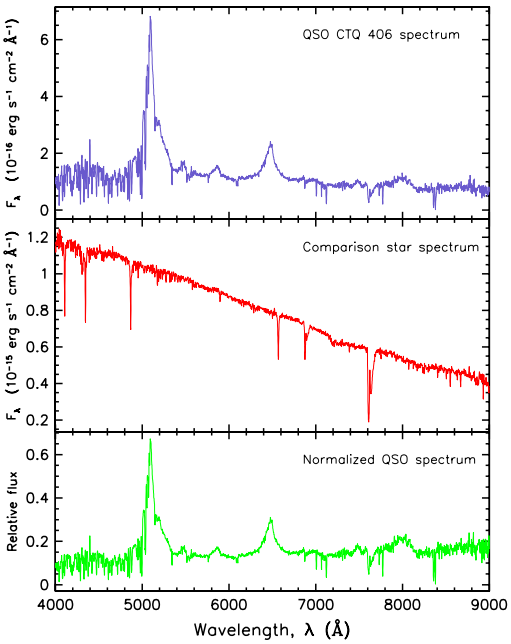

FIGURE B.4: Spectrum of CTQ 406 (top), its comparison star (middle) and the normalized QSO spectrum (bottom).

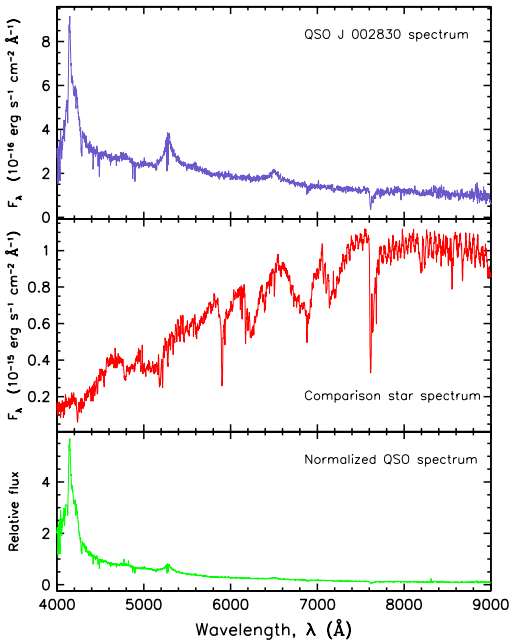

FIGURE B.5: Spectrum of CTQ 564 (top), its comparison star (middle) and the normalized QSO spectrum (bottom).

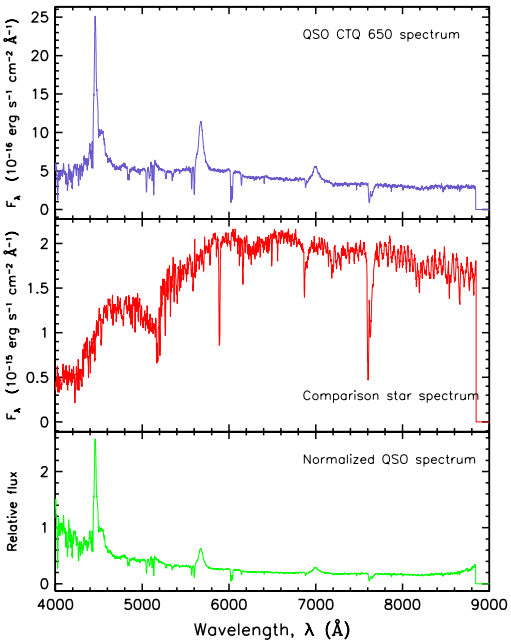

FIGURE B.6: Spectrum of CTQ 650 (top), its comparison star (middle) and the normalized QSO spectrum (bottom).

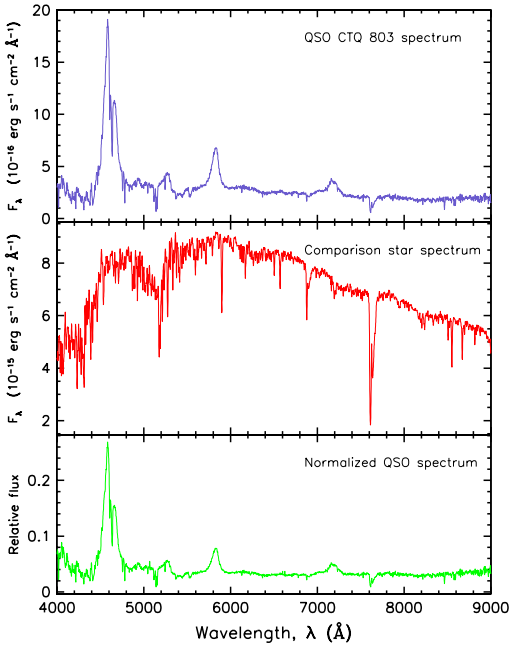

FIGURE B.7: Spectrum of CTQ 803 (top), its comparison star (middle) and the normalized QSO spectrum (bottom).

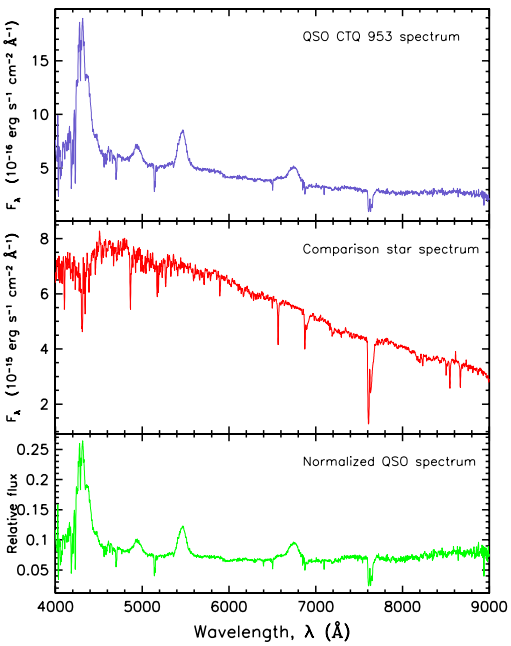

FIGURE B.8: Spectrum of CTQ 953 (top), its comparison star (middle) and the normalized QSO spectrum (bottom).

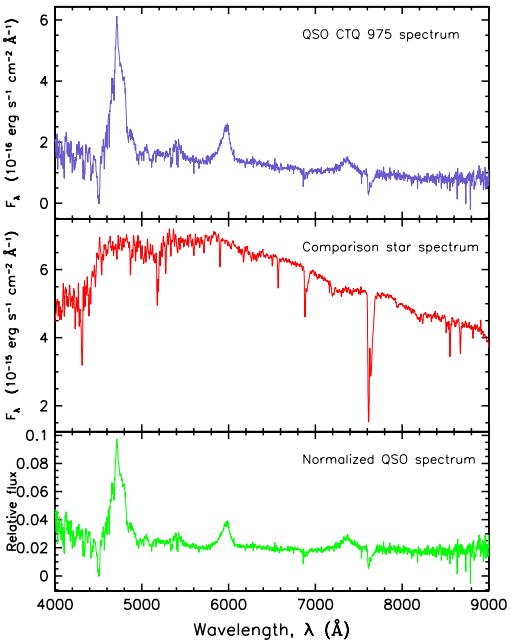

FIGURE B.9: Spectrum of CTQ 975 (top), its comparison star (middle) and the normalized QSO spectrum (bottom).

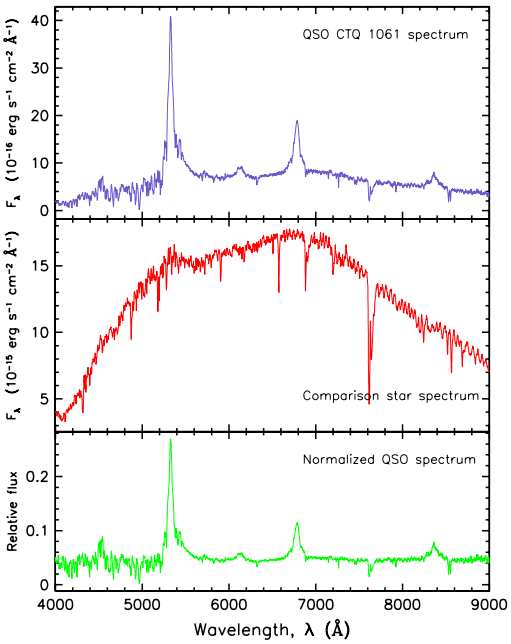

FIGURE B.10: Spectrum of CTQ 1061 (top), its comparison star (middle) and the normalized QSO spectrum (bottom).

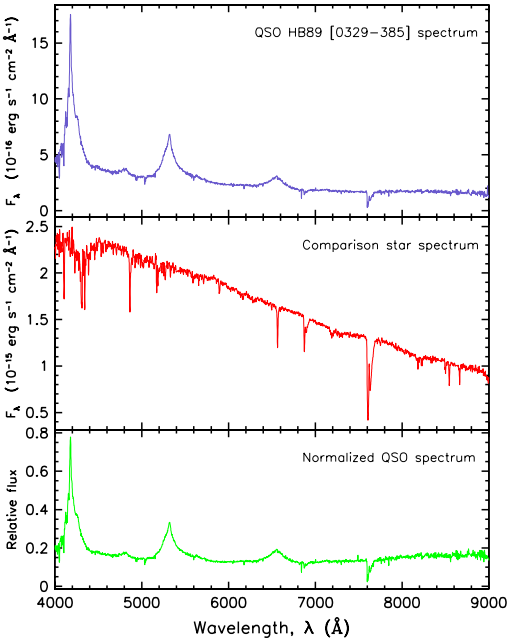

FIGURE B.11: Spectrum of HB89 [0325-385] (top), its comparison star (middle) and the normalized QSO spectrum (bottom).

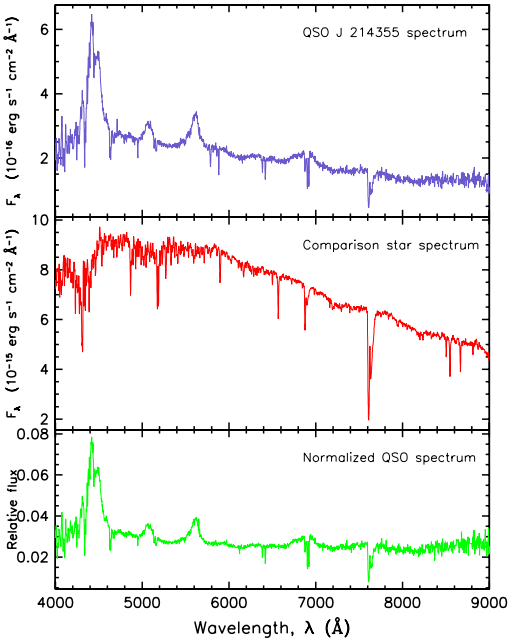

FIGURE B.12: Spectrum of J 214355 (top), its comparison star (middle) and the normalized QSO spectrum (bottom).

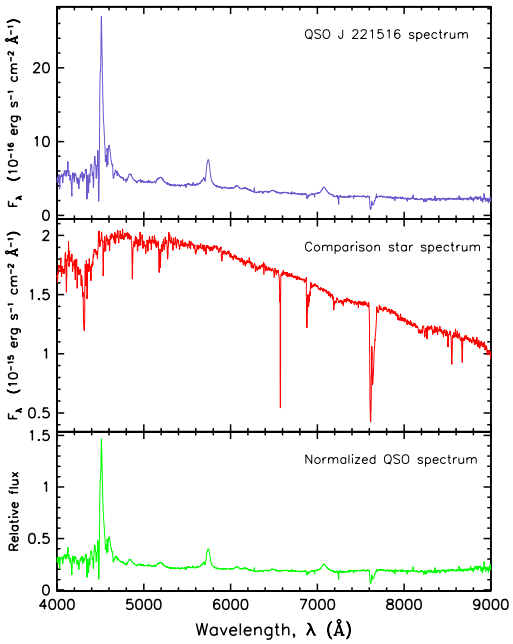

FIGURE B.13: Spectrum of J 221516 (top), its comparison star (middle) and the normalized QSO spectrum (bottom).

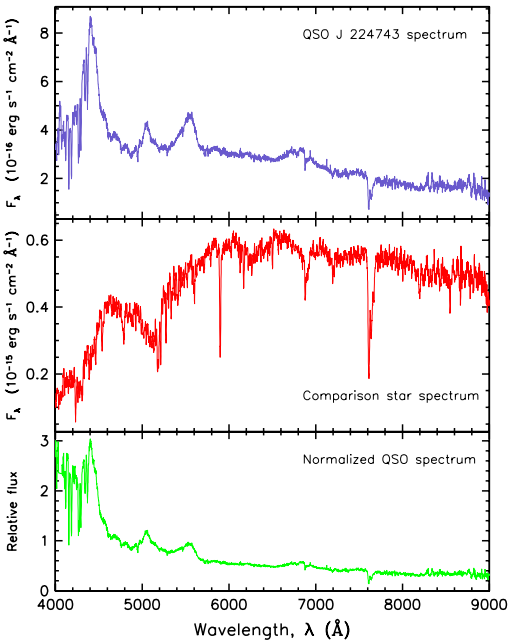

FIGURE B.14: Spectrum of J 224743 (top), its comparison star (middle) and the normalized QSO spectrum (bottom).

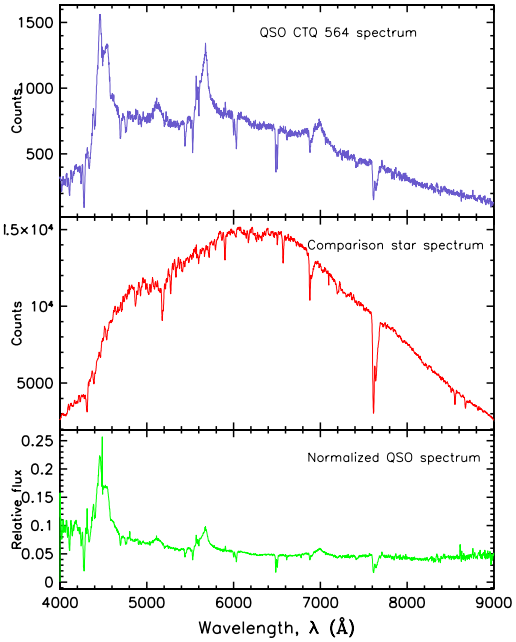

FIGURE B.15: Spectrum of CTQ 564 (top), its comparison star (middle) and the normalized QSO spectrum (bottom).